

CMS Draft Analysis Note

The content of this note is intended for CMS internal use and distribution only

2020/05/26

Archive Hash: 658f350-D

Archive Date: 2020/05/23

B^+ production in PbPb collisions at $\sqrt{s_{\text{NN}}} = 5.02 \text{ TeV}$

Gwang-Jun Kim¹, Zhaozhong Shi¹, Júlia Silva², Jing Wang¹, Ran Bi¹, Michael Peters¹, Camelia Mironov¹, Nuno Leonardo², and Yen-Jie Lee¹

¹ Massachusetts Inst. of Technology

² Técnico Lisboa

Abstract

In this note we present the measurements of B^+ meson p_T differential yields with respect to p_T and centrality with 2018 PbPb collision data at $\sqrt{s_{\text{NN}}} = 5.02 \text{ TeV}$. The exclusive decay channel $B^+ \rightarrow J/\psi K^+$ is used for the reconstruction of the events. This note is a compliment of the analysis note [1] on measurement of B_s^0 meson production and its corrected yield.

This box is only visible in draft mode. Please make sure the values below make sense.

PDFAuthor:

Gwang-Jun Kim

PDFTitle:

B^+ production in PbPb collisions at $\sqrt{s_{\text{NN}}} = 5.02 \text{ TeV}$

PDFSubject:

CMS

PDFKeywords:

CMS, physics, B meson, PbPb collisions, quark gluon plasma, open heavy flavor, cold nuclear matter effect

Please also verify that the abstract does not use any user defined symbols

1 Version Notice

- 2 Answer to the re-approval comments HIN conveners: https://espace.cern.ch/cms-heavyion/hf/hin19011/_layouts/15/WopiFrame.aspx?sourcedoc=/cms-heavyion/hf/hin19011/Shared%20Documents/Answer%20to%20Re-approval%20Comments/Answer%20to%20HIN-19-011%20Re-approval%20Comments.docx&action=default
- 6 Since the re-approval presentation date on 04/24/2020 for the CADI HIN-19-011, we have
7 addressed all the comments from the HIN conveners and updated our studies in this B_s^0 AN-
8 19-055 and the complimentary B^+ AN-19-132. The major changes in the sections of this AN are
9 summarized as below:

10 No major changed except minor text update is made in the following sections:

11 **Introduction**

12 **Datasets and Event Selections**

13 **B^+ meson reconstruction**

14 **B^+ meson selection optimization**

15 **B^+ candidate properties comparison between data and MC**

16 **Results**

17 **Acceptance and Efficiency**

18 **Appendix A Training Results**

19 **Appendix B Non-prompt J/Ψ background**

20 **Appendix C PDF Variations**

21 We have made the changes in the following sections:

22 **Signal Extraction**

- 23 1. Table 2 the comparison between symmetric and asymmetric uncertainties in the raw yield
24 extraction has been added.
- 25
- 26 2. A dedicated 7.3 section for the use of sPlot weight and comparison of the sPLOT weighted
27 with the nominal unweighted efficiency correction factors have been added.

28 **Closure Test of the Corrected Yield**

- 29 1. small samples → data-like samples
- 30 2. Figure 38 for the asymmetric statistical uncertainties on the efficiency correction factor
31 $\langle \frac{1}{\alpha \times \epsilon} \rangle$ has been added.

32 3. Table 9 the comparison between the statistics uncertainties of raw yield, efficiency correc-
33 tion factor, and corrected yield has been added.

34 **Systematics uncertainties**

35 1. More detailed descriptions with each step (muon identification, muon trigger, and the
36 tracking) on the TnP analysis (line 431 - 441) and the plots (Figure 43 - 48) of their contribu-
37 tions to the systematics individually have been added.

DRAFT

38 Contents

39	1	Introduction	2
40	2	Datasets and Event Selections	3
41	2.1	Datasets	3
42	2.2	MC samples	3
43	2.2.1	MC reweighting	3
44	3	B^+ meson reconstruction	6
45	3.1	Muon and J/ψ selection	6
46	3.2	Track selection	6
47	4	B^+ meson selection	7
48	4.1	Cut optimization	7
49	4.2	Fiducial region	16
50	5	MC-Data Comparison	18
51	5.1	B candidate properties comparison between data and MC	18
52	6	Signal Extraction	21
53	6.1	Closure test of the fitting procedure	24
54	7	Acceptance and Efficiency	26
55	7.1	Muon Efficiency Correction: Tag-and-Probe	26
56	7.2	Acceptance and Efficiency from PbPb MC	33
57	7.3	sPlot Weight Techniques Studies	35
58	8	Closure Test of the B^+ Corrected Yield	39
59	9	Results	49
60	9.1	p_T differential corrected yield in PbPb collisions at 5.02 TeV	49
61	10	Systematic uncertainties	51
62	10.1	Summary table	51
63	10.2	T_{AA} and N_{MB}	54
64	10.3	Branching ratio	54
65	10.4	Tracking efficiency	54
66	10.5	Muon efficiency: Tag and Probe	54
67	10.6	Selection efficiency: Splot weight	57
68	10.7	p_T shape: Bpt weight	59
69	10.8	MC stats: Toy MC study	59
70	10.9	Signal extraction: PDF variation	62
71	A	Training Results	65
72	B	Non-prompt J/ψ background	73
73	C	PDF variation studies	75

74 1 Introduction

75 The study of heavy-quark production plays a crucial role in understanding the mechanisms of
 76 heavy-quark interaction with the medium created in heavy-ion collisions. Because of the large
 77 masses, Heavy quarks are primarily produced at early stages of heavy-ion collisions, and there-
 78 fore they carry information about the pre-thermalization properties of the quark gluon plasma.
 79 Compared with light quarks and gluons, heavy quarks are expected to lose less energy due
 80 to smaller color charge and the dead cone effect [2]. As a consequence of this phenomenon,
 81 several theoretical calculations predict sizable differences in the suppression pattern of light
 82 particle versus that of charmed and beauty mesons, in central PbPb collisions. Using the high
 83 luminosity LHC runs of pp and PbPb collisions at 5 TeV, the CMS collaboration was able to
 84 measure already the nuclear modification factor, R_{AA} , of charmed particles [3] [4] in different
 85 centrality ranges. In addition, beauty meson has been measured for B^+ [5] and B_s^0 [6] in the
 86 inclusive centrality range. These measurements show a similar suppression in a very wide
 87 transverse momentum interval ($2 < p_T < 100 \text{ GeV}/c$ for charm, $7 < p_T < 50 \text{ GeV}/c$ for beauty).
 88 The goal of the present analysis is to test the flavour dependence of energy loss and to study
 89 the hadronization of beauty quark, by measuring the exclusive production of B^+ mesons in
 90 PbPb collisions in a similar kinematic range ($7 < p_T < 50 \text{ GeV}/c$), which is the same as the B_s
 91 analysis [1], with the increased statistics by 2018 LHC Run.

92

93 In this note, the analysis of the B^+ meson transverse momentum spectra in PbPb collisions at
 94 5.02 TeV is presented. PbPb spectra is fully analyzed with the new 2018 PbPb collision data.
 95 The B mesons are measured in rapidity region $|y_{\text{lab}}| < 2.4$, via the full reconstruction of the
 96 decay channel: $B^+ \rightarrow J/\psi K^+$ with branching fraction $\mathcal{B} = (6.02 \pm 0.17) \times 10^{-5}$. At low p_T
 97 5-10GeV/c, most candidates are confined to forward rapidity region largely due to limited de-
 98 tector muon acceptance. In this p_T range we adopt fiducial region which is $1.5 < |y_{\text{lab}}| < 2.4$.
 99 As this analysis does not separate B^+ from B^- , the meson are referred to generically as B^+ , for
 100 the purposes of reconstruction. For the corrected yields, the combined results are divided by
 101 two to obtain an average.

102

103 This note is a compliment of the analysis note CMS AN-19-055([1]) on measurement of B_s^0
 104 meson production and its corrected yield. Several materials used for B^+ are the same with B_s^0 .
 105 From now on, whenever B_s^0 Analysis note is referred, please check the corresponding sections
 106 and items on the reference above for more detailed information.

107 2 Datasets and Event Selections

108 2.1 Datasets

109 This analysis is performed using the 2018 PbPb data at $\sqrt{s_{\text{NN}}}=5.02$ TeV. The Primary dataset,
 110 triggers, and event selections we use are the same with B_s analysis ongoing parallel. For more
 111 information, please check the corresponding sections on B_s analysis note (CMS AN-19-055) [1].

112 2.2 MC samples

113 This section is identical to the B_s AN. The only difference is that we use different decay channels
 114 for reconstruction of B mesons. Here we use $B^+ \rightarrow J/\psi K^+$ channel.

115 2.2.1 MC reweighting

116 We use dedicated method to calculate the acceptance and efficiency correction factor, by taking
 117 average over data which is described in the section. 7.2. The p_T weight we get here is not used
 118 for our nominal result, since the average over data already includes the information of data p_T
 119 shape. However, the p_T weight we obtain here is used to check the robustness of the method,
 120 and will be quoted as systematics uncertainties related with the method.

121 The p_T spectrum of the B^+ MC was reweighted in order to match with the data. We first
 122 evaluated the raw yield of the data and MC without any p_T weight in p_T range 5-60GeV, and
 123 normalized them. Then we took the ratio of the two to get the first p_T weight distribution. This
 124 distribution is fitted with polynomials, and we found that the 4th order polynomial have the
 125 minimum χ^2 among the lowest order polynomials, thus we used this as our weight function.
 126 After then, we examined the new raw yield of MC with the new weight, and compared the
 127 distributions to get a new weight functions. We iterated this twice, and we found that the first
 128 p_T weight obtained already shows good agreement with data. Thus we use that p_T weight as
 129 our weight function.

130 In Fig. 1, the normalized distributions of data and MC raw yield and their ratios are presented.
 131 The second row (with 1st p_T weight) already shows reasonable agreement between data and
 132 MC. The red fit function on the top right plot is our nominal p_T weight function.

133 PbPb MC simulations are also reweighted in order to match the centrality distribution in data.
 134 On the left panel of Figure 2, the centrality distribution of the MC simulation (red) is compared
 135 to the one in data (blue). On the right panel, MC is given the Ncoll weight and compared to
 136 the data. The unit (HiBin) on the x-axis corresponds 0.5% centrality.

137 In addition to the Bpt and centrality reweighting, it is known that the MB samples used for em-
 138 bedding PbPb signal MC samples (with Cymbal5Ev8 tune) has an offset in the primary vertex
 139 z position(PVz). This deviation is corrected by giving PVz weight. The procedure are shown in
 140 Fig. 3. The overall weight is given by the ratio between the two Gaussian functions. Note that
 141 this analysis is not sensitive to the absolute value of the PV position because the reconstruction
 142 of the B^+ meson rely only on the relative distance between PV and B^+ reconstructed vertex
 143 which is presented in the following section. We tried to estimate this effect by removing this
 144 re-weighting entirely and found that the difference is only 1.3%.

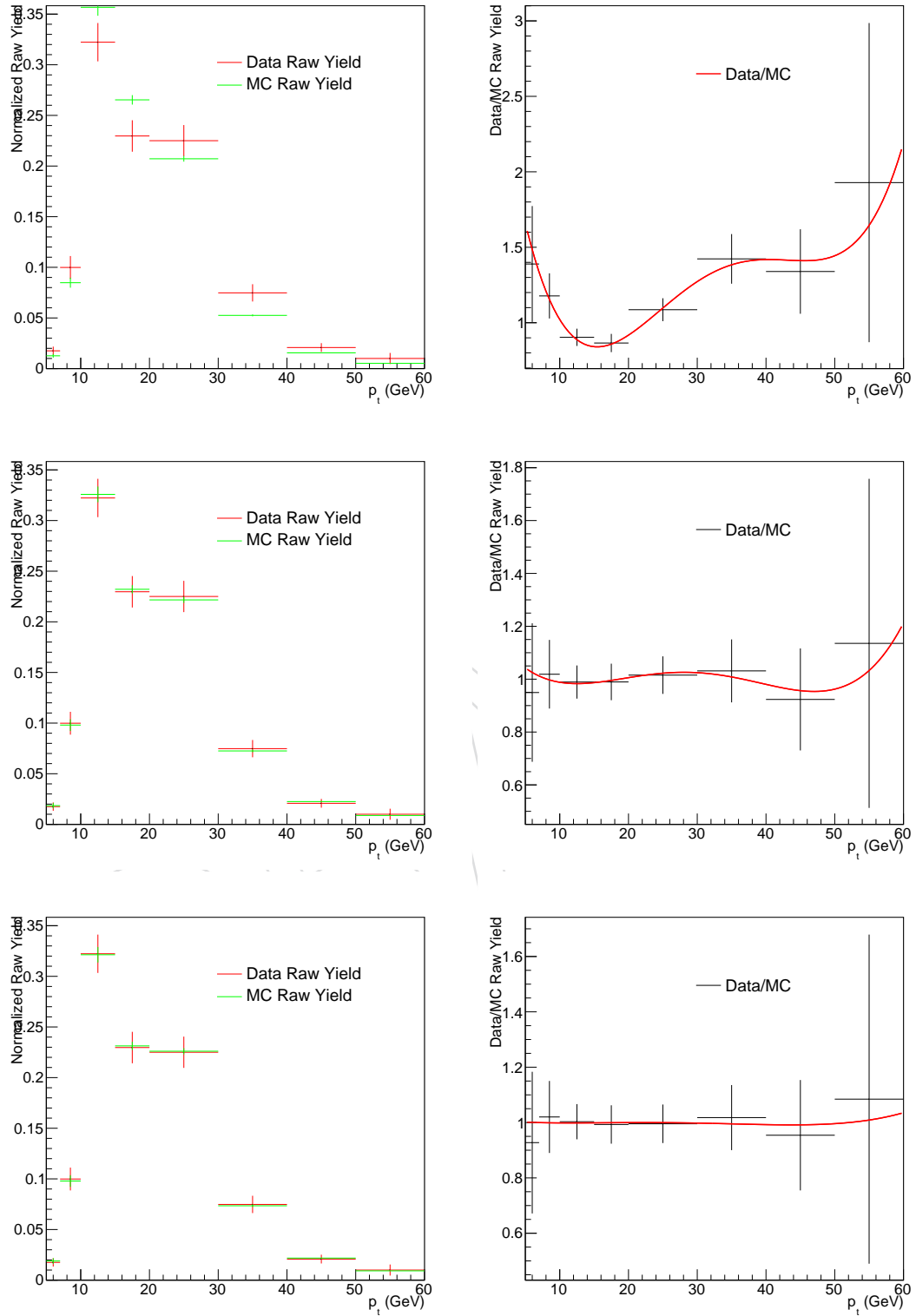


Figure 1: (Left) B^+ normalized raw yield distribution vs p_T in data and MC. (Right) The ratio of data and MC distribution and the 4th order polynomial fit. From the top to bottom we used no p_T weight, the 1st p_T weight, and the 2nd p_T weight in extracting the raw yield of MC.

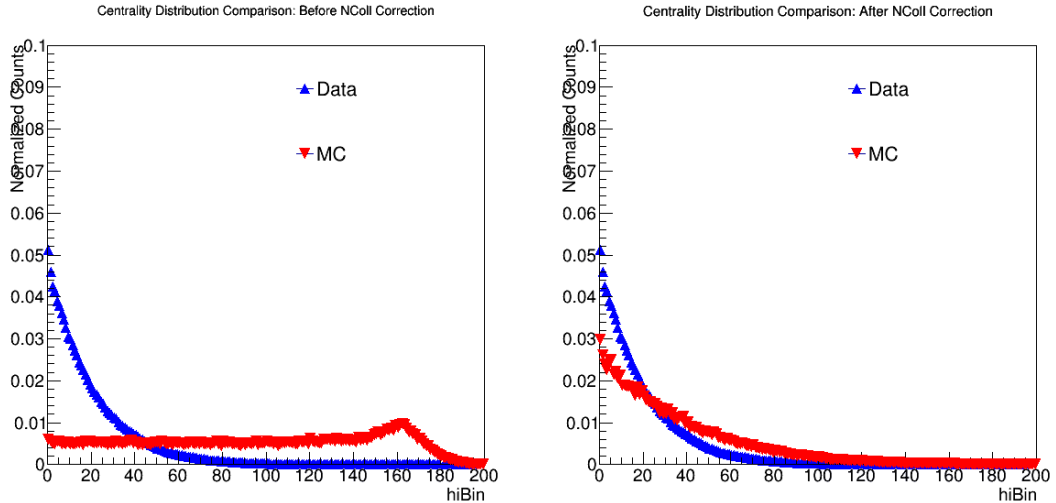


Figure 2: (Left) Centrality distribution of MC (red) and data (blue) in PbPb collisions in the centrality interval 0-100%. (Right) Centrality distribution of MC (red) and data(blue) where MC is weighed by Ncoll distribution.

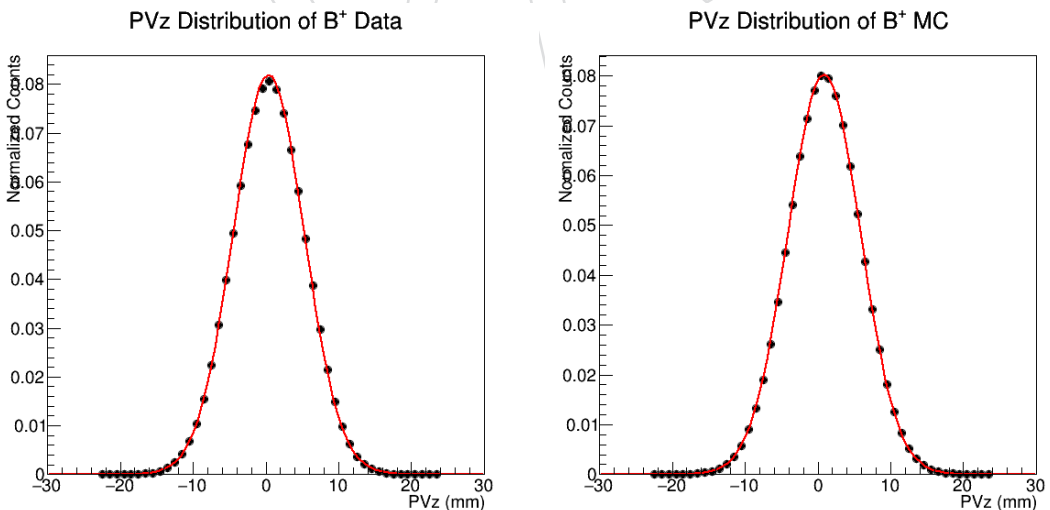


Figure 3: B^+ primary vertex z position(PVz) distribution and Gaussian fit obtained in PbPb Data and MC, respectively.

145 3 B^+ meson reconstruction

146 In this section, the B^+ meson reconstruction strategy is presented. The schematic diagram of
 147 the workflow is shown in Fig. 4, starting from muons and tracks to B^+ meson candidates.
 148 Muon candidates and tracks are required to pass several quality selection criteria as described
 149 in Section 3.1 and Section 3.2. J/ψ candidates are reconstructed by vertexing muon pairs with
 150 opposite charge, using KinematicConstrainedVertexFitter. The B^+ candidates are built by combining
 151 the J/ψ candidates with each of the selected tracks. Finally, a kinematic fit to the $J/\psi-K^+$ system
 152 is performed, forcing the mass of dimuon pair to be equal to the nominal J/ψ mass based on
 153 PDG [7]. The selection criteria of the B^+ candidates are described in Section 4.

154

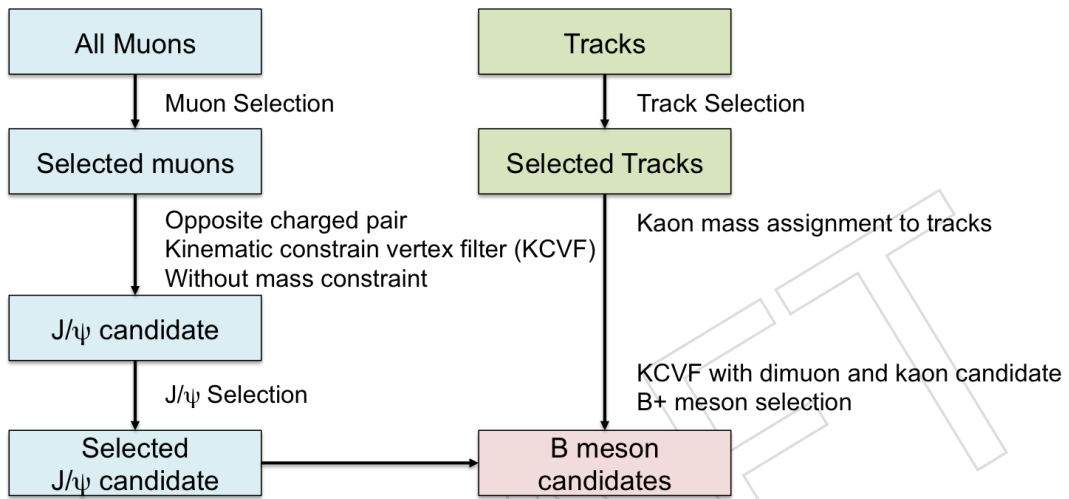


Figure 4: Schematic diagram of the B meson reconstruction workflow

155 3.1 Muon and J/ψ selection

156 We applied the same muon selection on B^+ with B_s^0 which is written exclusively on B_s^0 AN [1].

157 3.2 Track selection

158 The track selection we applied are the same with B_s^0 AN [1].

159 **4 B^+ meson selection**

160 The selections described in the previous section (so-called prefilter) are not sufficient to distin-
 161 guish signal from background, especially at low p_T range where the entire spectrum is dom-
 162 inated by combinatorial backgrounds which arises from random combination of muons and
 163 tracks. In order to see clear signals and reduce the uncertainties, several additional selection
 164 on the B^+ decay topology were then applied. A cut optimization procedure was performed to
 165 decide the cut values. For more details, see Section 4.1.

166 **4.1 Cut optimization**

167 The goal of the optimization procedure is to maximize the statistical significance of the signals
 168 while keeping reasonably high signal efficiencies. The optimal cut that minimizes background
 169 efficiency for a specific signal efficiency is obtained by the TMVA(Toolkit for Multivariate Data
 170 Analysis with ROOT) [8].

171 Boosted Decision Tree(BDT) is chosen to be the classification method in TMVA training for B^+ .
 172 In addition, for comparison the CutsGA (Genetic algorithm-based rectangular cut decision) is
 173 also examined. We found that in the lowest p_T bin(5-7GeV), the prefilter itself does not filter
 174 out background sufficiently, which limits the performance of BDT method. In order to enhance
 175 the performance, we first found the optimal rectangular cuts from CutsGA method in this p_T
 176 bin. After then we used normalized decay length(dls3D) and $\cos\theta$ (2D angle between B^+ meson
 177 displacement and B^+ meson momentum in transverse plane) cuts ($dls3D > 12.0 \cos\theta > 0.95$; this
 178 is slightly looser than the optimal rectangular cuts, in order not to reject possible signals that
 179 BDT can reconstruct but CutsGA cannot) in our prefilter for BDT training. This enhanced the
 180 raw yield extraction and reduced the yield error. We also applied this strategy to the p_T 7-10
 181 GeV/c bin with the selection ($dls3D > 9.0 \cos\theta > 0.92$) to enhance the performance. For other
 182 p_T bins, we just used the original prefilter for our BDT training.

183 The reconstructed candidates matched to the generated signal in MC sample are used as signal
 184 when training, while the reconstructed candidates in sideband ($0.15 \text{ GeV}/c^2 < |M_{B^+} - M_{B^+}^{PDG}|$
 185 $< 0.25 \text{ GeV}/c^2$) of data sample are used as background.

186 The kinematic variable distributions of daughter tracks and B^+ mesons before and after apply-
 187 ing the prefilter is shown on Figure 5, 6, 7, 8

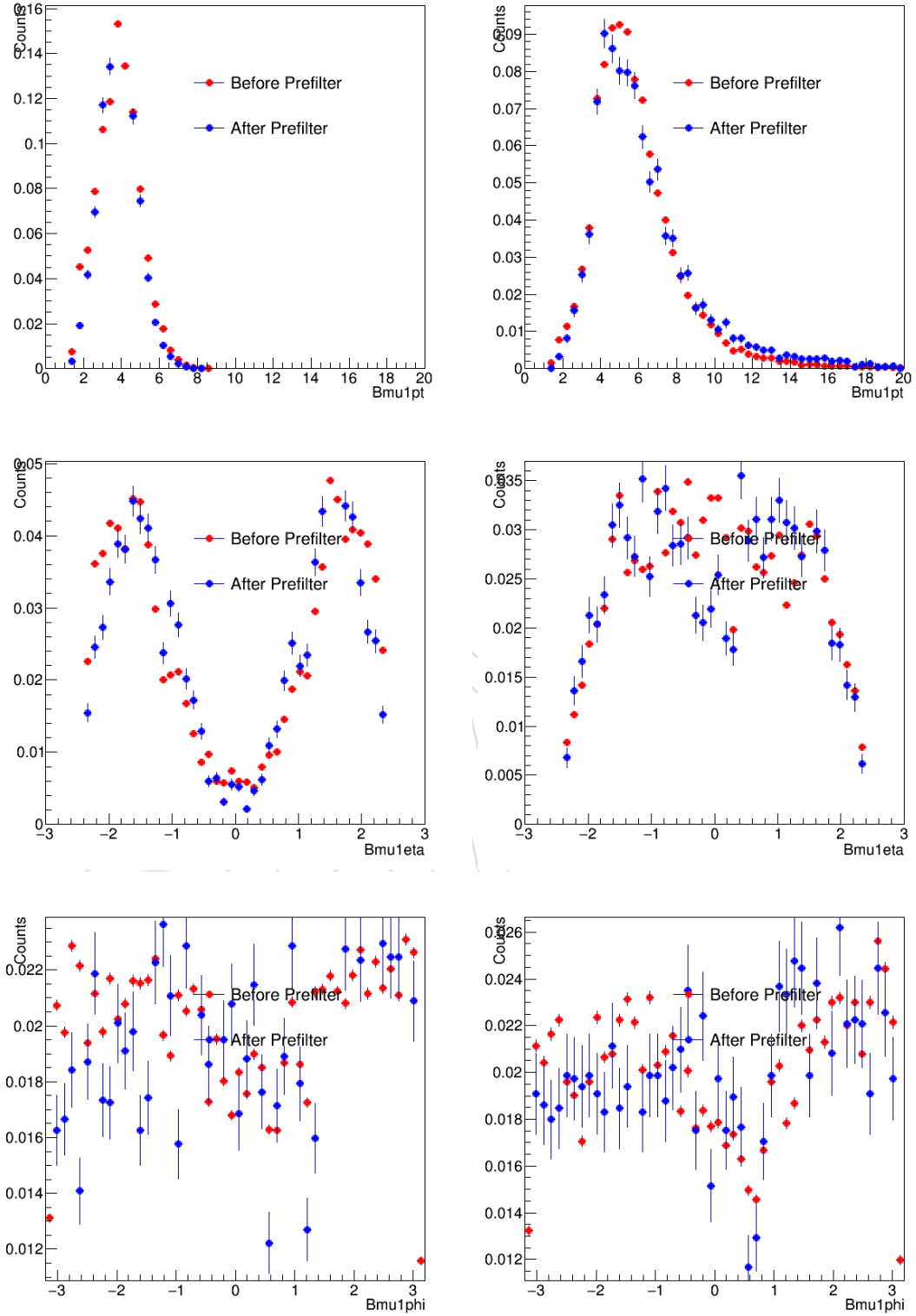


Figure 5: The normalized $J/\psi \mu^-$ kinematic variable distributions before and after prefilter for $p_T = 7 - 10 \text{ GeV}/c$ (left) and $10 - 50 \text{ GeV}/c$ (right) are shown above.

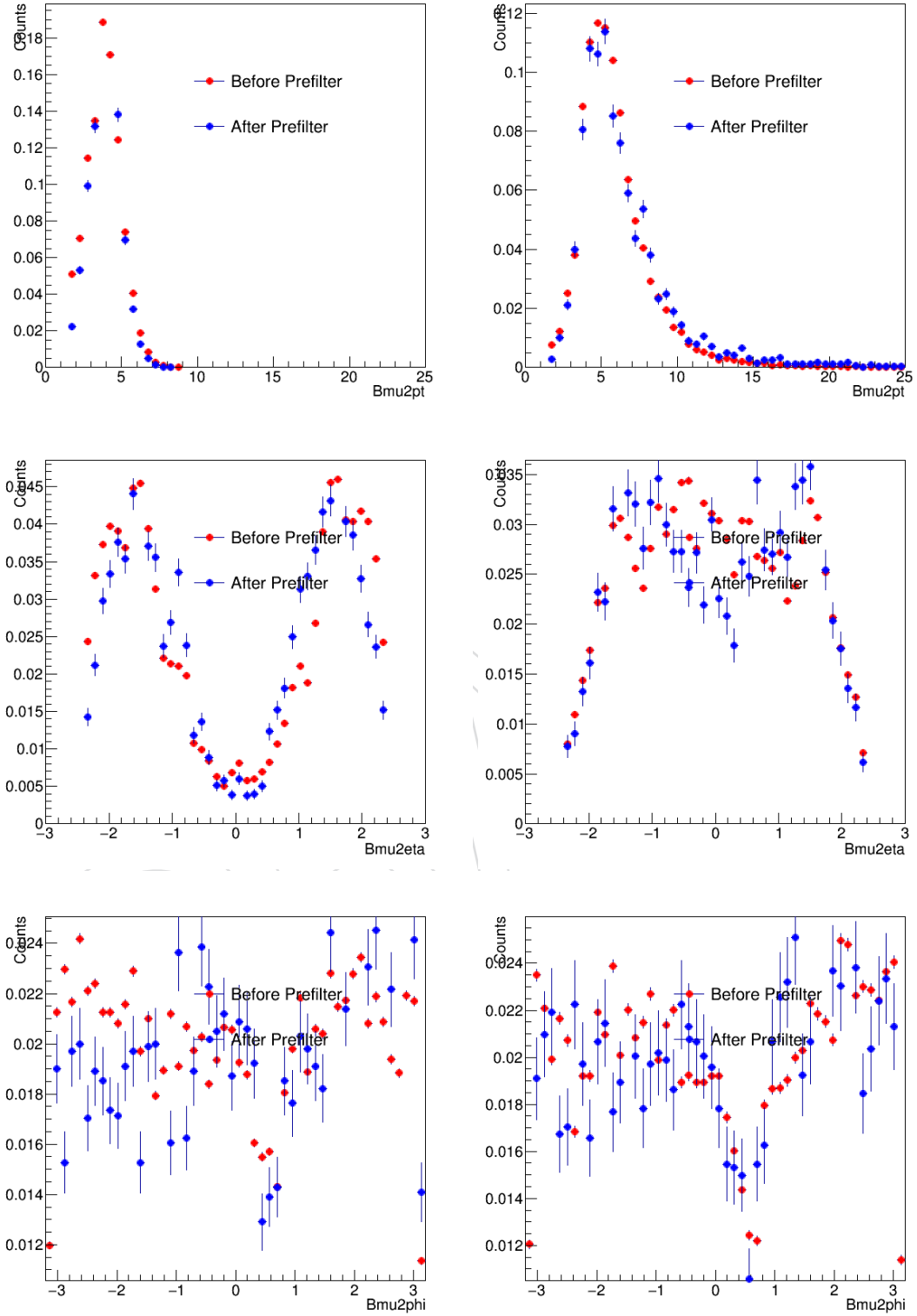


Figure 6: The normalized $J/\psi \mu^+$ kinematic variable distributions before and after prefilter for $p_T = 7 - 10 \text{ GeV}/c$ (left) and $10 - 50 \text{ GeV}/c$ (right) are shown above.

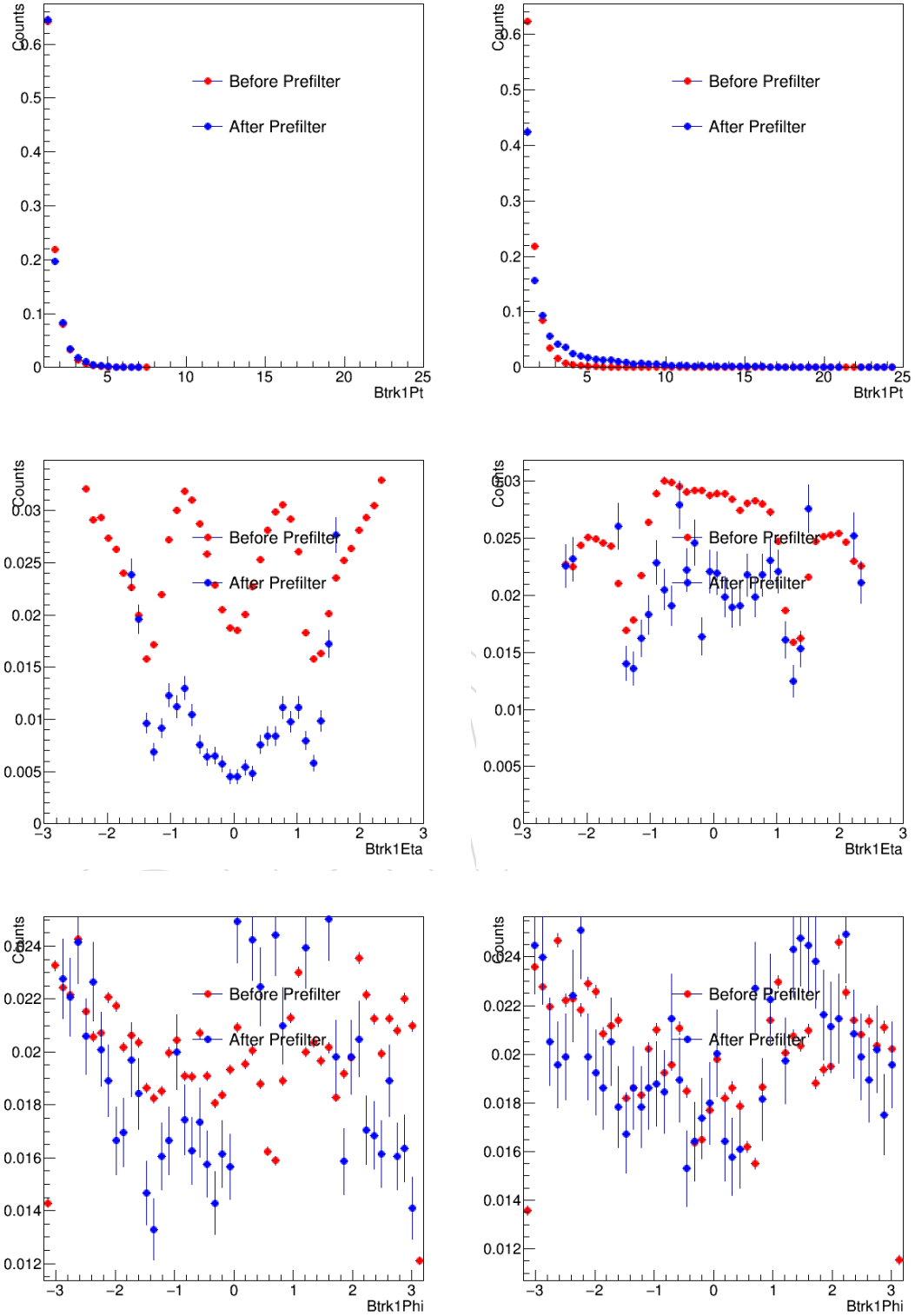


Figure 7: The normalized K^+ track, muons, and K^+ track kinematic variable distributions before and after prefilter for $p_T = 7 - 10 \text{ GeV}/c$ (left) and $10 - 50 \text{ GeV}/c$ (right) are shown above.

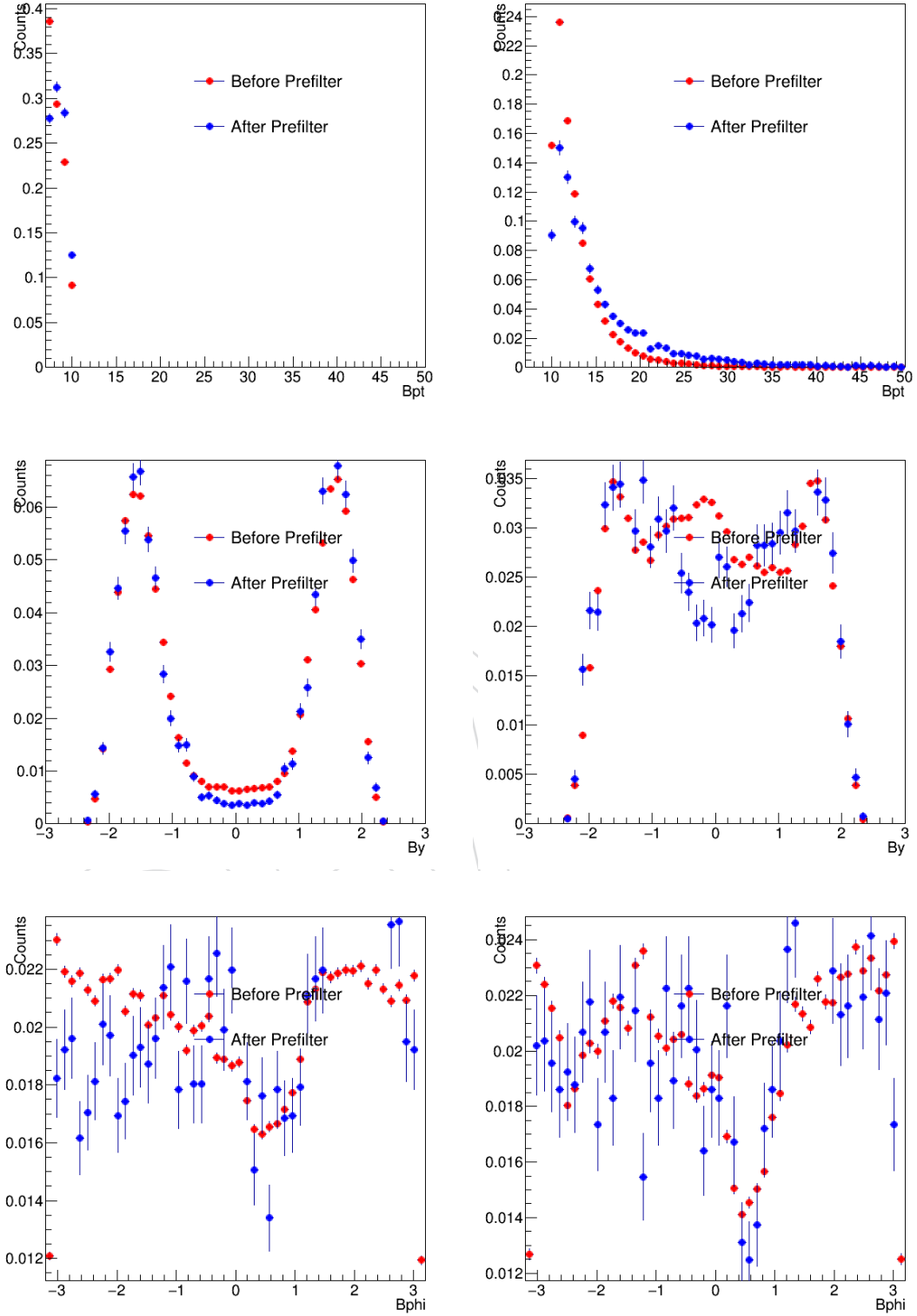


Figure 8: The normalized B^+ kinematic variable distributions before and after prefilter for $p_T = 7 - 10 \text{ GeV}/c$ (left) and $10 - 50 \text{ GeV}/c$ (right) are shown above.

188 We can see that the prefilter cuts do not significantly change the distribution of the kinematic
189 variable shapes and create potential bias. Therefore, these show that our prefilter cut is valid
190 to use.

191 Then, we use the following six selection variables trained for PbPb:

- 192 • dls3D: Normalized decay length (SV PV distance), the distance between primary
193 and B^+ decay (secondary) vertex normalized by its uncertainty
- 194 • Balph: The angle between B^+ meson displacement and B^+ meson momentum in
195 3D
- 196 • Btrk1Pt: Track p_T , the transverse momentum of the track
- 197 • Bchi2cl: χ^2 probability, the χ^2 probability of the secondary decay vertex fitting
- 198 • Btrk1Eta: The absolute value of the track pseudorapidity
- 199 • Btrk1Dxysig: Normalized track Dxy, the transverse distance between track and the
200 primary vertex normalized by its uncertainty

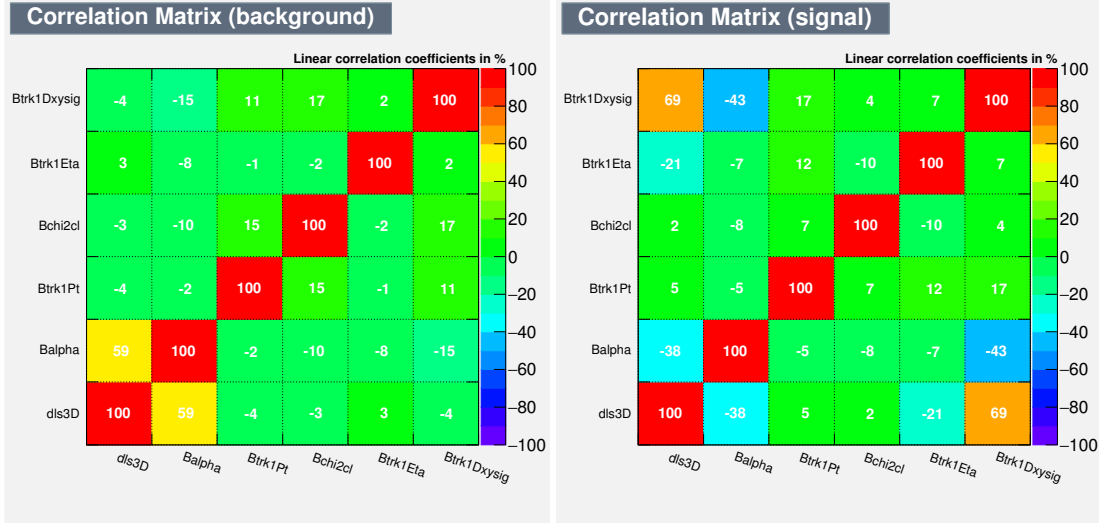
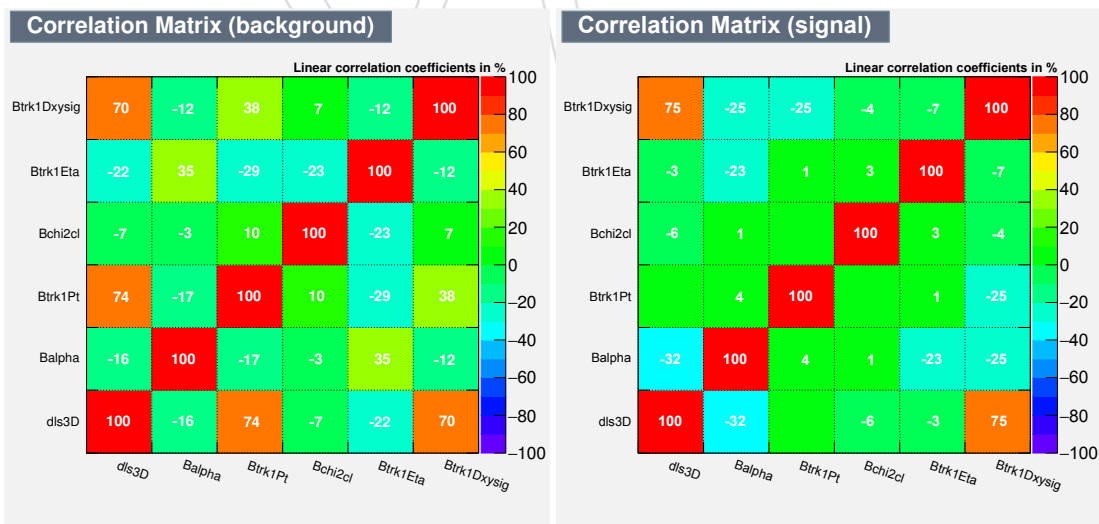
201 The BDT training setup for all p_T bins are as follows: NTree = 850, MinNodeSize=2.5%, MaxDepth=3,
202 BoostType=AdaBoost, AdaBoostBeta=0.5, UseBaggedBoost, BaggedSampleFraction=0.5, Sepa-
203 rationType=GiniIndex, nCuts=20

204 The optimal BDT cut values are defined as the numbers which maximize the figure of merit(statistical
205 significance) $S / \sqrt{S + B}$. Here, S is the number of signal in signal region after applying optimal
206 cuts, while B is the number of background in signal region after applying optimal cuts. Signal
207 region is defined as $|M_{B^+} - M_{B^+}^{PDG}| < 0.08 \text{ GeV}/c^2$. For the lowest p_T bin, we used a new figure
208 of merit $S / \sqrt{\gamma_{\text{quantile}}(\alpha/2, S + B, 1)}$ (where, α is chosen to be 1-0.6827) that is suitable for this
209 low signal/background ratio.

- 210 • $S = S' \times (\text{signal optimal cut efficiency})$, where S' is the number of signal in signal
211 region before applying optimal cuts.
- 212 • $B = B' \times (\text{background optimal cut efficiency})$, where B' is the number of background
213 in signal region before applying optimal cuts.

214 S' and B' are calculated by fitting the invariant mass plot with prefilter selection, with the same
215 functional form used in the main analysis. However, at the 4 lowest p_T bins, the prefilter is not
216 sufficient to reveal the signal. In those cases, S' is calculated by the expected number of signal
217 from FONLL pp cross-section calculation multiplied by pre-filters efficiency, acceptance from
218 MC, and expected R_{AA} value from previous measurement [5].

219 Fig. 9 and Fig. 10 show the correlation matrices of the training, in the lowest and highest p_T
220 bin, respectively.

Figure 9: TMVA training correlation matrices of PbPb in p_T 5 - 7 GeV/c.Figure 10: TMVA training correlation matrices of PbPb in p_T 50 - 60 GeV/c.

221 Fig. 11 shows the overtraining check in the lowest and the highest p_T bin.

222

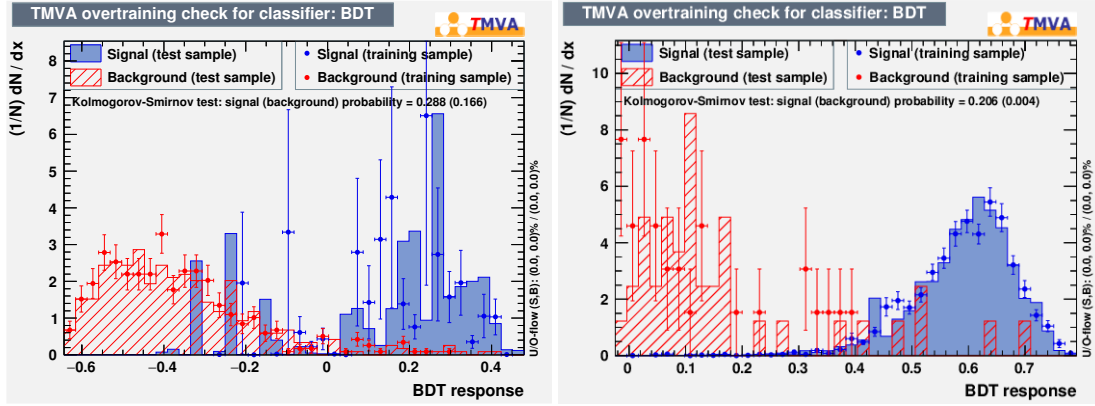


Figure 11: TMVA overtraining check of PbPb in p_T 5-7 and 50 - 100 GeV/c, respectively

223 Fig. 12 shows the variable distribution comparison between signal and background, and the
224 statistical significance curve in p_T 15-20GeV. Some variables show prominently distinct distribu-
225 tion between signal and background.

226

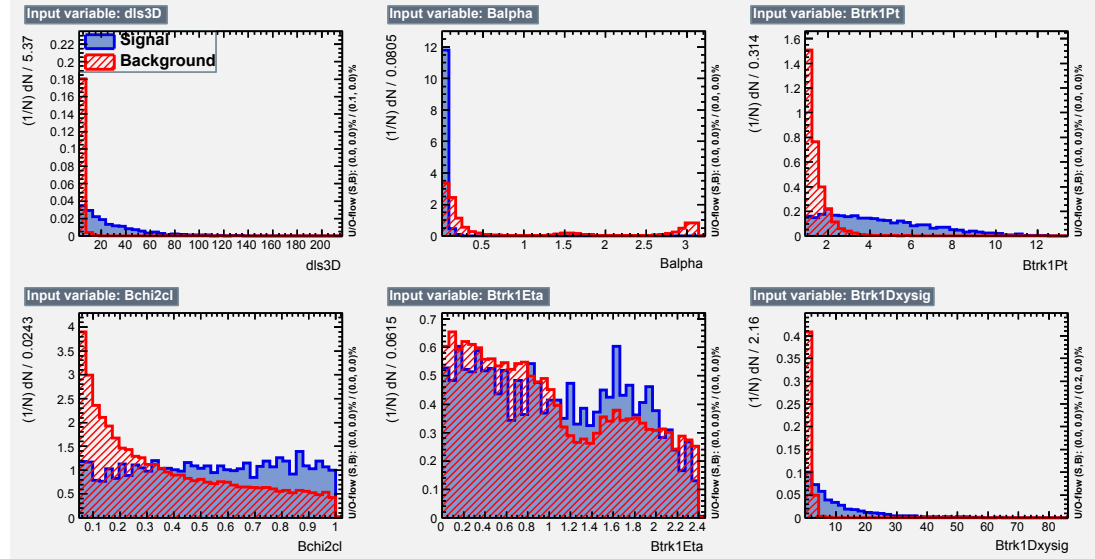


Figure 12: TMVA training variable distribution of PbPb in p_T 15 - 20 GeV/c.

- 227 The maximum significance point is selected as our nominal working point, as shown in Fig. 13.
 228 Tab. 1 shows the summary of the optimal selection criteria in different p_T intervals.
 229 All the other TMVA performance plots not listed in this section are on Appendix. A.

230

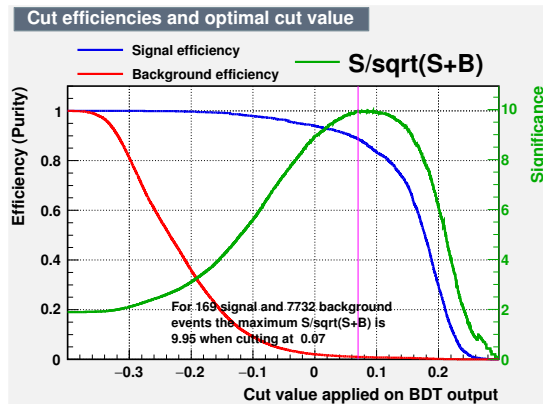


Figure 13: TMVA significance curve of PbPb in p_T 15 - 20 GeV/c.

p_T (GeV/c)	5-7	7-10	10-15	15-20	20-30	30-40	40-50	50-60
BDT	>0.02	>0.03	>0.09	>0.07	>0.10	>0.16	>0.20	>0.27

Table 1: Summary table of selection criteria in different p_T intervals in PbPb collisions

231 **4.2 Fiducial region**

232 As we go to low B^+ p_T where the daughter particles also have predominantly low p_T , it be-
 233 comes improbable to detect muons in low rapidity ranges due to the limited acceptance of the
 234 muons. In other words, the signal and background candidates of B^+ are largely confined to for-
 235 ward rapidity region at low B^+ p_T . Fig 14 shows theoretically possible inverse of acceptance,
 236 selection efficiency, and total efficiency vs B^+ p_T and $|y|$ 2D distribution with only single muon
 237 and track selections but without BDT selections.

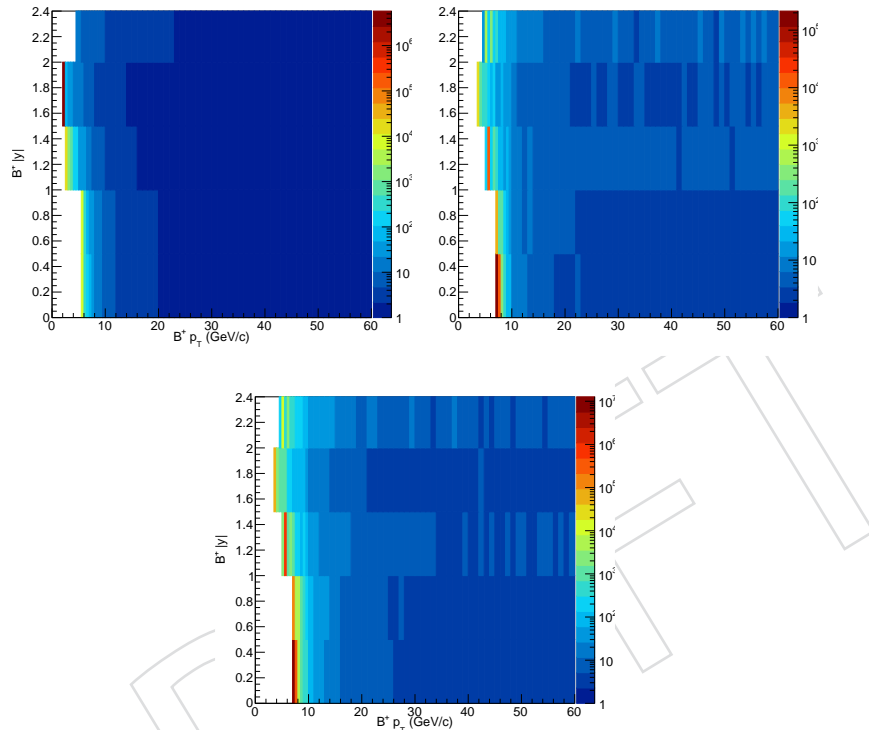


Figure 14: The two dimensional maps of the inverse of the acceptance efficiency (left), selection efficiency (middle), and total efficiency (right) vs B^+ p_T and rapidity in MC for the centrality range of 0 - 90% without applying BDT cuts are shown above.

238 Next, we quantitatively examine the 2D maps of candidate distributions in both data and MC
 239 after applying the optimal BDT selections, which are shown in Fig. 15.
 240 It is found that B^+ acceptance is better than B_s^0 , presumably because of less number of tracks
 241 needed to reconstruct B meson, which allows broader phase space that the daughter particles
 242 can reside. Since this analysis is mainly for the comparison with B_s^0 , we adopted more strict
 243 fiducial region ($5 < p_T < 10 \text{ GeV}$, $1.5 < |y_{lab}| < 2.4$) that is defined using B_s^0 2D map.

244

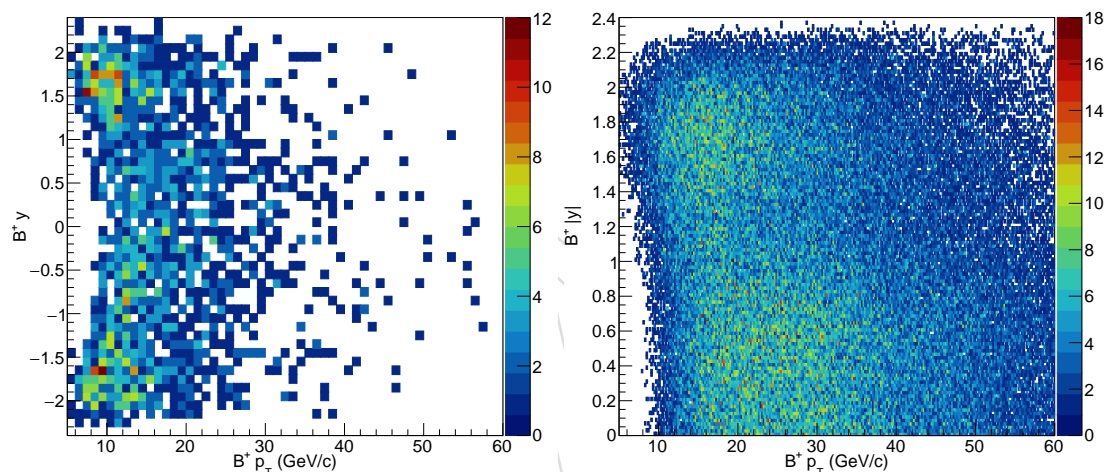


Figure 15: B^+ p_T and rapidity two dimensional map of candidates that passed the full analysis cut in data (Left) and MC (right).

245 5 MC-Data Comparison

246 5.1 B candidate properties comparison between data and MC

247 Potential differences between Data and MC distributions of the variables used for the selection
 248 of the B^+ signal, can introduce biases in the efficiency corrections. In this section, the distribu-
 249 tions of the B^+ selection variables in PbPb data and MC samples are compared.

250

251 The Splot method is used for our analysis. This is a likelihood-based method by which we
 252 reweight the data using the unbinned fit result. The weights are added to the dataset based on
 253 model and yield extraction variables. Each event has two weights: probability of belonging to
 254 the signal given its mass, probability of belonging to the background given its mass. The Splot
 255 class gives us the distributions of our variables for a given species (signal or background). The
 256 advantage of using this method is that we use the full dataset for the comparison in contrast to
 257 the sideband subtraction method where one should select the investigation range of signal and
 258 background. Furthermore, we use likelihood to describe events' behavior in contrast to the po-
 259 tential misidentification of signal events in background region which might occur in sideband
 260 subtraction method. For more details on general description of Splot method applied to this
 261 analysis, please refer to the section 4 and 5 of the analysis note CMS AN-19-219([9]).

262

263 To show the correlations between the BDT variables to the B^+ invariant mass and validate
 264 our Splot techniques approach, we first make the correlation matrices for BDT variables vs B^+
 265 invariant mass Bmass for data and MC as follows in Figure 16:

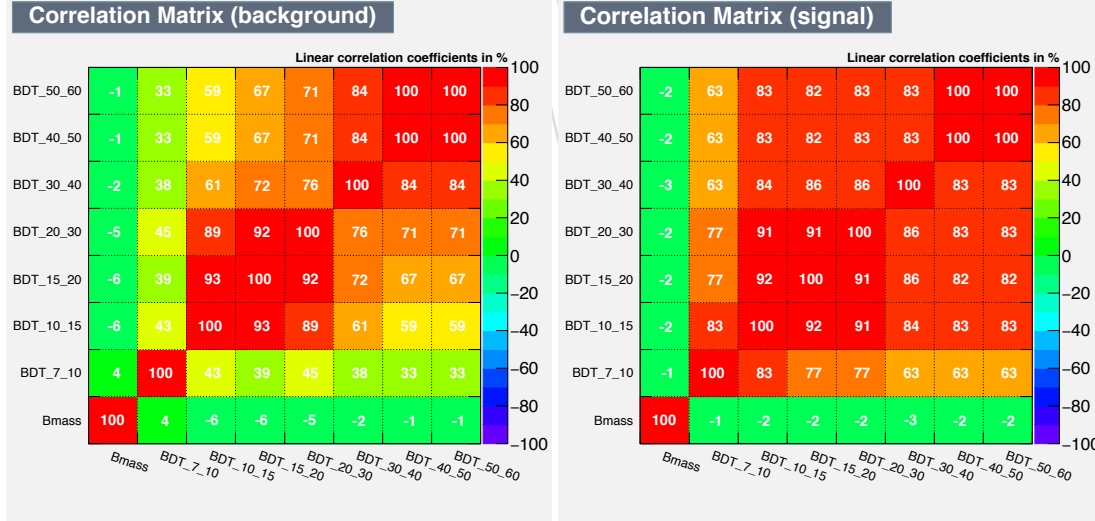


Figure 16: The correlation matrices in data (left) and MC (right) are shown above.

266 Fig. 17 shows the data and MC comparison results based on Splot method. Here, we focus
 267 on BDT values that are directly used in our signal extraction and related to MC distribution
 268 validation, rather than the variables themselves used in BDT training. In a wide ranges of BDT,

- ²⁶⁹ the two distributions show good agreement. We only focus on the region where BDT is greater
²⁷⁰ than the working point and is smaller than the maximum value that candidates have.

DRAFT

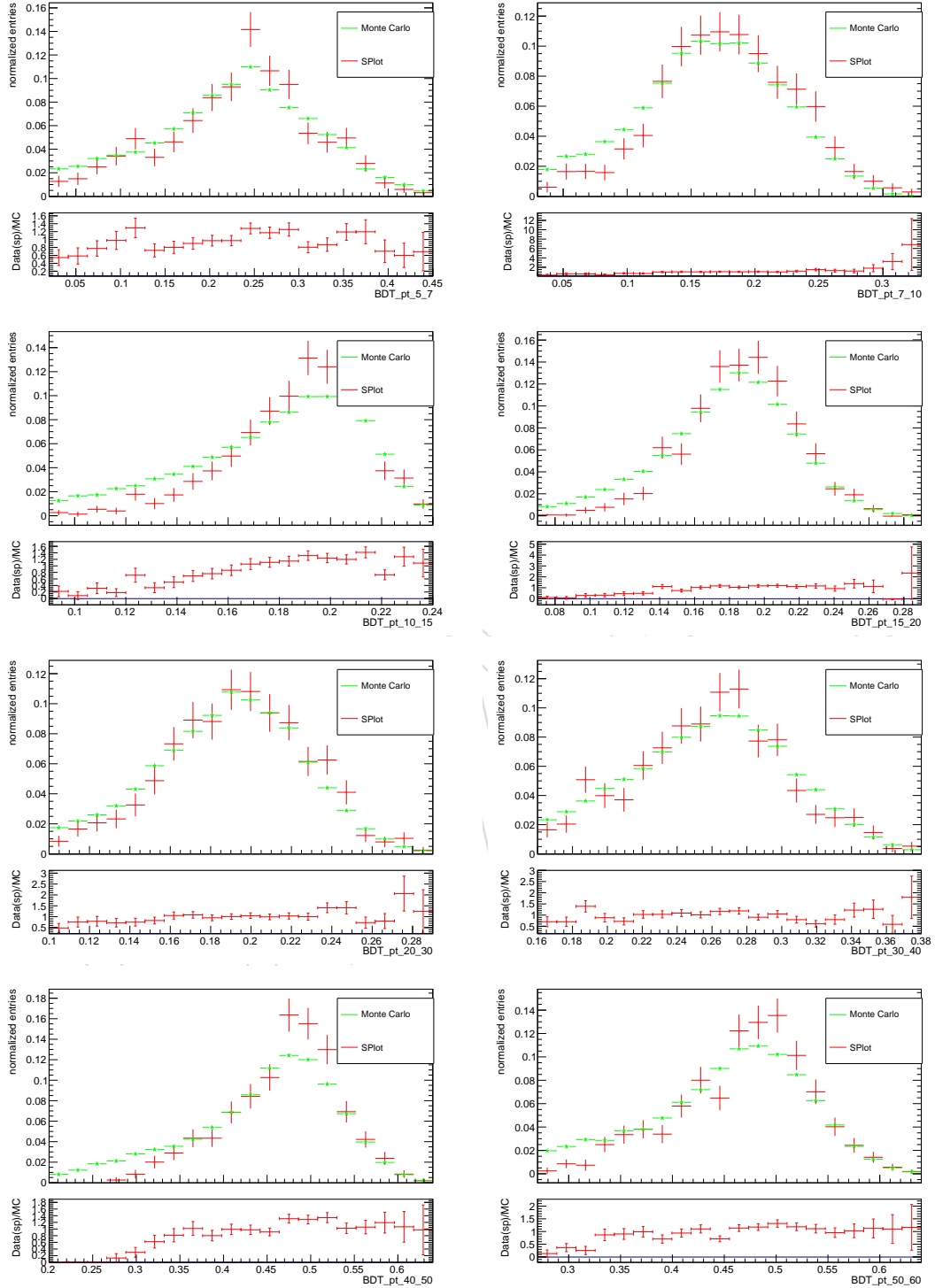


Figure 17: Comparison of B^+ BDT distribution in data and MC using Splot method.

271 6 Signal Extraction

272 The method and the fit model for signal and background we applied are mostly the same with
 273 B_s AN. Please refer to the corresponding section in [1].

274 However, there is one major difference between B_s and B^+ yield extraction. From the inclusive J/ ψ sample study, we have found that there is a clear and sizable contribution from non-
 275 prompt J/ ψ candidates that are fed down from the B^+ signal in our region of interest. We model
 276 this component with an error function and a Gaussian. The error function component mostly
 277 comes from 4-prong B meson decay (e.g. $B^+ \rightarrow J/\psi K^*(892)^+$) that are partially reconstructed
 278 as $B^+ \rightarrow J/\psi K^+$ (one track is lost) and can form peaking structures for values of the invariant
 279 mass below $\approx 5.20 \text{ GeV}/c^2$. The Gaussian contribution mainly comes from $B^+ \rightarrow J/\psi \pi^+$ where
 280 pion is misidentified as kaon.

281 The ratio of the height of error function and the Gaussian is fixed by MC simulation. However,
 282 the Gaussian component is shown to be relatively negligible compared to the error function,
 283 and even more to the signal double Gaussian of our nominal channel. More details on the non-
 284 prompt J/ ψ study can be found in Appendix Sec. B.

285 Note that we do not discriminate B^+ from B^- in raw yield extraction process. Therefore, the
 286 invariant mass plots shown below contains both B^+ and B^- signal and backgrounds. This dou-
 287 ble counting is properly canceled in the corrected yield calculation process later.

289

290 In Fig. 18 and Fig. 19, the invariant mass spectra and their pull distributions obtained in the p_T
 291 intervals in the PbPb analyses are presented.

292 We also make the comparison between the symmetric raw yield error and their asymmetric
 293 upper and lower yield error using the RooFit framework on the unbinned fit. The table is
 294 shown below in Table 2:

Table 2: The comparison between RooFit and unbinned fit framework.

Centrality	p_T (GeV/c)	Raw Yield Error	Raw Yield Error Up	Raw Yield Error Down
0 - 90%	7 - 10	10.88	11.20	10.66
0 - 90%	10 - 15	20.68	21.05	20.35
0 - 90%	15 - 20	17.86	18.21	17.56
0 - 90%	20 - 50	19.84	20.19	19.55
0 - 30%	10 - 50	27.72	28.01	27.45
30 - 90%	10 - 50	19.53	19.92	19.20
0 - 90%	10 - 50	33.78	34.13	33.47

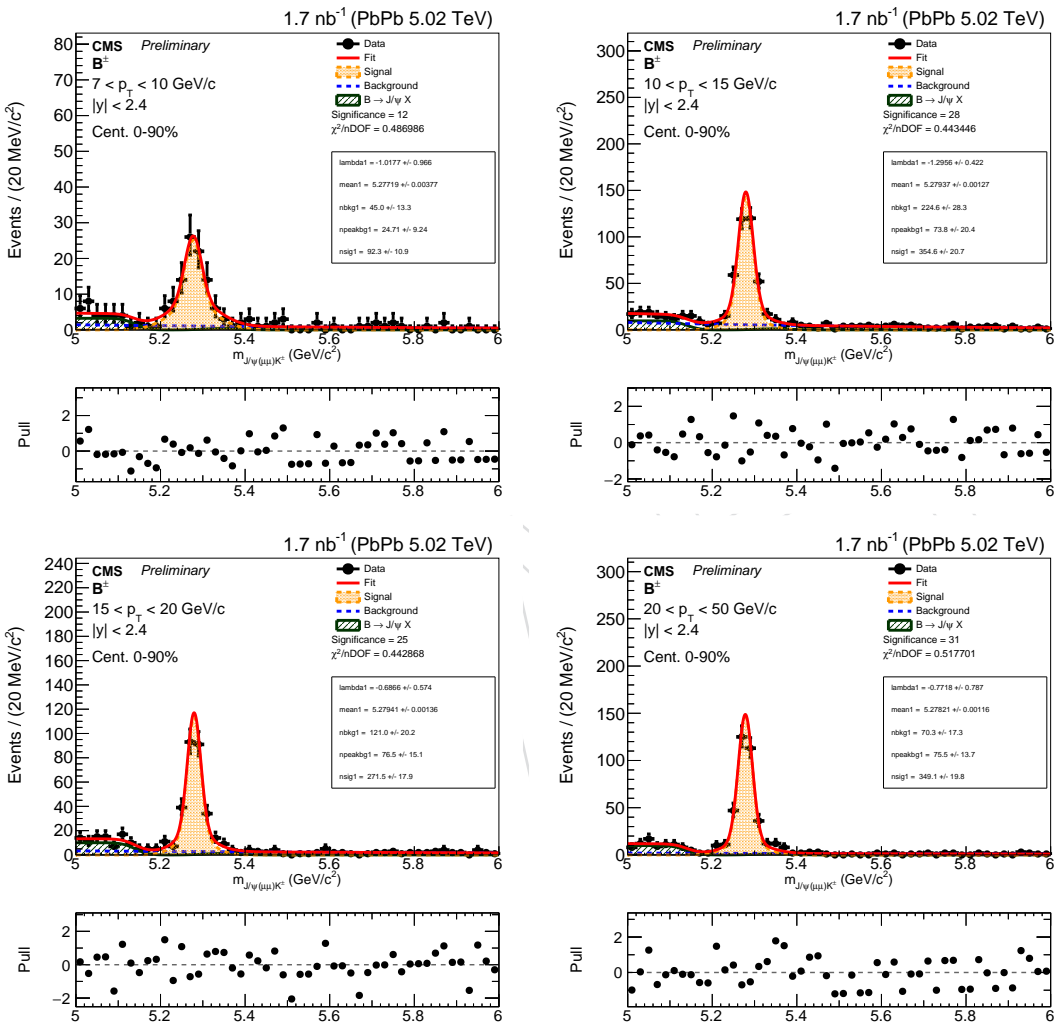


Figure 18: Invariant mass distribution of B^+ candidates obtained in PbPb collisions in p_T intervals in the transverse momentum range from 7-50 GeV/c and Centrality 0-90%.

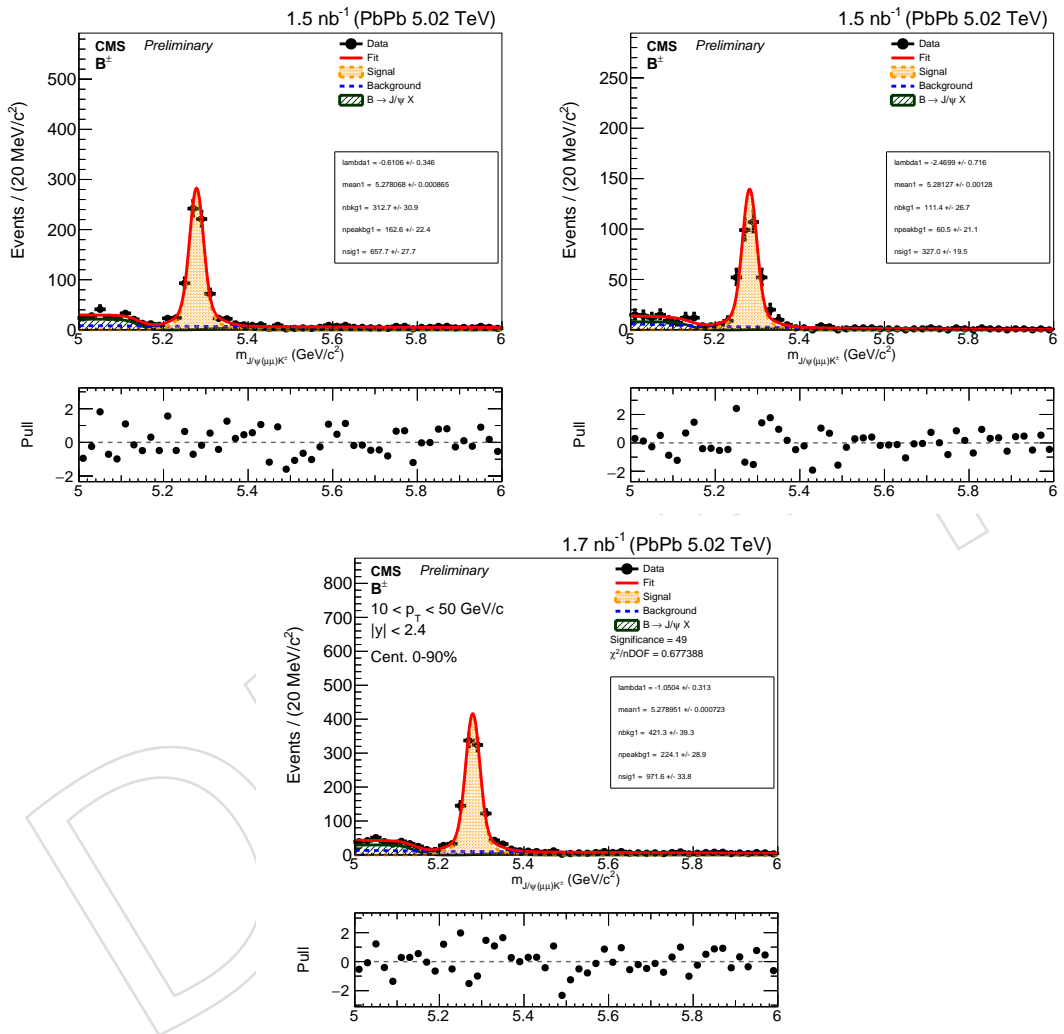


Figure 19: Invariant mass distribution of B^+ candidates obtained in PbPb collisions in centrality intervals 0 - 30%, 30 - 90%, and 0 - 90% in the transverse momentum range from 10 - 50 GeV/c.

295 **6.1 Closure test of the fitting procedure**

296 In order to validate the yield extraction procedure, we generate 5000 toy MC for the fit and
 297 make the pull distribution. Then we perform the Gaussian fits to the pull distribution to obtain
 298 the mean and width. The results are show in Fig 20 and Fig 21:

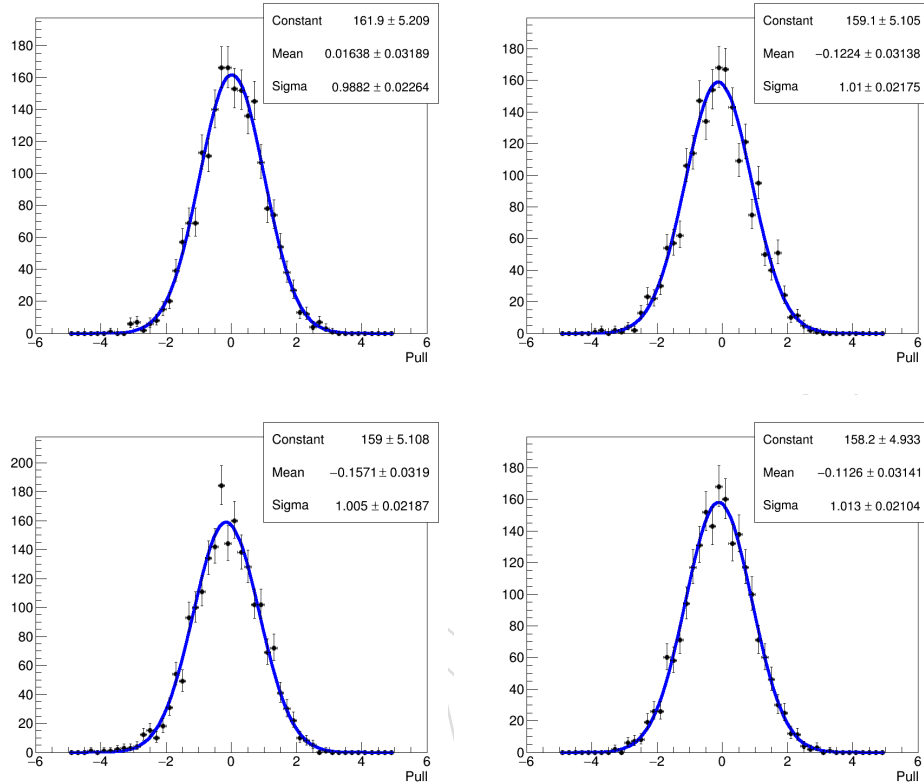


Figure 20: The pull distribution and the Gaussian fits for 0 - 90% at 7 - 10, 10 - 15, 15 - 20, 20 - 50 are shown respectfully above.

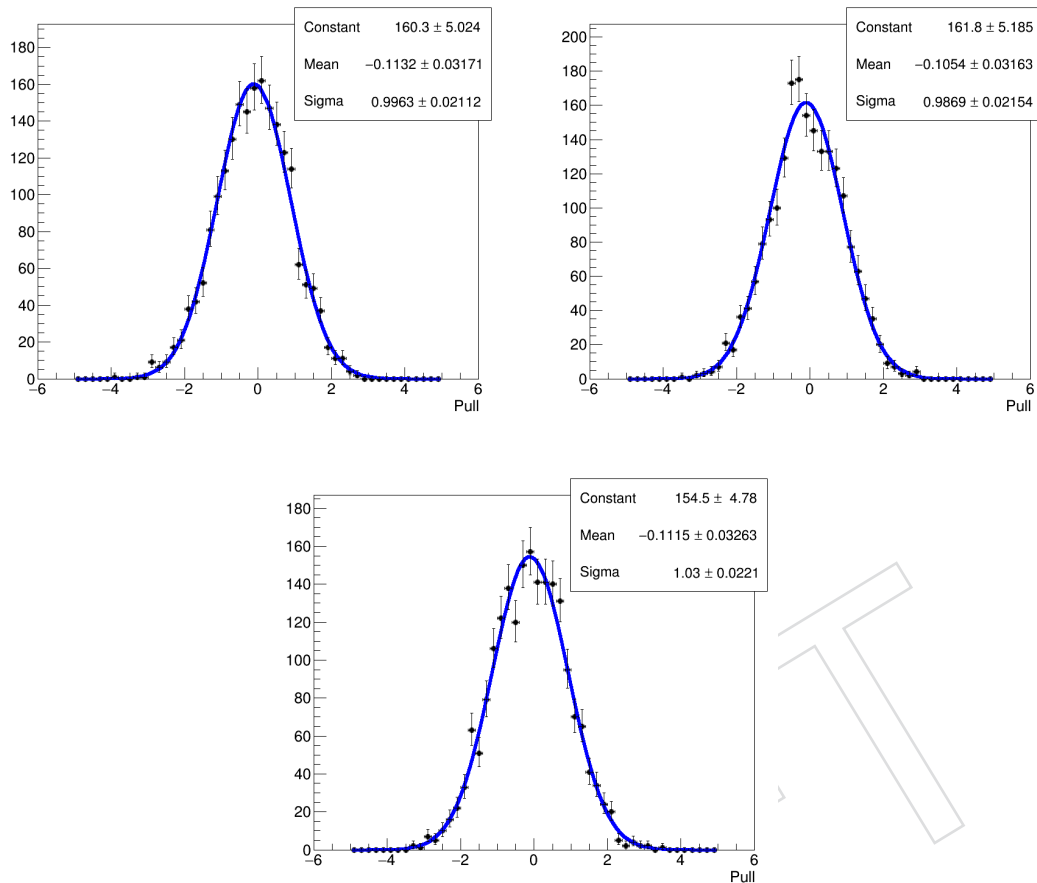


Figure 21: The pull distribution and the Gaussian fits for 0 - 90% at 7 - 10, 10 - 15, 15 - 20, 20 - 50 are shown respectfully above.

299 We can see that all p_T and centrality bins have zero mean and unit width from the Gaussian fits
 300 to the pull distribution. This validate the closure of our fits to extract the B^+ raw yield.

301 **7 Acceptance and Efficiency**

302 We used the same method with B_s AN. For more details not described fully in this section,
303 please refer to B_s AN.

304 **7.1 Muon Efficiency Correction: Tag-and-Probe**

305 When we do the efficiency corrections, there are inherent scaling factor and uncertainties that
306 comes from muon reconstruction with respect to muon track reconstruction, muon id, and trig-
307 ger efficiency. This is considered by Tag-and-Probe(TnP) study primarily done by the dilepton
308 group.

309

310 We used the header file of muon efficiency in the following link here: <https://github.com/>
311 CMS-HIN-dilepton/MuonAnalysis-TagAndProbe/blob/103X_HI/macros/tnp_weight_

312 lowptPbPb.h

313

314 We obtained TnP factors by looping over all candidates in MC that passed prefilter, BDT se-
315 lection, and gen-match condition. We use the J/ψ L3 filter as our trigger scale factor for TnP
316 efficiency corrections. The tag and probe efficiency as a function of muon p_T and η according
317 to the header file are shown below on Fig 22, 23, and 24:

DRAFT

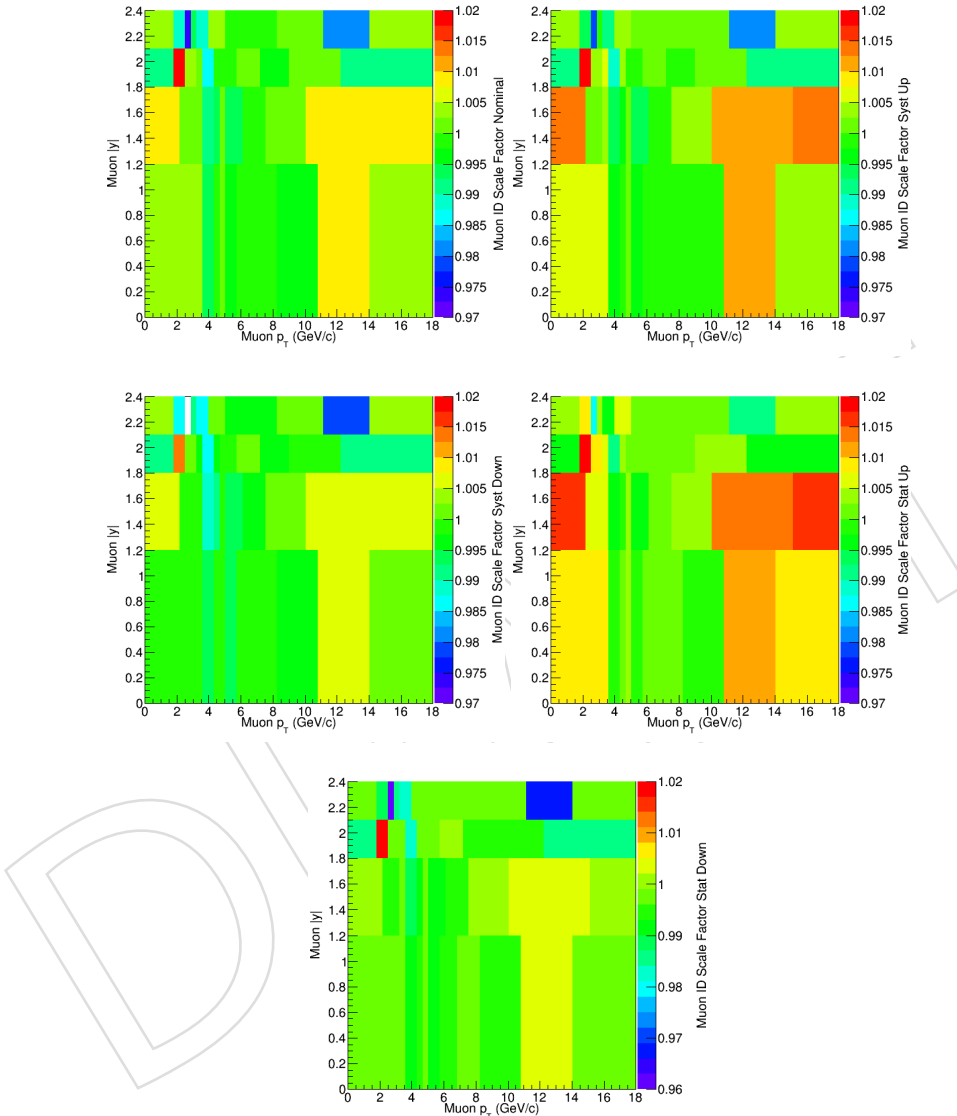


Figure 22: The muon identification scaling factor from the header file of the dilepton group is shown above. From top left to bottom right respectfully: nominal, systematic 1 sigma down, systematic 1 sigma up, statistical 1 sigma up, and statistical 1 sigma down.

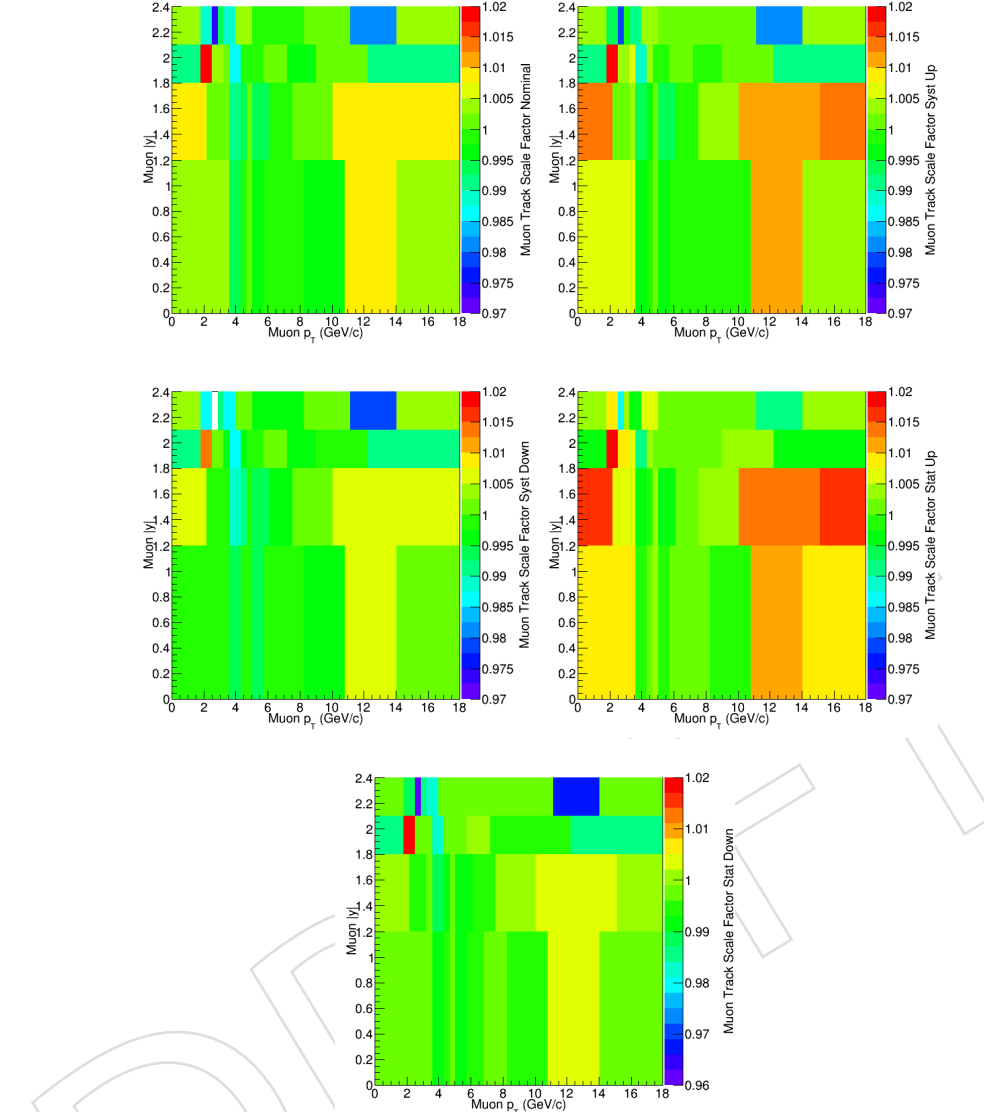


Figure 23: The muon track scaling factor from the header file of the dilepton group is shown above. From top left to bottom right respectfully: nominal, systematic 1 sigma down, systematic 1 sigma up, statistical 1 sigma up, and statistical 1 sigma down.

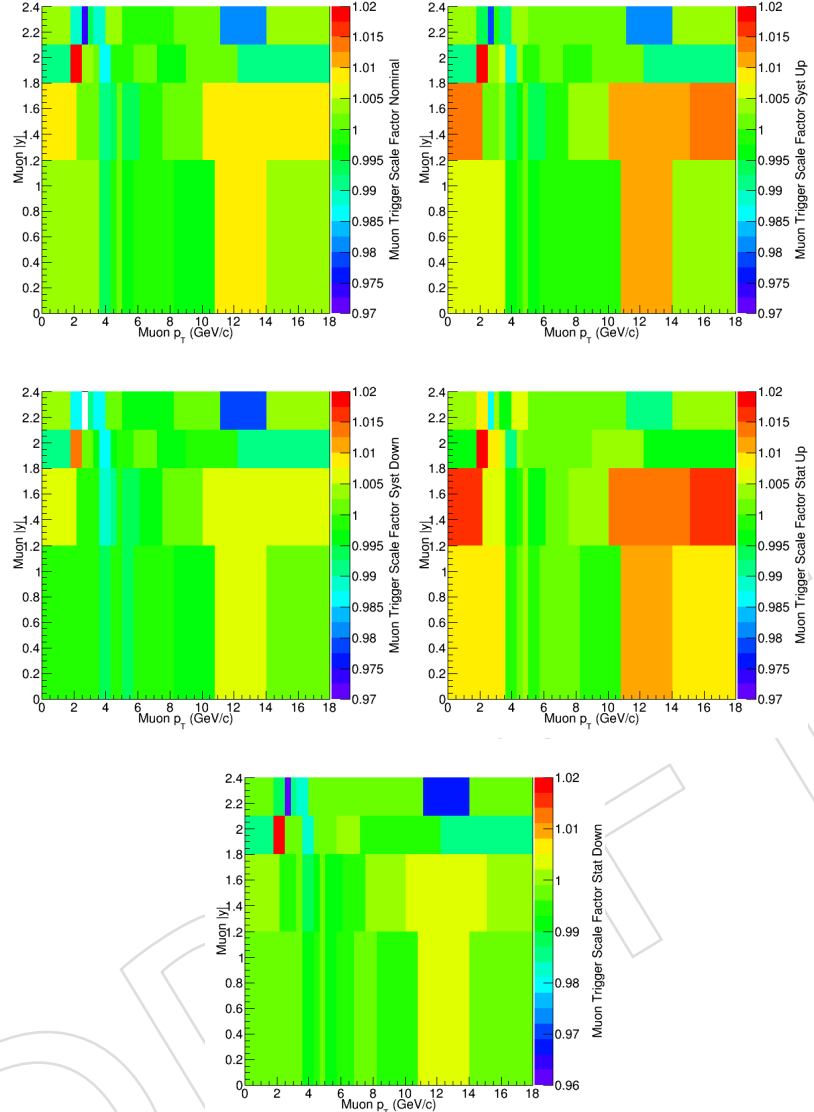


Figure 24: The muon L3 filter trigger scaling factor from the header file of the dilepton group is shown above. From top left to bottom right respectfully: nominal, systematic 1 sigma down, systematic 1 sigma up, statistical 1 sigma up, and statistical 1 sigma down.

318 We vary the correction factor to up and down with `trg, trk, muid` error, and the correction factor
 319 change compared to nominal one is considered as the uncertainty. then syst and stat are com-
 320 bined by $Error = \sqrt{syst^2 + stat^2}$. We read muon p_T and pseudorapidity of each event, and then
 321 obtained weight (scale) factor and its uncertainties from the header file according to the kine-
 322 matics. We recorded the scale and uncertainties in B^+ rapidity and p_T 2D map, and propagated
 323 into our analysis workflow to obtain the nominal efficiency correction factor and the related
 324 systematic uncertainties. The binnings of 2D map we used are, $B^+ |y_{lab}|$ 0.0-0.5-1.0-1.5-2.0-2.4,
 325 p_T unit 0.5GeV within 5-10GeV and unit 1GeV within 10-60GeV.

326

327 The following figures show the TNP scaling and the uncertainties in 2D map. The scaling
 328 factors are directly applied to our acceptance and efficiency calculation shown in the next sub-
 329 section.

330

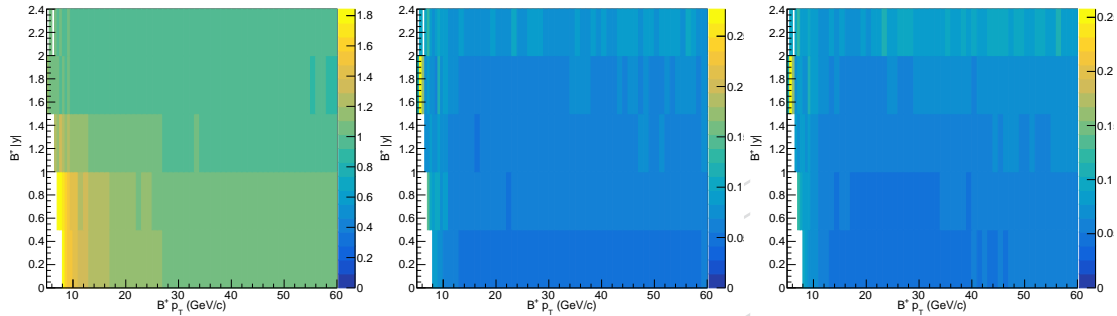


Figure 25: B^+ TnP in centrality 0 - 30% range. (Left) TnP scaling factors. (Middle) TnP scaling factor uncertainties(up). (Right) TnP scaling factor uncertainties(down).

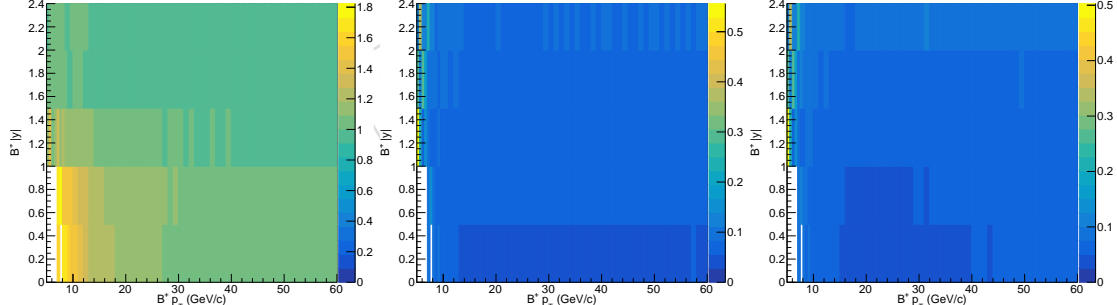


Figure 26: B^+ TnP in centrality 30 - 90% range. (Left) TnP scaling factors. (Middle) TnP scaling factor uncertainties(up). (Right) TnP scaling factor uncertainties(down).

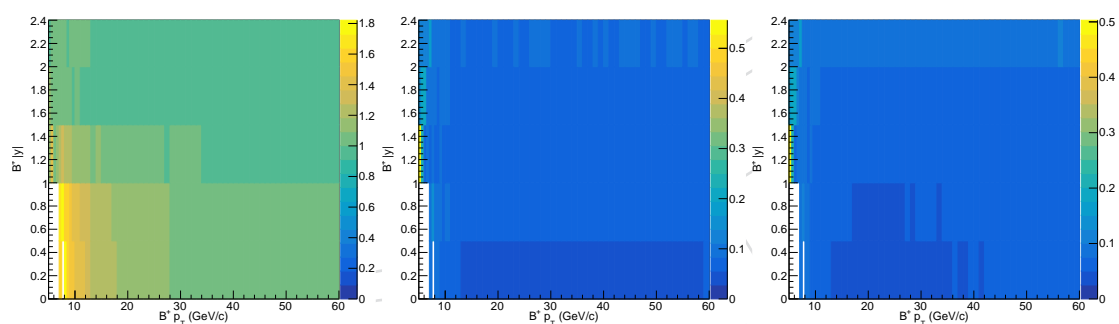


Figure 27: B^+ TnP in centrality 0 - 90% range. (Left) TnP scaling factors. (Middle) TnP scaling factor uncertainties(up). (Right) TnP scaling factor uncertainties(down).

331 In fact, there is no significant centrality dependence on the B^+ tag and probe scale factors. We
 332 can take the ratio of 0 - 30% and 30% - 90% to the inclusive 0 - 90%. Figure 28 shows the 2D
 333 map ratios:

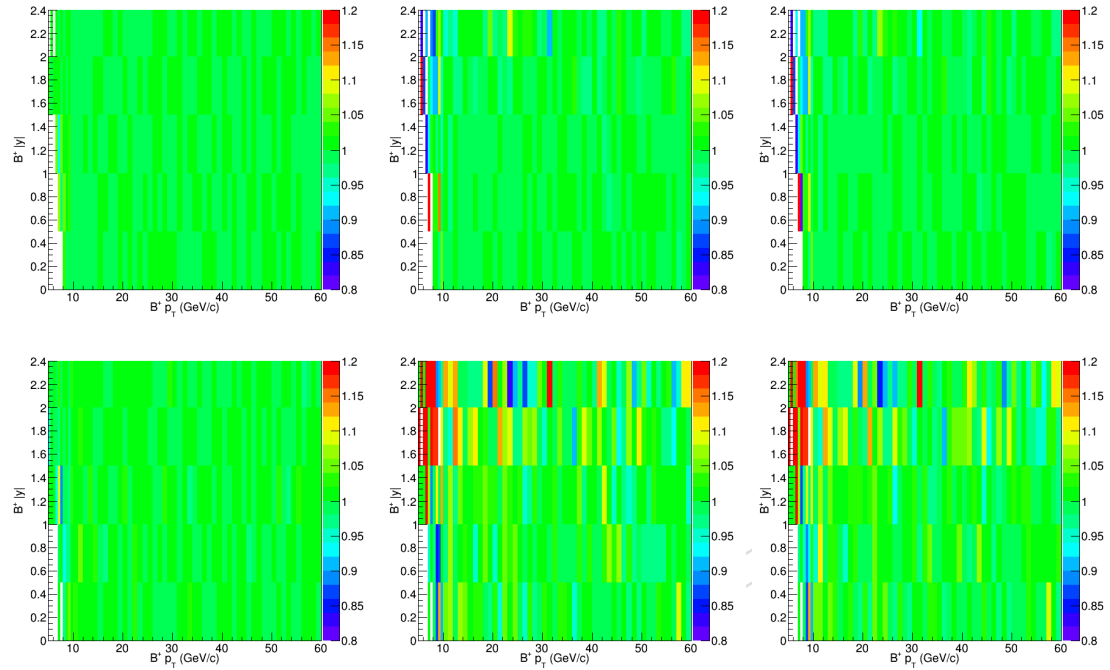


Figure 28: The finely binned 2D tag and probe scaling factor ratio to the inclusive 0 - 90% vs B^*
 p_T and $B^* |y|$ and their upper and lower uncertainties are for 0 - 30% (up) and 30% - 90% (down)
 are shown respectfully above.

334 Again, we have explicitly shown that their ratio is consistent with unity within uncertainties
 335 and thus no significant centrality is observed for the tag and probe scale factors.

336 7.2 Acceptance and Efficiency from PbPb MC

337 We adopted the same method with B_s^0 to calculate the efficiency correction factor. Basic concept
 338 is, rather than using the functional form of $B^+ p_T$ weight (which is essentially the same with
 339 what we want to measure - p_T shape), we calculate acceptance and efficiency from MC in a
 340 finely binned map of rapidity and transverse momentum. After then, we loop over data can-
 341 didates that passed the full selection and the signal region confinement identical to the TMVA
 342 training and give them $\langle \frac{1}{\alpha \times \epsilon} \rangle$ factors. We take the average of these factors in the analysis p_T bin
 343 we want to examine. In other words, we do coarser version of event-by-event weighting in a
 344 finite-binned map.

345 However, since we don't explicitly discriminate signal and background in this procedure. Thus
 346 potential difference in signal and background in the signal region, where the invariant is within
 347 $0.08 \text{ GeV}/c^2$ near the B^+ PDG mass peak, may entail discrepancy in the calculation. This effect
 348 can be examined by Splot weight method which will be described further in detail if needed.

349 Fig. 29 shows the 2D map of acceptance*efficiency in the fiducial region. Fig. 30 shows the
 350 data-average of $\langle \frac{1}{\alpha \times \epsilon} \rangle$ factor in p_T binnings in centrality 0 - 90%. Fig. 31 shows the correction
 351 factor of inclusive p_T 10 - 50 GeV/c for centrality 0 - 30%, 30% - 90%, and 0 - 90%

352

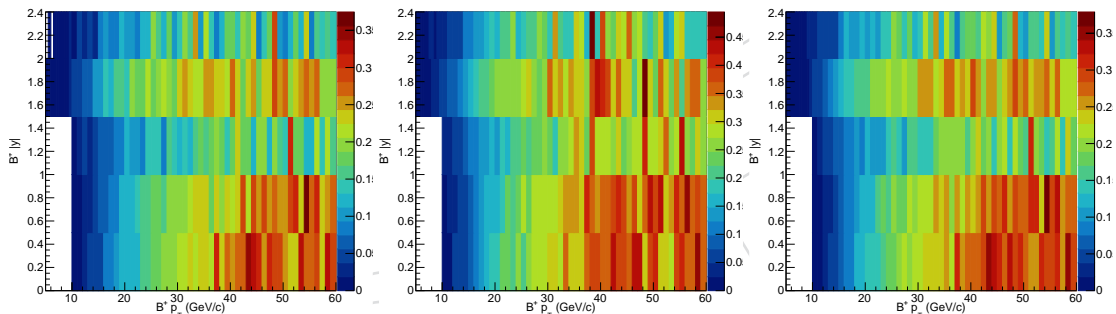


Figure 29: B^+ acceptance*efficiency in 2D map. (Left) Centrality 0-30% (Middle) 30-90% (Right) 0-90%

353 The precise central values and uncertainties of the $\langle \frac{1}{\alpha \times \epsilon} \rangle$ are also summarized in Table 3 below

Table 3: The precise central values and uncertainties of the efficiency correction factors $\langle \frac{1}{\alpha \times \epsilon} \rangle$ are summarized below.

Centrality	p_T (GeV/c)	$\langle \frac{1}{\alpha \times \epsilon} \rangle$ Central Value	$\langle \frac{1}{\alpha \times \epsilon} \rangle$ Propagated Error
0 - 90%	7 - 10	107.8	5.2
0 - 90%	10 - 15	32.5	0.3
0 - 90%	15 - 20	10.11	0.059
0 - 90%	20 - 50	5.71	0.04
0 - 30%	10 - 50	19.02	0.21
30 - 90%	10 - 50	10.72	0.11
0 - 90%	10 - 50	17.02	0.12

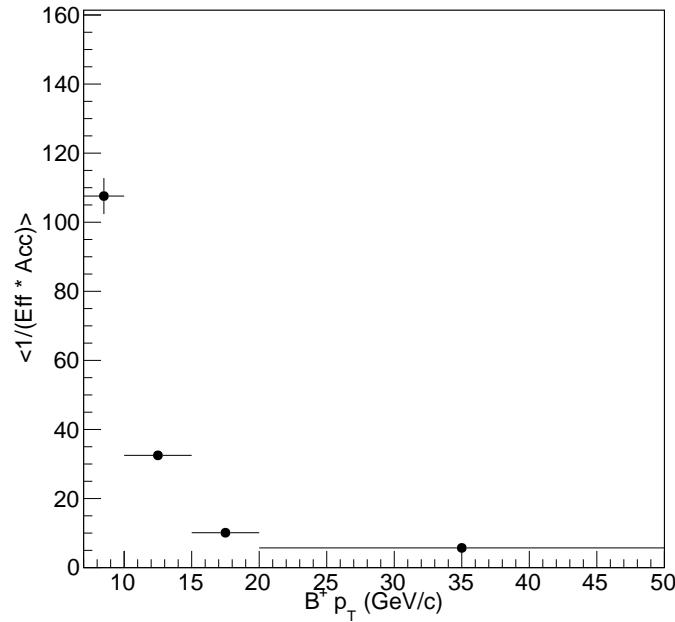


Figure 30: Data candidate average of the efficiency correction factor of B^+ vs p_T using B_s binning are shown above.

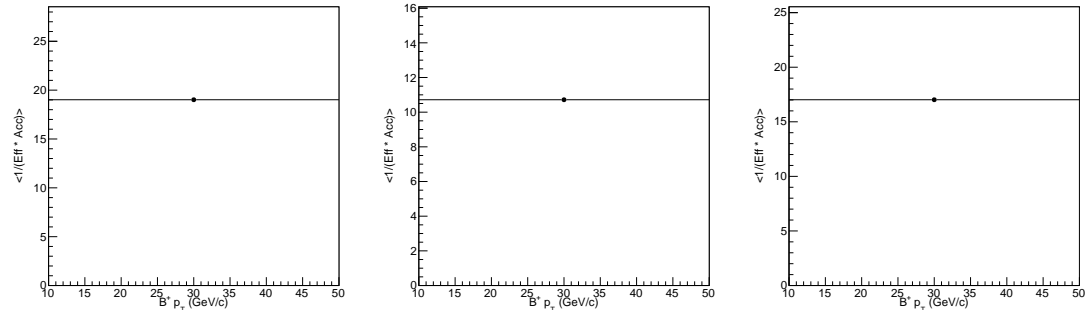


Figure 31: Data candidate average of the efficiency correction factor of B^+ in inclusive p_T . 10 - 50 GeV/c for 0 - 30%, 30% - 90%, and 0 - 90%.

354 7.3 sPlot Weight Techniques Studies

355 Again, to understand the effects of the possible contamination in the signal region on the ef-
 356 ficiency factor $\langle \frac{1}{\alpha \times \epsilon} \rangle_i$, we apply sPlot techniques [9] to separate the signal and background in
 357 the data. We assign a weight to each candidates and recompute the weighted average $\langle \frac{1}{\alpha \times \epsilon} \rangle$
 358 defined as follows:

$$\langle \frac{1}{\alpha \times \epsilon} \rangle_i = \frac{\sum_j^{n_i} w_j \frac{1}{\alpha \times \epsilon_j}}{\sum_j^{n_i} w_j} \quad (1)$$

359 The fits on the inclusive 5 - 50 GeV/c B^+ invariant mass distribution and the pull distribution
 360 are shown below

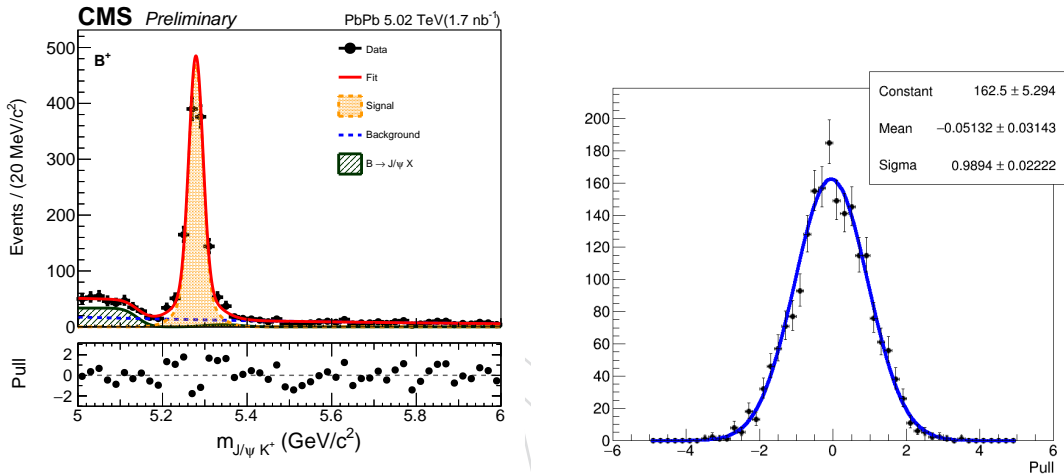


Figure 32: The 5 - 50 GeV/c B^+ invariant mass distribution and the raw yield fits are shown on the left. The pull distribution from the invariant mass fits is shown on the right.

361 As we can see from Figure 32, we have a good closure on the fit on all B^+ candidates to obtain
 362 the sPlot. The sPlot weight distribution of the B^+ candidates in the data passing the analysis
 363 selection is shown below in Figure 33 . Note that the weight can be negative or greater than 1
 364 just as a normal sPlot weight applied in data-MC comparison studies.

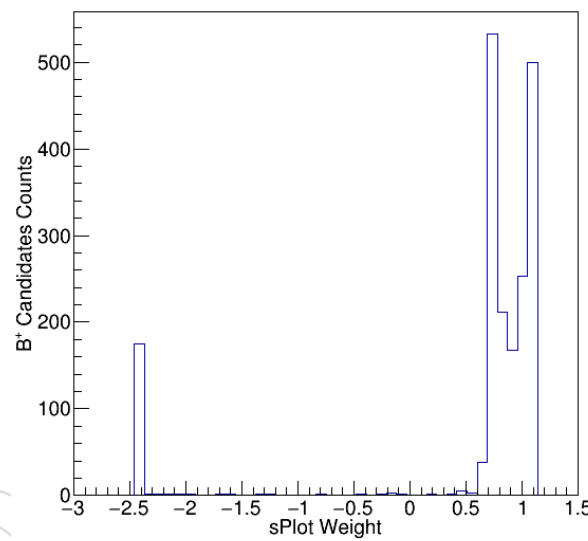


Figure 33: The sPlot weight distribution for B^+ candidates. They will be used to compute the sPlot weighted efficiency.

With the weights, we then recompute the efficiency correction factor $\langle \frac{1}{\alpha \times \epsilon} \rangle$ for each p_T and centrality bin. Our sPlot weighted results and the comparison with the nominal efficiency correction factor $\langle \frac{1}{\alpha \times \epsilon} \rangle$ for p_T and centrality bins are shown below in Figure 34 and Figure 35

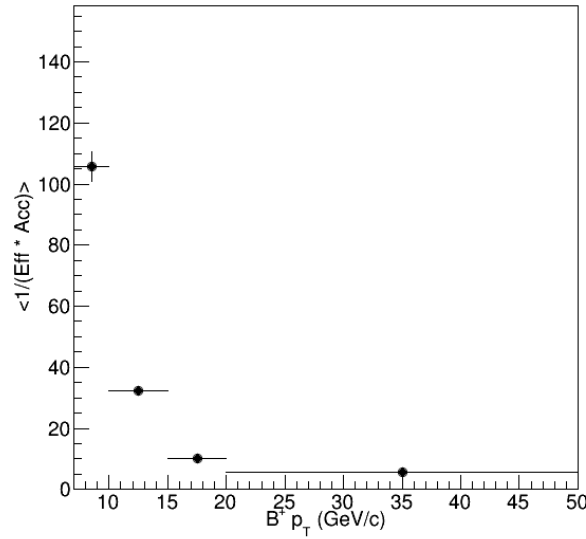


Figure 34: The p_T differential $\langle \frac{1}{\alpha \times \epsilon} \rangle$ for centrality 0 - 90% is shown above.

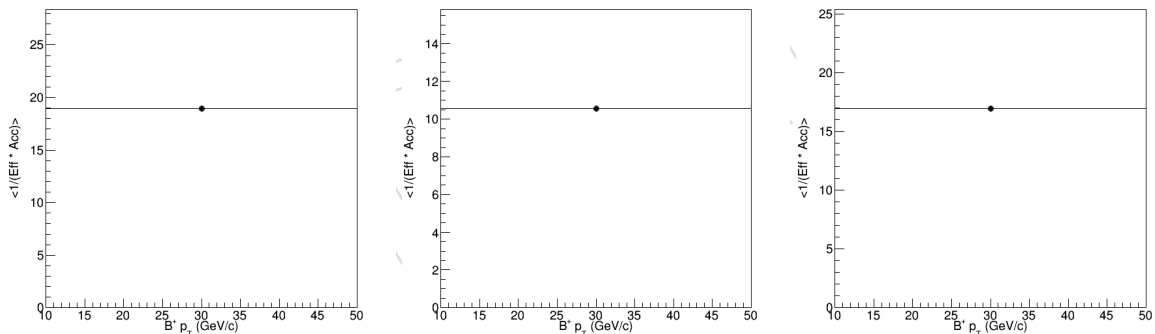


Figure 35: The p_T inclusive $\langle \frac{1}{\alpha \times \epsilon} \rangle$ for centrality 0 - 30% (left), 30% - 90% (middle), 0 - 90% (right) are shown above.

³⁶⁸ We compare numerically the value of $\langle \frac{1}{\alpha \times \epsilon} \rangle$ with and without sPlot weight. The results are
³⁶⁹ summarized below on Table 4

Table 4: The precise central values and uncertainties of the efficiency correction factors $\langle \frac{1}{\alpha \times \epsilon} \rangle$ are summarized below.

Centrality	p_T (GeV/c)	$\langle \frac{1}{\alpha \times \epsilon} \rangle$ Weighted	$\langle \frac{1}{\alpha \times \epsilon} \rangle$ Unweighted	Percent Deviation
0 - 90%	7 - 10	105.6	107.8	2.04%
0 - 90%	10 - 15	32.4	32.5	0.03%
0 - 90%	15 - 20	10.10	10.11	0.10%
0 - 90%	20 - 50	5.70	5.71	0.18%
0 - 30%	10 - 50	18.93	19.02	0.47%
30 - 90%	10 - 50	10.55	10.72	1.58%
0 - 90%	10 - 50	16.92	17.02	0.59%

³⁷⁰ As we can see, the sPlot weight effect is negligible and will not change our efficiency correction
³⁷¹ factor $\langle \frac{1}{\alpha \times \epsilon} \rangle$ significantly. They are well within 2%. Therefore, we will stick to use the nominal
³⁷² one without applying the sPlot weight as our nominal values in the final results.

DRAFT

373 8 Closure Test of the B^+ Corrected Yield

374 The closure test on B^+ is basically identical to the B_s case documented in section 8 of the AN-
 375 19-055 [1]. Therefore, here we will not discuss the detail procedures again about the studies in
 376 texts. Instead, we will just present the final results and summary of the statistical and system-
 377 atic uncertainties from the closure test in this section.

378 We first get the randomly sampled data-like size MC percentage deviation from the expected
 379 efficiency. Figure 36 shows the results from our studies.

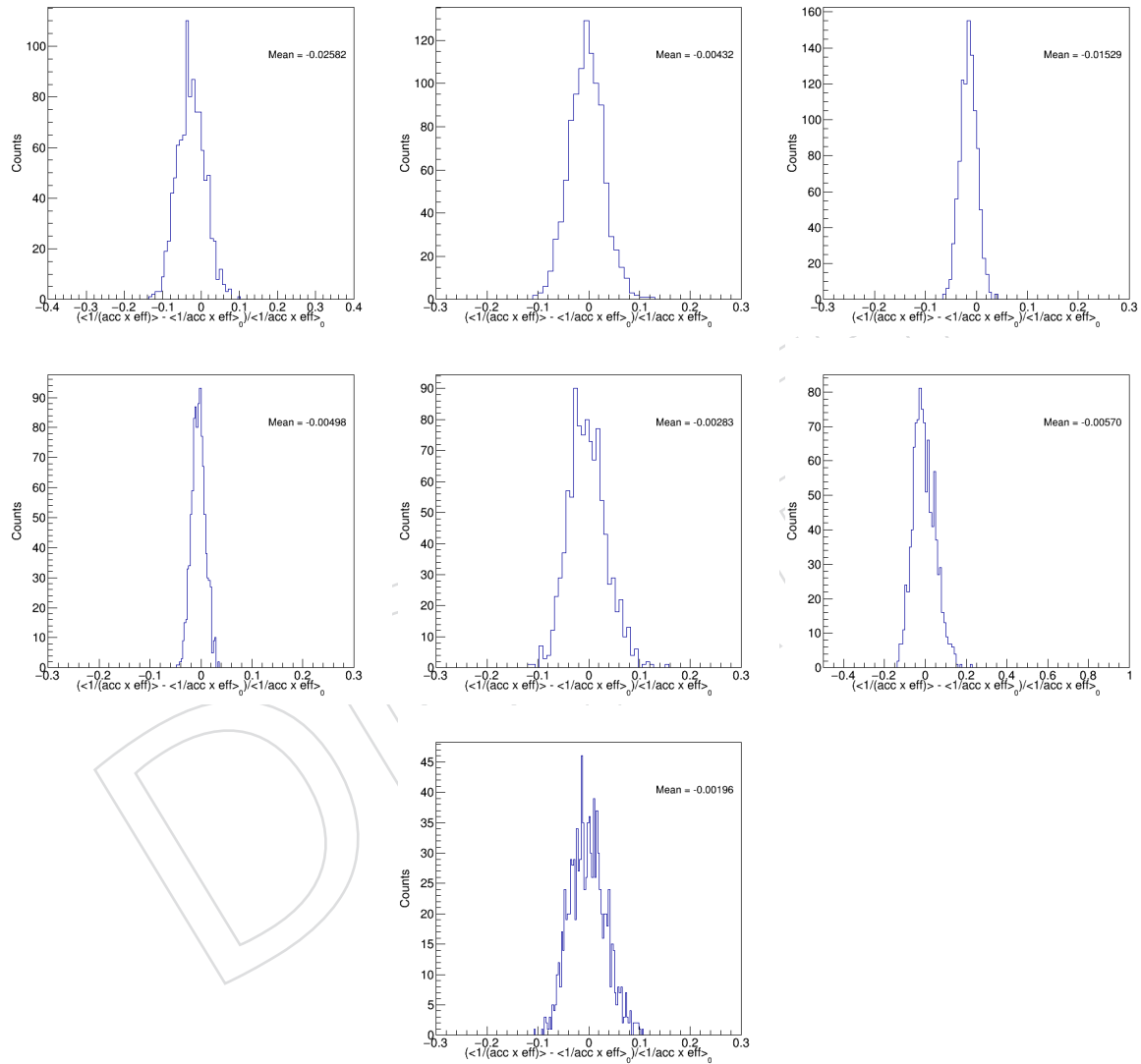


Figure 36: The percentage deviation distributions of $\langle \frac{1}{\alpha \times \epsilon} \rangle$ to RECO/GEN for the data-like randomly sampled MC samples for 0 - 90% at 7 - 10, 10 - 15, 15 - 20, and 20 - 50 GeV/c as well as 0 - 90%, 0 - 30%, and 30 - 90% are shown respectfully above.

³⁸⁰ Finally, we quote the mean value as the systematic due to the non-closure of $\langle \frac{1}{\alpha \times \epsilon} \rangle$. The per-
³⁸¹ centage deviation is summarize in the table 5

Table 5: The percentage deviation of the efficiency factors from the expected value in the statistics similar to the data analysis are shown above.

Centrality	p_T (GeV/c)	% Dev
0 - 90%	7 - 10	-2.58%
0 - 90%	10 - 15	-0.43%
0 - 90%	15 - 20	-1.53%
0 - 90%	20 - 50	-0.50%
0 - 90%	10 - 50	-0.28%
0 - 30%	10 - 50	-0.57%
30 - 90%	10 - 50	-0.20%

DRAFT

³⁸² In conclusion, we can see that, even in the limit of low statistics, which is similar to the statistics
³⁸³ in our data analysis, the $\langle \frac{1}{\alpha \times \epsilon} \rangle$ correction method still gives us satisfying closure with bias
³⁸⁴ within 3%.

³⁸⁵ Next, we validate that our fits to extract the raw yield actually have good closure. The raw
³⁸⁶ yield distributions are shown below for p_T bins in Figure 37 and centrality bins Figure 38. We
³⁸⁷ also summarize on Table 6

DRAFT

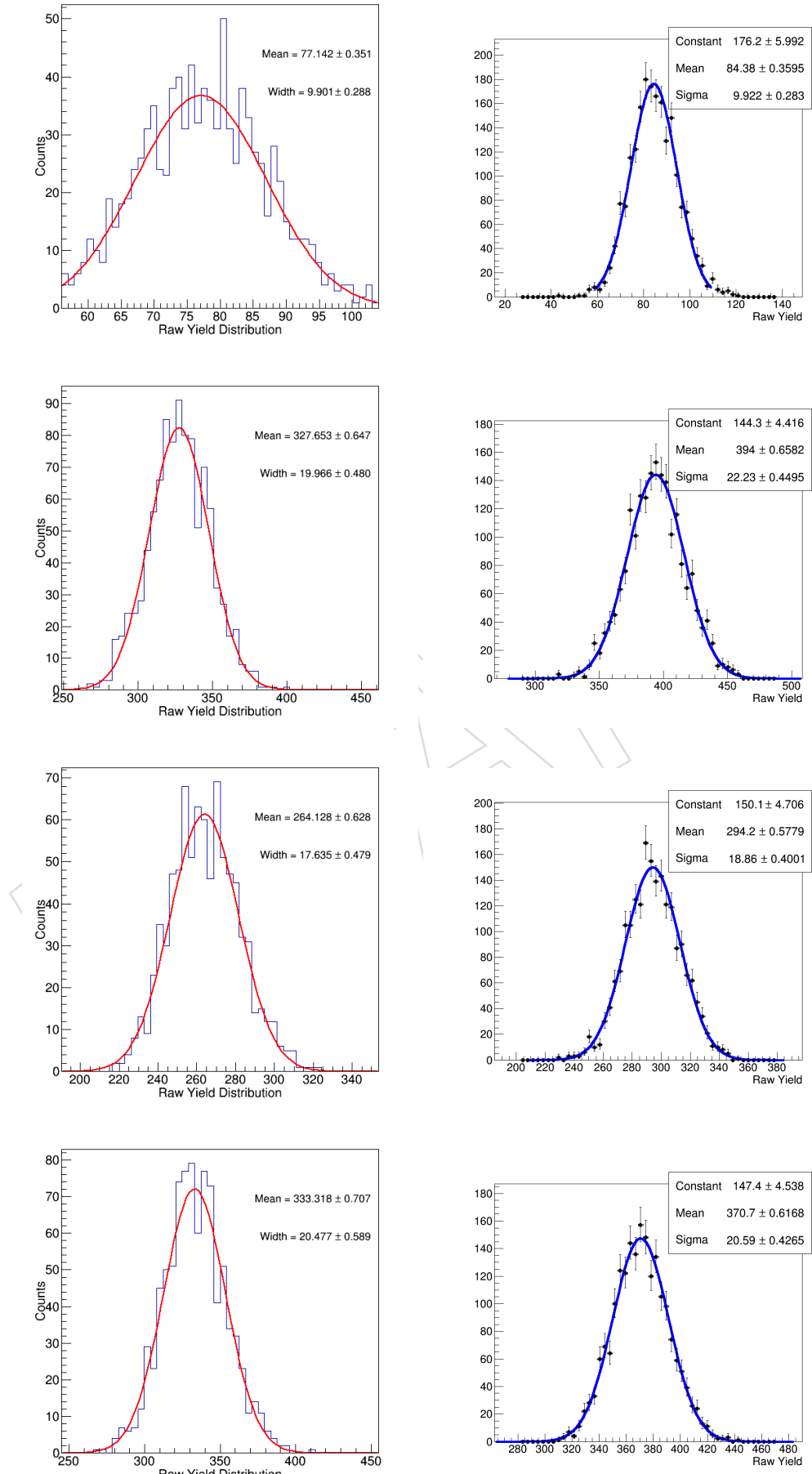


Figure 37: The raw yield distributions from resampled datasets (left) and toy MC (right) for 0 - 90% at 7 - 10, 10 - 15, 15 - 20, 20 - 50 are shown respectfully above.

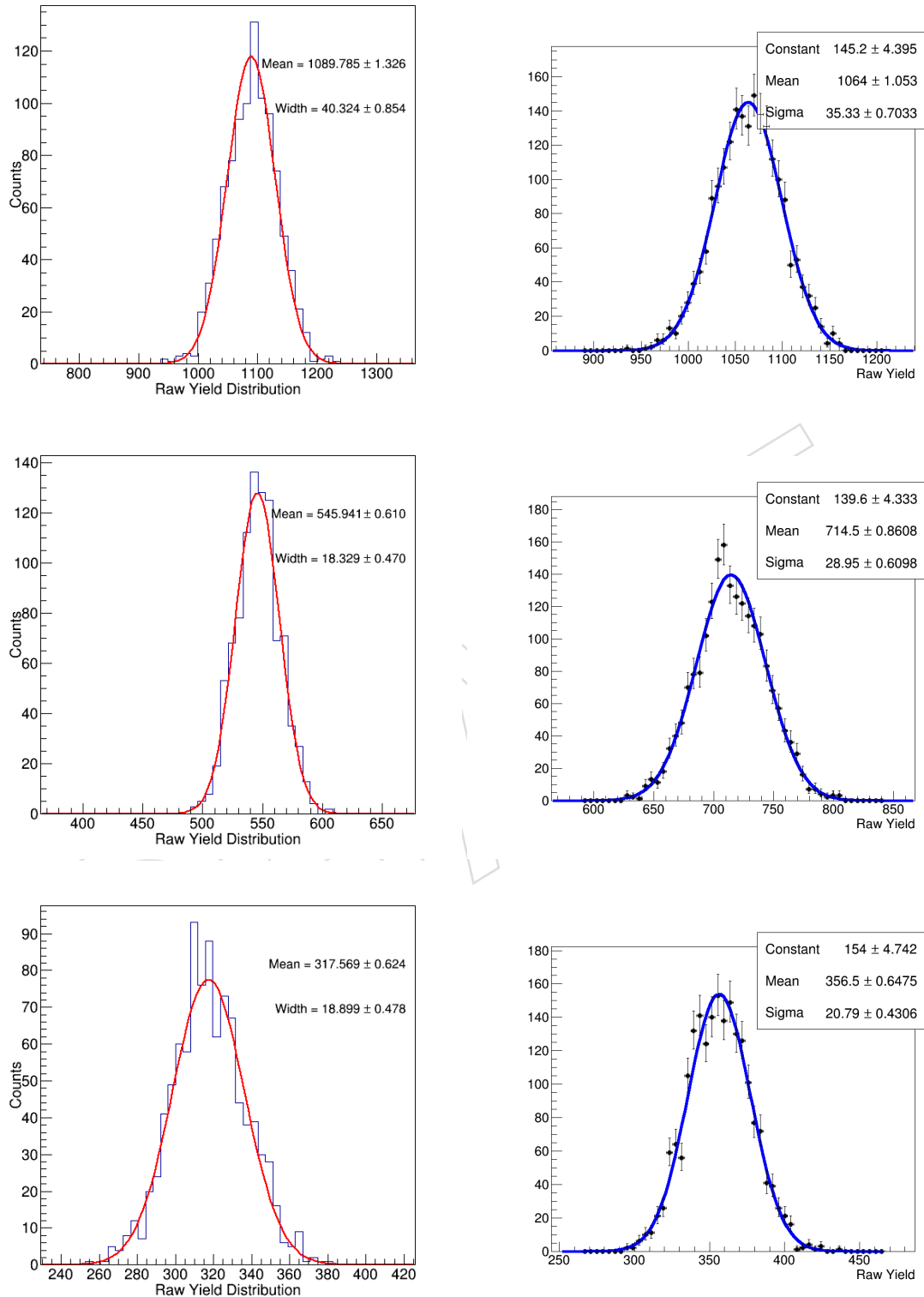


Figure 38: The raw yield distributions from resampled datasets (left) and toy MC (right) for 10 - 50 GeV/c for 0 - 30%, 30% - 90%, and 0 - 90% are shown respectfully above.

Table 6: The RMS/Mean of the corrected yield distribution are summarized above.

Centrality	p_T (GeV/c)	Data Resampling Raw Yield	Toy MC Raw Yield
0 - 90%	7 - 10	77 ± 9.9	84.4 ± 9.9
0 - 90%	10 - 15	327 ± 20	394 ± 22
0 - 90%	15 - 20	264 ± 18	294 ± 19
0 - 90%	20 - 50	333 ± 20	371 ± 21
0 - 90%	10 - 50	1090 ± 40	1064 ± 35
0 - 30%	10 - 50	546 ± 18	715 ± 29
30 - 90%	10 - 50	318 ± 19	357 ± 21

DRAFT

388 Subsequently, we are able to get the efficiency correction factor $\langle \frac{1}{\alpha \times \epsilon} \rangle$ in Figure 39

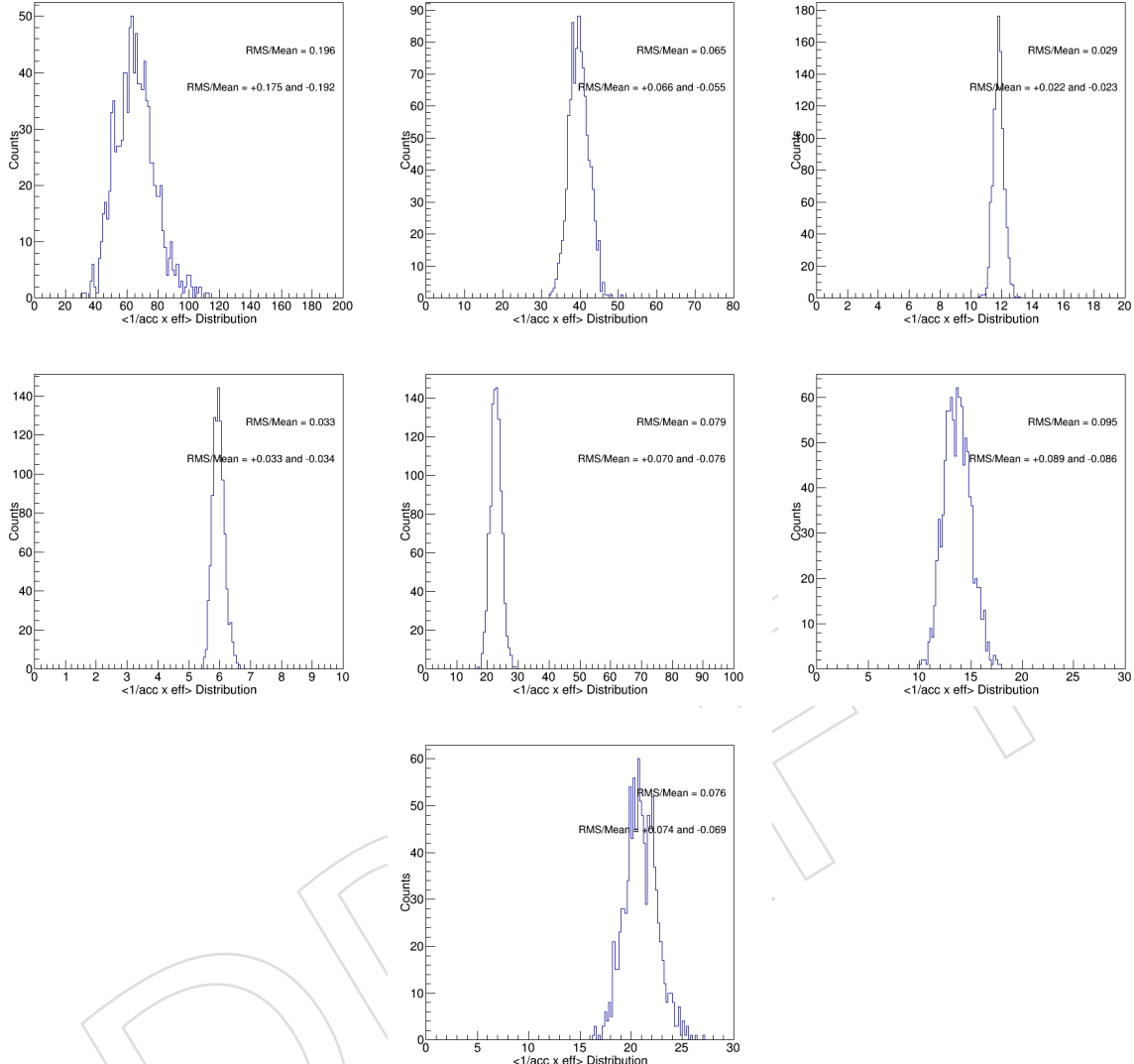


Figure 39: The efficiency correction factor $\langle \frac{1}{\alpha \times \epsilon} \rangle$ distributions of the data-like randomly resampled datasets for 0 - 90% at 7 - 10, 10 - 15, 15 - 20, and 20 - 50 GeV/c as well as 0 - 30%, 30 - 90%, and 0 - 90% are shown respectfully above.

Table 7: The RMS/Mean and the asymmetric up and down statistical uncertainties of the efficiency correction factor $\langle \frac{1}{\alpha \times \epsilon} \rangle$ distribution are summarized below.

Centrality	p_T (GeV/c)	RMS/Mean	Stat. Up (+)	Stat Down (-)
0 - 90%	7 - 10	19.6%	17.5%	19.2%
0 - 90%	10 - 15	6.5%	6.6%	5.5%
0 - 90%	15 - 20	2.9%	2.2%	2.3%
0 - 90%	20 - 50	3.3%	3.3%	3.4%
0 - 30%	10 - 50	7.9%	7.0%	7.6%
30 - 90%	10 - 50	9.5%	8.9%	8.6%
0 - 90%	10 - 50	7.6%	7.4%	6.9%

389 Then, our corrected yield distributions are shown in 40 below

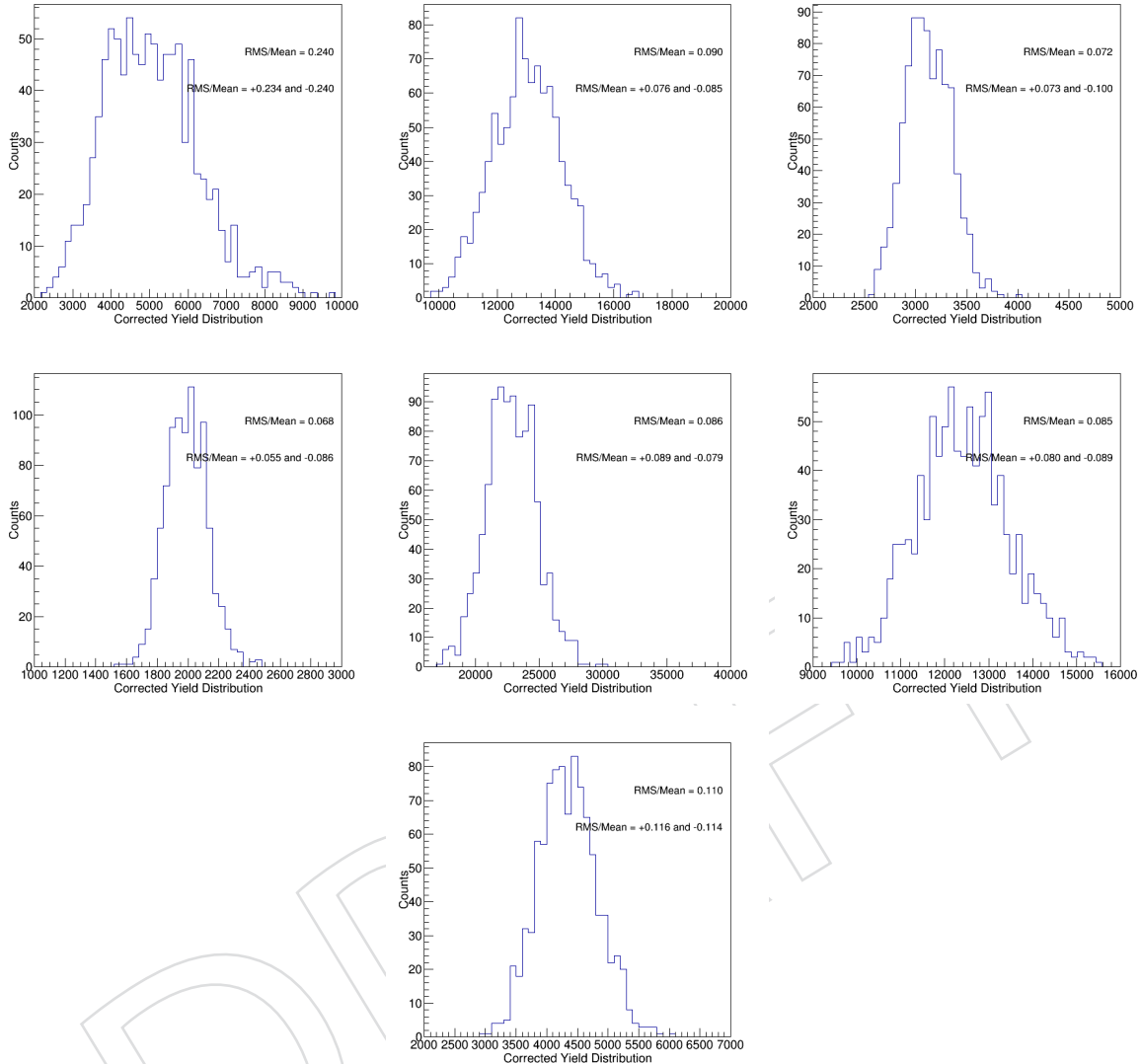


Figure 40: The corrected yield distributions of the data-like randomly resampled datasets for 0 - 90% at 7 - 10, 10 - 15, 15 - 20, and 20 - 50 GeV/c as well as 0 - 90%, 0 - 30%, and 30 - 90% are shown respectfully above.

390 Finally, we calculate the RMS/Mean and the asymmetric up and down statistical uncertainties
 391 of the corrected yield distribution above for each p_T and centrality and quote them as our
 392 statistical uncertainties. The procedure of calculating the asymmetric up and down statistical
 393 uncertainties is described in the B_s AN [1]. Our results are summarized on the table 8 below:

394 Here, we conclude our closure test. We will quote the results from Tab. 8 as the statistical
 395 uncertainties of our corrected yield and 5 as the systematic uncertainties due to the bias of
 396 efficiency correction for our data analysis. We have included them in our final B^+ results. We
 397 finally attach the summary of comparison among the raw yield, efficiency correction factor,
 398 and corrected yield in Table 9 below

Table 8: The RMS/Mean and the asymmetric up and down statistical uncertainties of the corrected yield distribution are summarized below.

Centrality	p_T (GeV/c)	RMS/Mean	Stat. Up (+)	Stat Down (-)
0 - 90%	7 - 10	24.0%	23.4%	24.0%
0 - 90%	10 - 15	9.0%	7.6%	8.5%
0 - 90%	15 - 20	6.6%	7.3%	10.0%
0 - 90%	20 - 50	6.8%	5.5%	8.6%
0 - 90%	10 - 50	8.6%	8.9%	7.9%
0 - 30%	10 - 50	8.5%	8.0%	8.9%
30 - 90%	10 - 50	11.0%	11.6%	11.4%

Table 9: The statistical uncertainties on the B^+ raw yield, efficiency correction factor $\langle \frac{1}{\alpha \times \epsilon} \rangle$, and corrected yield distribution are summarized below for comparison.

Centrality	p_T (GeV/c)	Raw Yield	$\langle \frac{1}{\alpha \times \epsilon} \rangle$ Err (+)	$\langle \frac{1}{\alpha \times \epsilon} \rangle$ Err (-)	Corr. Err (+)	Corr. Yield Err (-)
0 - 90%	7 - 10	11.7%	17.5%	23.4%	19.2%	24.0%
0 - 90%	10 - 15	5.6%	6.6%	7.6%	5.5%	8.5%
0 - 90%	15 - 20	6.5%	2.2%	7.3%	2.3%	10.0%
0 - 90%	20 - 50	5.4%	3.3%	5.5%	3.4%	8.6%
0 - 30%	10 - 50	4.1%	7.0%	8.0%	7.6%	8.9%
30 - 90%	10 - 50	14.3%	8.9%	11.6%	8.6%	11.4%
0 - 90%	10 - 50	5.9%	7.4%	8.9%	6.9%	7.9%

399 9 Results

400 9.1 p_T differential corrected yield in PbPb collisions at 5.02 TeV

401 The method we applied is the same with B_s AN [1].

402 In Fig. 41, Number of MinBias events-normalized, TAA-normalized, efficiency-corrected and
 403 p_T -width divided yield (let's call this "normalized corrected yield") of B^+ mesons in the cen-
 404 trality 0-90% and rapidity region $|y_{\text{lab}}| < 2.4$ (Caveat: Note the fiducial region $1.5 < |y_{\text{lab}}| < 2.4$
 405 in B^+ p_T 7 - 10GeV/c) in PbPb collisions at $\sqrt{s} = 5.02$ TeV is presented. The boxes around the
 406 data points represent the total systematic uncertainties.

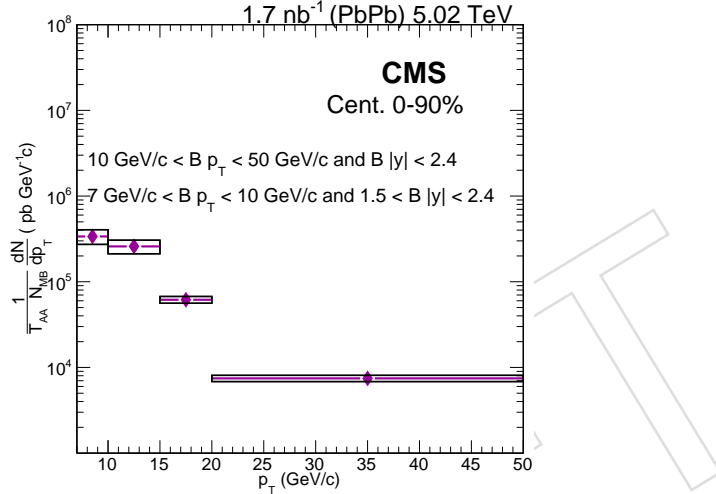


Figure 41: B^+ normalized corrected yield vs. p_T in the inclusive centrality range 0-90%. (Left) B^+ analysis p_T bin (Right) B_s^0 analysis p_T bin. Note the fiducial region p_T 5-10GeV and $1.5 < |y_{\text{lab}}| < 2.4$

407 In addition, we provide the normalized corrected yield for inclusive p_T 10-50 GeV/c in 0 - 30%,
 408 30 - 90%, and 0 - 90% centrality bins in Fig. 42.

409 The normalized corrected yields and their uncertainties for various kinematic ranges are sum-
 410 marized in Table. 10 and Table. 11. For more details on systematic uncertainties, see Section. 10.

411

Table 10: B^+ normalized corrected yields and the uncertainties in various p_T ranges within centrality 0-90%. All the corrected yield values are in units of pb^{-1}GeV . Note that the global uncertainties are not included here on this table, which are sub 4% level. Note also the fiducial region p_T 5-10GeV and $1.5 < |y_{\text{lab}}| < 2.4$ and the same as the B_s p_T binning is reported.

p_T (GeV)	Corrected yield	Stat. up (+)	Stat. down (-)	Syst. up (+)	Syst. down (-)
7-10	359765	23.4%	24.0%	19.6%	18.8%
10-15	275298	7.58%	8.54%	18.1%	17.9%
15-20	65653	7.30%	10.0%	9.22%	9.00%
20-50	7940	5.50%	8.56%	8.41%	8.24%

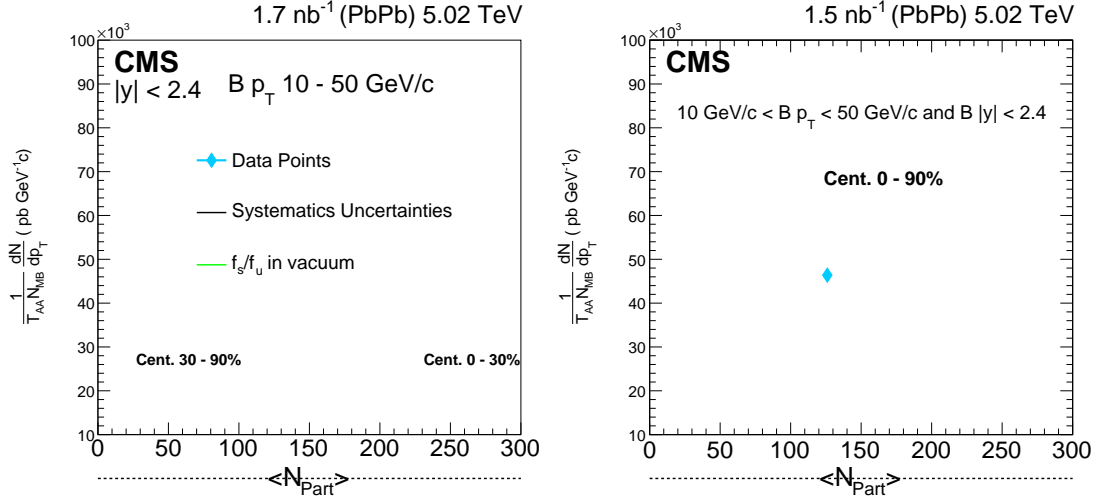


Figure 42: B^+ normalized corrected yield vs. $\langle N_{\text{part}} \rangle$ in inclusive p_T . (Left) 10-50GeV, 0-30-90% 30-90% and (Right) 10-50GeV, 0-90%. Note the fiducial region p_T 5-10GeV and $1.5 < |y_{\text{lab}}| < 2.4$

Table 11: B^+ normalized corrected yield and the uncertainties of inclusive p_T 10 - 50GeV for 0 - 30% and 30 - 90%, and 00-90%. All the corrected yield values are in units of pb^*c/GeV . Note that the global uncertainties are not included here on this table, which are sub 3% level. Note also the fiducial region p_T 5-10GeV and $1.5 < |y_{\text{lab}}| < 2.4$

Centrality	Corrected yield	Stat. up (+)	Stat. down (-)	Syst. up (+)	Syst. down (-)
0-30%	14969	8.03%	8.89%	12.7%	12.4%
30-90%	38518	11.6%	11.4%	13.3%	13.0%
0-90%	49403	8.85%	7.95%	13.1%	12.9%

⁴¹² **10 Systematic uncertainties**

⁴¹³ **10.1 Summary table**

⁴¹⁴ Below are the summary tables of various systematic uncertainties. For detailed description of
⁴¹⁵ each systematics source, please refer to the subsequent subsections.

Table 12: Summary of systematic uncertainties from each factor in B^+ PbPb analysis for corrected yield vs p_T . All the values are shown in percentage.

Factors	(7,10)	(10,15)	(15,20)	(20,50)
Hadron tracking efficiency	5%	5%	5%	5%
Data-MC Discrepancy	5.67%	15.30%	3.61%	1.74%
p_T shape	0.128%	0.206%	0.000%	0.010%
PDF variation background	4.46%	2.67%	2.74%	2.36%
PDF variation signal	0.117%	0.546%	0.576%	1.03%
TnP Systematics +)	9.72%	6.96%	5.88%	5.85%
TnP Systematics -)	8.28%	6.48%	5.52%	5.60%
MC stat.	14.86%	3.75%	2.20%	1.51%
Total +)	19.80%	18.14%	9.23%	8.44%
Total -)	19.14%	17.96%	9.01%	8.28%
N_{MB+}) events	1.18%	1.18%	1.18%	1.18%
N_{MB-}) events	1.18%	1.18%	1.18%	1.18%
T_{AA}	2.2%	2.2%	2.2%	2.2%
Branching fractions	2.8%	2.8%	2.8%	2.8%
Global Systematics +)	3.75%	3.75%	3.75%	3.75%
Global Systematics -)	3.75%	3.75%	3.75%	3.75%

⁴¹⁶ We also plot the summary plots for the table able as follows in Fig 43

Table 13: Summary of systematic uncertainties from each factor in B^+ PbPb analysis for corrected yield vs centrality. All the values are shown in percentage.

Factors	0 - 30 %	30 % - 90%	0 - 90 %
Hadron tracking efficiency	5%	5%	5%
Data-MC Discrepancy	12.86%	7.92 %	10.50%
p_T shape	0.131%	0.163%	0.139%
PDF variation background	0.412%	1.13%	0.427%
PDF variation signal	2.50%	2.57%	2.60%
TnP Systematics +)	6.68%	6.59%	6.65%
TnP Systematics -)	6.31%	6.18%	6.22%
MC stat.	3.15%	2.24%	2.28%
T_{AA}	2.0%	3.6%	2.2%
N_{MB} events +)	1.32%	1.22%	1.18%
N_{MB} events -)	1.34%	1.21%	1.18%
Total +)	16.04%	12.59%	14.07%
Total -)	15.89%	12.38%	13.87%
Branching fractions	2.8%	2.8%	2.8%
Global Systematics +)	2.8%	2.8%	2.8%
Global Systematics -)	2.8%	2.8%	2.8%

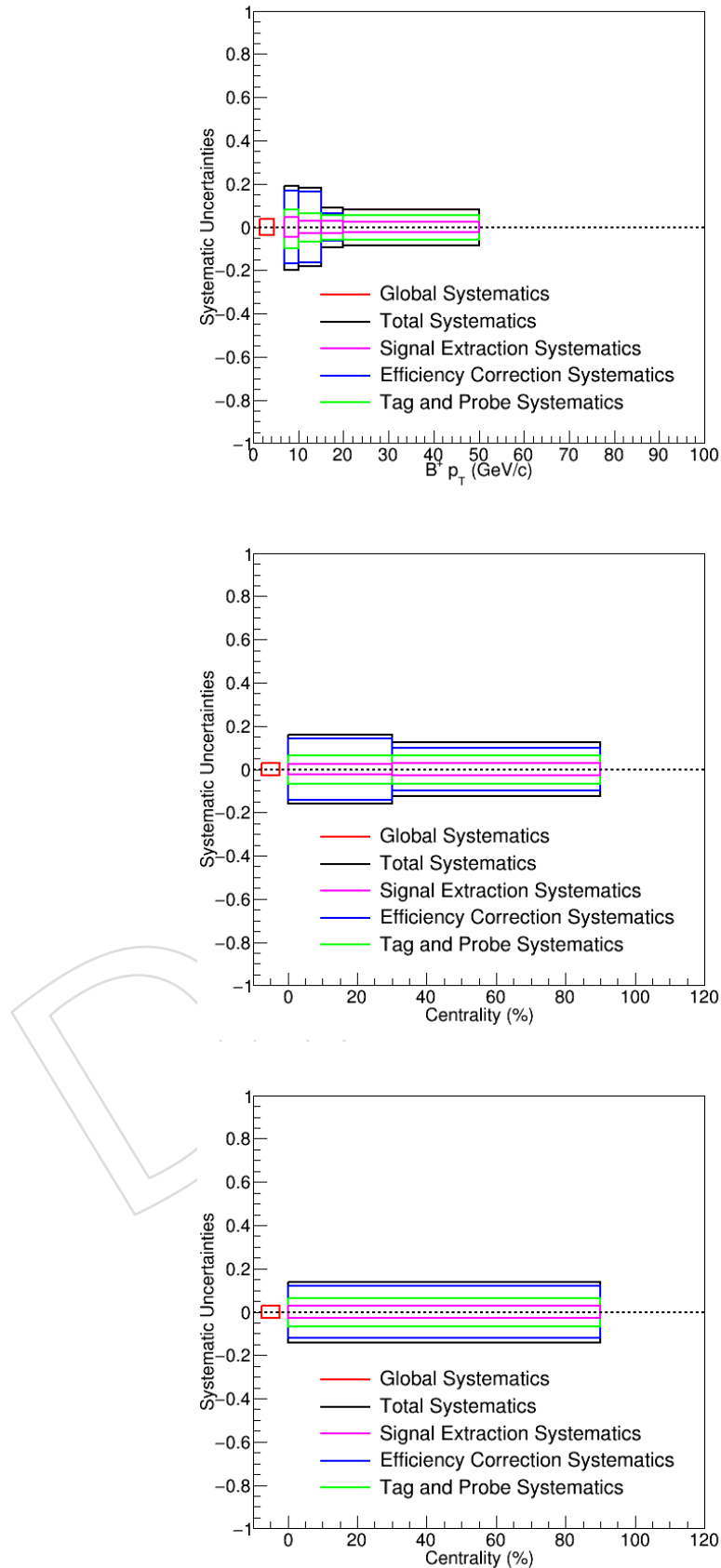


Figure 43: The plots summarizing the systematic uncertainties for p_T bins and centrality bins are shown above.

417 **10.2 T_{AA} and N_{MB}**

418 We use the same uncertainties for T_{AA} (Nuclear overlap function) and N_{MB} (Number of Min-
419 Bias events) listed on the B_s AN [1].

420 **10.3 Branching ratio**

421 The systematic uncertainty on the branching ratio of the decay $B^+ \rightarrow J/\psi K^+$, with $J/\psi \rightarrow$
422 $\mu^+ \mu^-$, is calculated by adding in quadrature the uncertainties on each sub-channel. The re-
423 sulting uncertainty for the full decay chain is 2.8% [7]. This is global to all p_T and centrality
424 selections in our analysis.

425 **10.4 Tracking efficiency**

426 The current standard value of tracking efficiency uncertainty for one track is 5% for now, sug-
427 gested in the link <https://twiki.cern.ch/twiki/bin/viewauth/CMS/HITracking2018PbPb>.
428 This is global to all p_T and centrality selections in our analysis. This number may be updated
429 later.

430 **10.5 Muon efficiency: Tag and Probe**

431 The TnP study on 2D map is done and the plots are shown in Sec. 7. The uncertainties are
432 propagated onto the $\langle \frac{1}{\alpha \times \epsilon} \rangle$ data-average method. The data-average $\langle \frac{1}{\alpha \times \epsilon} \rangle$ with TnP scaling
433 factors are our nominal values, and the data-average with TnP scaling and uncertainty factors
434 are our deviated values for systematics estimation.

435 Basically, we have taken into account the muon identification (denoted: muid), tracking (de-
436 noted: trk), and triggering (denoted: trg). To calculate the scale factor, we apply the B meson
437 optimal selection with the , PVz, and centrality reweighting implemented on the B meson can-
438 didates. We have the nominal as well as the up and down with 1 sigma of the combined
439 statistics and systematics value for each of the 3 scale factor according to the dilepton header
440 file. Then, we individually apply these correction on the $\langle \frac{1}{\alpha \times \epsilon} \rangle$ for p_T (Figure 44) and centrality
441 (Figure 45) are shown below:

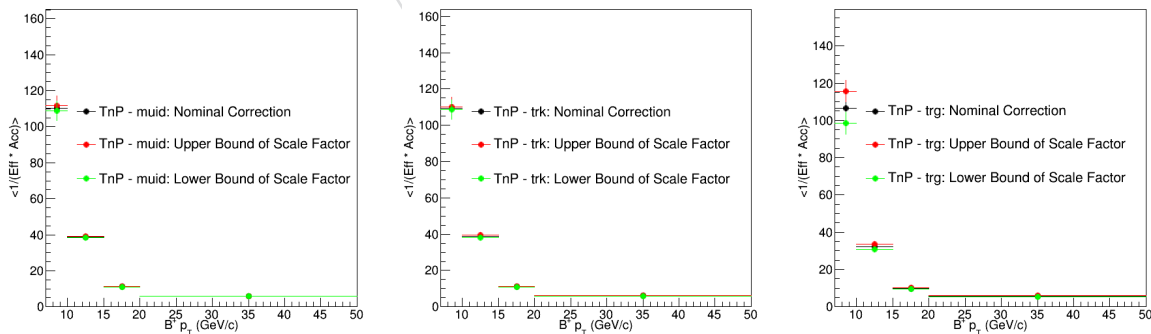


Figure 44: The $\langle \frac{1}{\alpha \times \epsilon} \rangle$ vs p_T with muon identification correction only (left), muon tracking only (middle), and muon trigger only (right) are shown above.

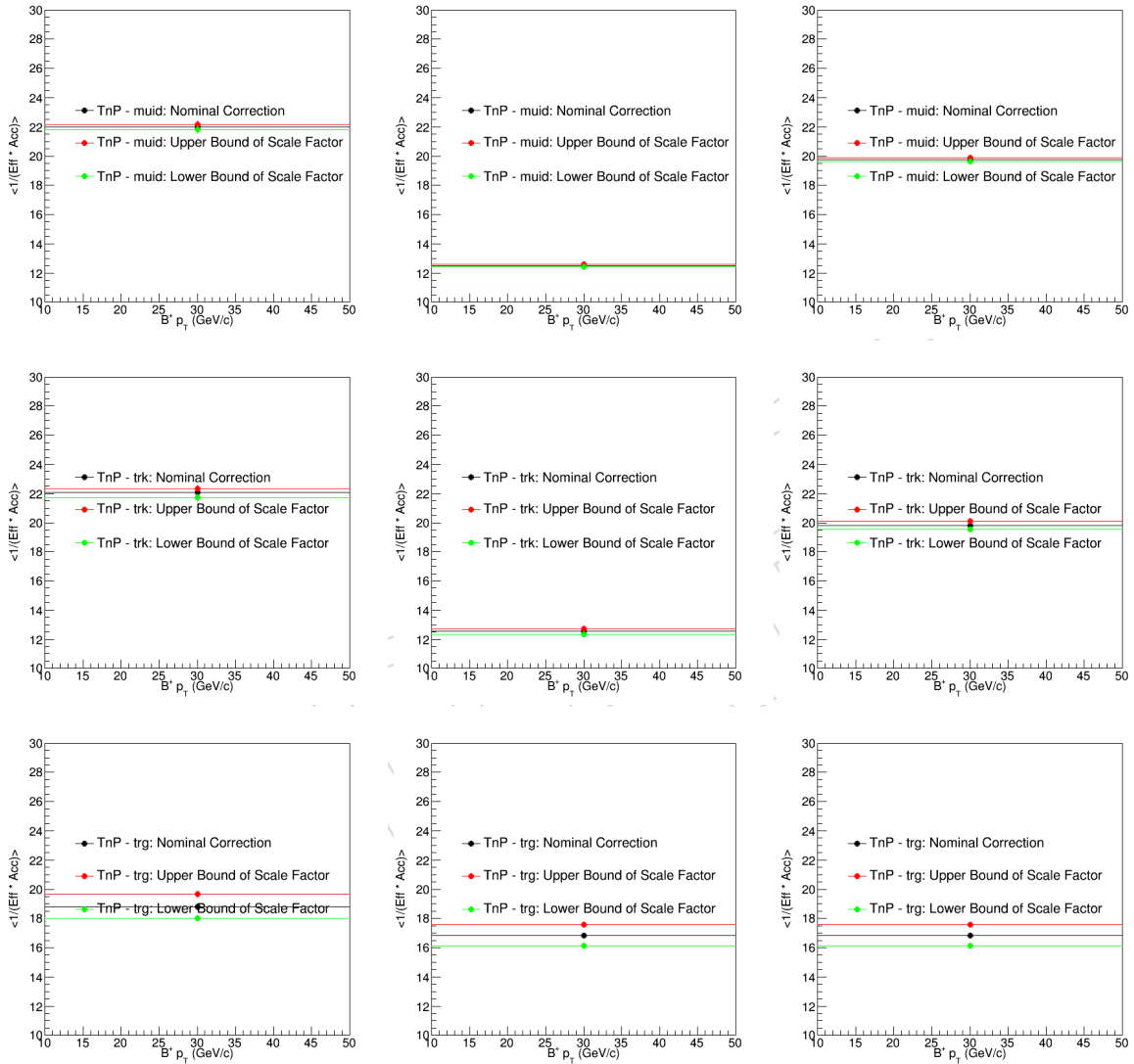


Figure 45: The $\langle \frac{1}{\alpha \times \epsilon} \rangle$ vs centrality in 0 - 30% (top), 30% - 90% (middle), 0 - 90% (bottom) with muon identification correction only (left), muon tracking only (middle), and muon trigger only (right) are shown above.

442 Then, the total nominal scale factor (central value) used in the analysis is given by the product
 443 of the 3 corrections: $\text{total} = \text{muid} \times \text{trk} \times \text{trg}$. The total scaling factor up and down uncertain-
 444 ties are added by their total up and down into quadrature: $\frac{\sigma_{\text{total}}}{\text{total}} = \sqrt{(\frac{\sigma_{\text{muid}}}{\text{muid}})^2 + (\frac{\sigma_{\text{trk}}}{\text{trk}})^2 + (\frac{\sigma_{\text{trg}}}{\text{trg}})^2}$.
 445 Our results for p_T and centrality are shown on Figure 46 and Figure 47 below

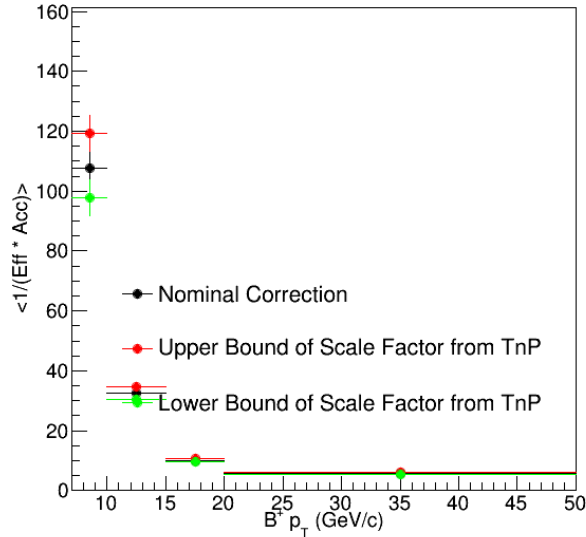


Figure 46: The $\langle \frac{1}{\alpha \times \epsilon} \rangle$ vs p_T with total tag and probe correction is shown above.

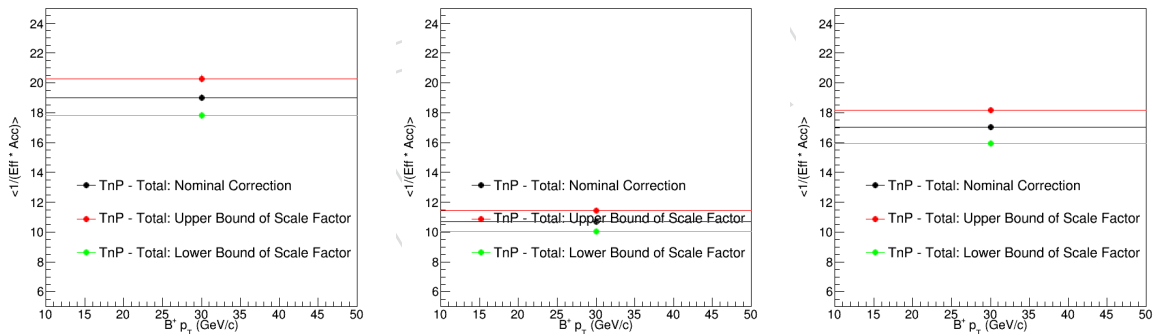


Figure 47: The $\langle \frac{1}{\alpha \times \epsilon} \rangle$ vs centrality in 0 - 30% (top), 30% - 90% (middle), 0 - 90% (bottom) with total tag and probe correction is shown above.

⁴⁴⁶ The difference between the nominal and varied values are quoted as our systematics, and they
⁴⁴⁷ are shown in Figure 48 and Figure 49 and Table. 12 and Table. 13.

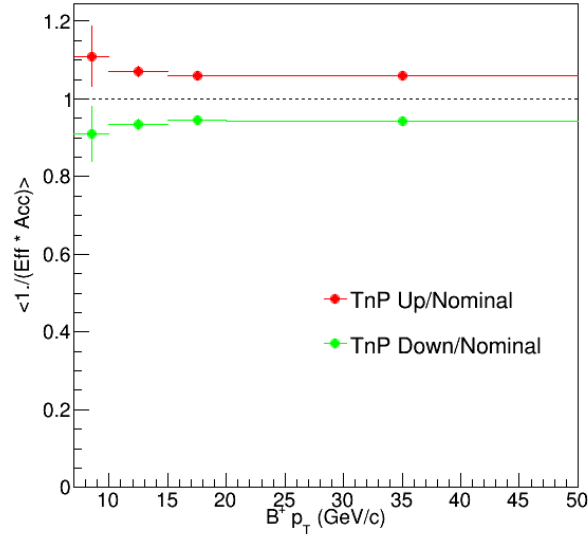


Figure 48: The upper bound and lower bound systematic uncertainties in $\langle \frac{1}{\alpha \times e} \rangle$ vs p_T with total tag and probe correction are shown above.

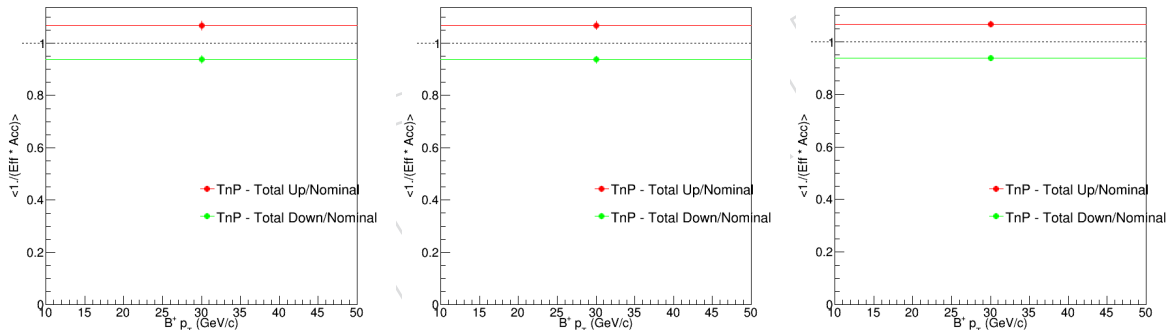


Figure 49: The upper bound and lower bound systematic uncertainties in $\langle \frac{1}{\alpha \times e} \rangle$ vs p_T with total tag and probe correction are shown above.

448 10.6 Selection efficiency: Splot weight

⁴⁴⁹ The potential difference in variable distributions in data and MC entails difference in calculation
⁴⁵⁰ of efficiency correction. Especially, the BDT distributions of MC can be modified by Splot
⁴⁵¹ weight (shown in section 5) to have closer distribution with data.

⁴⁵² We use the same method as the B_s analysis to implement the BDT score from the Splot studies.
⁴⁵³ The details of reweighting and calculation of systematic uncertainties can be found in the B_s
⁴⁵⁴ AN [1] Section 10.5.2: "Systematics Associated with Data-MC Disagreement".

⁴⁵⁵ This will bring the selection efficiency calculation modulated by BDT, and we quote the differ-
⁴⁵⁶ ence between the nominal and Splot-weighted $\langle \frac{1}{\alpha \times e} \rangle$ as our systematics in selection efficiency.
⁴⁵⁷ Table. 15 and Table. 16 shows the systematics for differential p_T and inclusive p_T , respectively.
⁴⁵⁸ Fig. 50 and Fig. 51 shows the comparison plots for differential p_T and inclusive p_T , respectively.

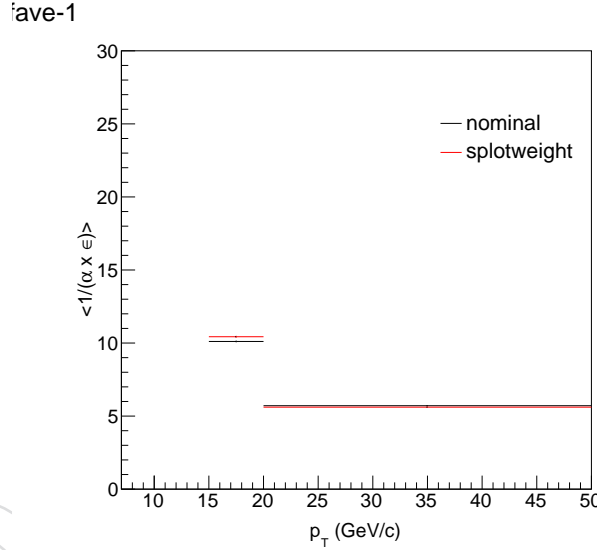
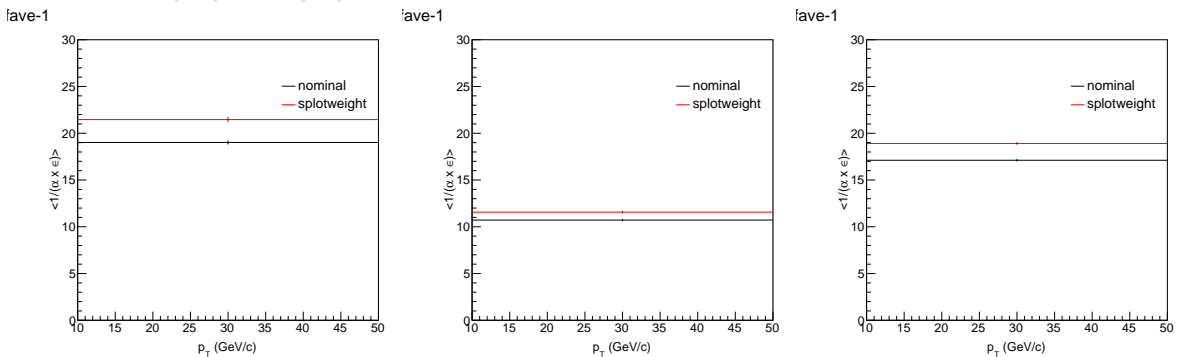
$p_T(\text{GeV})$	7-10	10-15	15-20	20-50
Syst(%)	5.67	15.30	3.61	1.72

Table 14: Systematic uncertainties associated with Splot weight for p_T bins in centrality 0-90%.

$p_T(\text{GeV}/c)$	7-10	10-15	15-20	20-50
Syst(%)	3.92	15.00	3.20	1.74

Table 15: Systematic uncertainties associated with Splot weight for p_T bins in centrality 0 - 90%.

Centrality	0-30%	30-90%	0-90%
Syst(%)	12.86	7.92	10.5

Table 16: Systematic uncertainties associated with Splot weight for inclusive p_T with centrality binning.Figure 50: Comparison of $\langle \frac{1}{\alpha} \rangle$ data-average correction factor between Splot weight and nominal MC in within 0-90% centrality.Figure 51: Comparison of $\langle \frac{1}{\alpha} \rangle$ data-average correction factor between Splot weight and nominal MC for p_T 10 - 50 GeV/c in centrality 0 - 30% (Left), 30 - 90% (Middle), and 30 0 - 90% centrality (Right).

459 **10.7 p_T shape: Bpt weight**

460 The potential difference in p_T distributions in data and MC entails difference in calculation of
 461 efficiency correction. The B^+ p_T distributions of MC can be modified by Bpt weight (shown in
 462 2.2.1) to have closer distribution with data. This will change the acceptance*efficiency calcula-
 463 tion, and we quote the difference between the nominal and Bpt-weighted $1/(acceptance*efficiency)$
 464 as our systematics.

465 Table. 17 and Table. 18 shows the systematics for differential p_T and inclusive p_T , respectively.
 466 Fig. 52 and Fig. 53 shows the comparison plots for differential p_T and inclusive p_T , respec-
 467 tively. Note that the systematics are very small, thus the differences may not be distinguished
 468 prominently on the plots.

$p_T(\text{GeV}/c)$	7-10	10-15	15-20	20-50
Syst(%)	0.128	0.206	0.000	0.010

Table 17: Systematic uncertainties associated with Bpt weight for p_T bins in centrality 0 - 90%.

Centrality	0-30%	30-90%	0-90%
Syst(%)	0.122	0.163	0.146

Table 18: Systematic uncertainties associated with Bpt weight for inclusive p_T with centrality binnings.

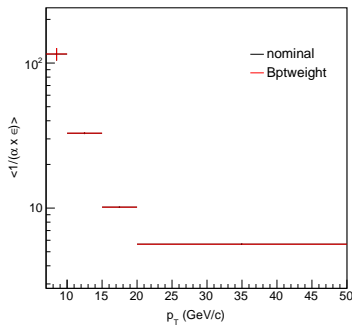


Figure 52: Comparison of $\langle \frac{1}{\alpha \times \epsilon} \rangle$ correction factor between B p_T weight and nominal MC in 0 - 90% centrality.

469 We can see that the p_T shape systematic uncertainties on the efficiency correction have been
 470 reduced to negligible using the $\langle \frac{1}{\alpha \times \epsilon} \rangle$ approach.

471 **10.8 MC stats: Toy MC study**

472 The statistical uncertainties of $\langle \frac{1}{\alpha \times \epsilon} \rangle$ in MC are examined by toy MC study. From the nominal
 473 2D map, we generated 10000 toy MCs for each rapidity p_T bin. The toy 2D maps are then
 474 propagated to the $\langle \frac{1}{\alpha \times \epsilon} \rangle$ data-average calculation. The distribution of data-averages are drawn
 475 in each analysis p_T and centrality bin, and the RMS deviation of the distribution (supposedly
 476 Gaussian) is compared to the nominal value. The ratio between RMS and the nominal value is
 477 quoted as systematics related to MC stats.

478

479 Table. 19 and Table. 20 shows the systematics for differential p_T and inclusive p_T , respectively.
 480 Fig. 54 and Fig. 55 shows the toy MC $1/(acceptance*efficiency)$ distributions for differential p_T
 481 and inclusive p_T , respectively. The blue markers are toy MC distribution, the red lines are the
 482 nominal correction factors in the main analysis.

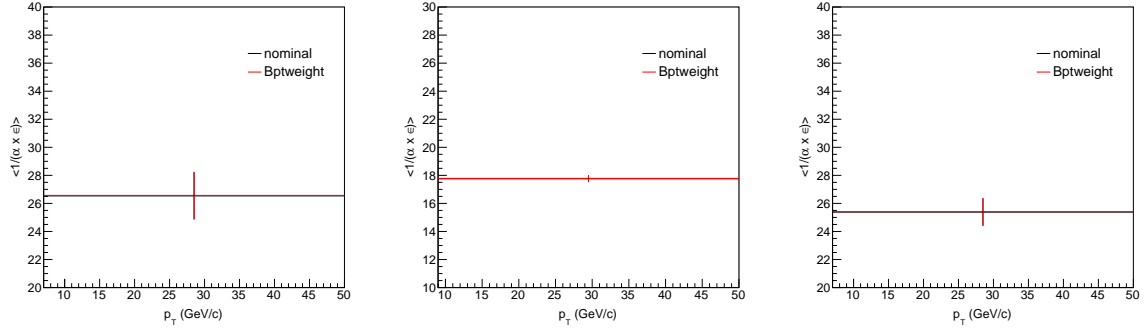


Figure 53: Comparison of $\langle \frac{1}{\alpha \times \epsilon} \rangle$ correction factor between B p_T weight and nominal MC in p_T 10 - 50 GeV/ in 0 - 30% (Left), 30% - 90% (Middle), and 0-90% (Right) centrality.

p_T (GeV/c)	7-10	10-15	15-20	20-50
Syst(%)	14.86	3.75	2.20	1.51

Table 19: Toy MC systematics for p_T bins in centrality 0 - 90%.

Centrality	0-30%	30-90%	0-90%
Syst(%)	3.42	1.37	2.33

Table 20: Toy MC systematics for inclusive p_T with centrality binning.

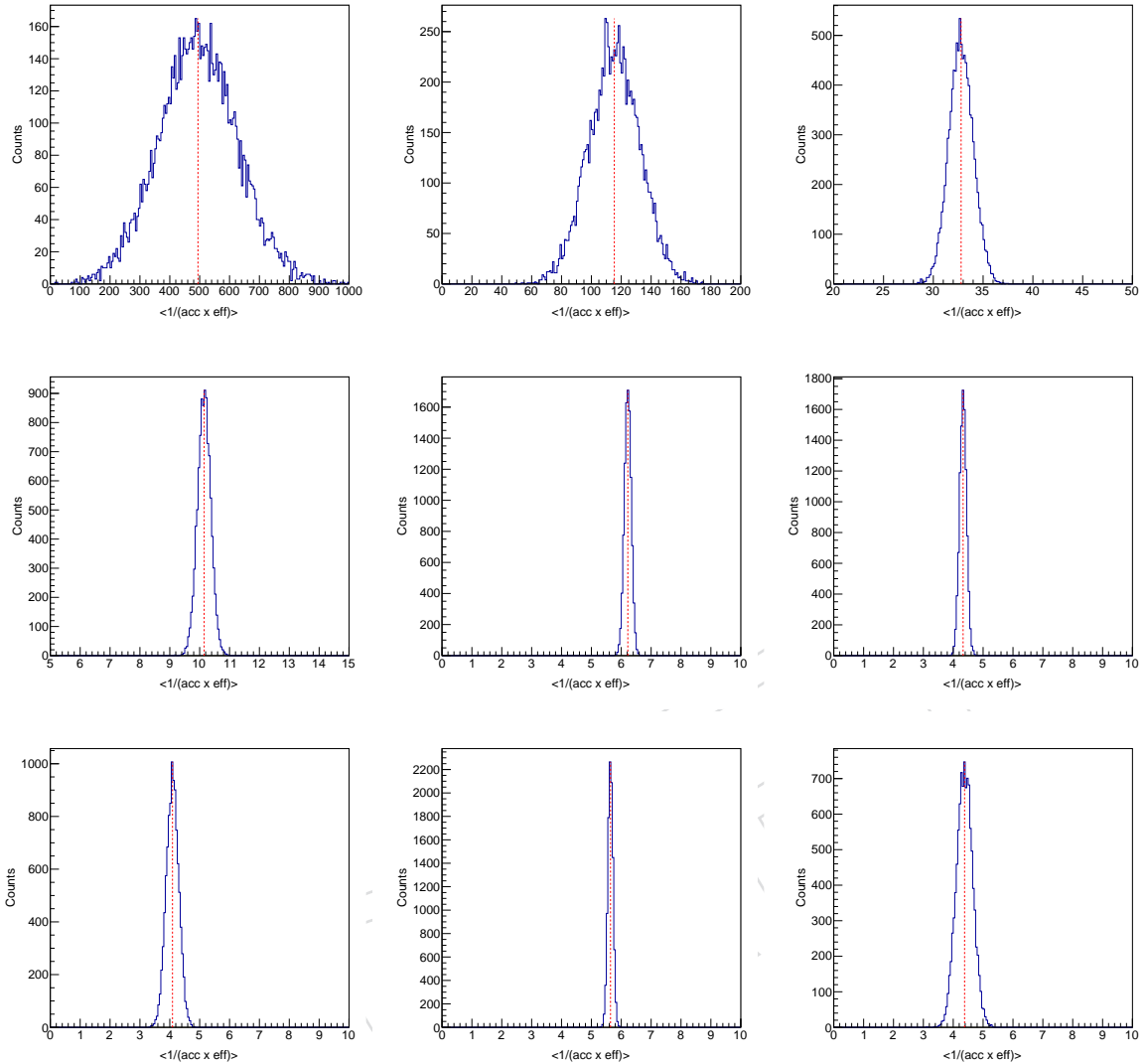


Figure 54: $1/(\text{acceptance} \times \text{efficiency})$ distributions of toy MCs for differential p_T bins. From left to right, top to bottom, 5-7, 7-10, 10-15, 15-20, 20-30, 30-40, 40-50, 20-50, and 50-60 GeV in centrality 0-90% are shown, respectively.

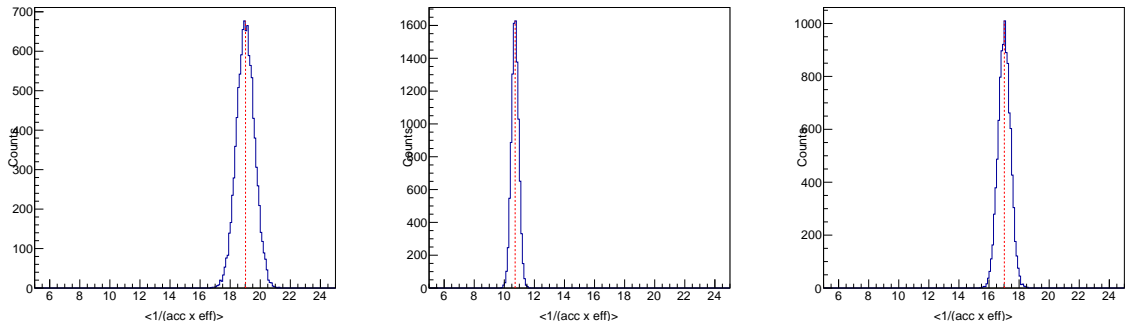


Figure 55: $1/(\text{acceptance} \times \text{efficiency})$ distributions of toy MCs for inclusive p_T bins 10 - 50 GeV/c for 0 - 30% (Left), 30 - 90% (Middle), and 0 - 90% (Right).

483 10.9 Signal extraction: PDF variation

484 Here we quote the numbers. For plots with more details, see Appendix. C.

485 As discussed in detail in Sec. 6, the central value of the raw yields were extracted using a
 486 fit function of Double Gaussian signal and exponential combinatorial background. The non-
 487 prompt component was modeled with an error function and a Gaussian peak. The systematic
 488 uncertainty on the signal extraction was evaluated by varying the functions used to model the
 489 various components:

- 490 • Model the signal with a triple Gaussian function.
- 491 • Release the constraint on the width of the signal double Gaussian (fixed in the de-
 492 fault fit to the MC extracted values). In this case, a scaling factor (a) between the MC
 493 widths is left as a free parameter in order to account for possible differences between
 494 the resolution in data and MC.
- 495 • Fixed the mean of the signal double Gaussian.
- 496 • Consider 1st, 2nd, and 3rd order polynomial for combinatorial background.

The detailed description on the release of the constraints on the widths of the signal double Gaussian is as follows. The full signal model used in the fit to data is:

$$497 \alpha \frac{1}{a\sigma_1 \sqrt{2\pi}} e^{-\frac{1}{2} \frac{(B_{mass}-\mu)^2}{(a\sigma_1)^2}} + (1 - \alpha) \frac{1}{a\sigma_2 \sqrt{2\pi}} e^{-\frac{1}{2} \frac{(B_{mass}-\mu)^2}{(a\sigma_2)^2}}, \quad (2)$$

497 where a is the resolution scaling factor (the same for both gaussians) which describes the pos-
 498 sible discepancy between data and MC fit, α is the relative proportion between the gaussians,
 499 σ_1 and σ_2 are the Gaussians' widths that are directly derived from MC fit, and μ is the mean
 500 shared by both Gaussians.

501 In order to examine the potential systematic difference in data and MC signal fit, we are re-
 502 quired to define a moderate variation range of the scaling factor in order not to introduce sta-
 503 tistical fluctuations in our estimation. To achieve this, we first performed fit by letting the
 504 scaling factor float around in individual p_T bins and inclusive p_T bin (Figure 56). The parame-
 505 ter values from the best fit are summarised in Table 21.

506 We observed that in several individual p_T bins, the deviations from unity(value for nominal fit)
 507 are sizable. In mid p_T bins (10-15-20-30GeV) where statistics are comparably large, the devia-
 508 tions are small. Whereas in low p_T bins(5-7-10GeV) and high p_T bins(30-40-50-60GeV) where
 509 statistics are small, the deviations are relatively large. On the other hand, the optimal scailing
 510 factors of individual p_T bins agree with that of inclusive p_T bin within a significance of 2σ .
 511 From this observation, the sizable differences can be considered to mainly come from statistical
 512 limitation of each small p_T ranges. In addition, the 2σ difference can be considered to be the
 513 statistical uncertainties of scaling factors of individual p_T bins.

514 To conclude, we can claim that the scaling factor of the inclusive p_T ($a = 1.09 \pm 0.04$) is a rep-
 515 resentative of the scaling factor for all p_T bins. Since that factor is a optimal fit parameter, we
 516 can take 10% variation from the nominal value(unity) as our signal PDF variation range where
 517 the fits are good enough and has reasonably low statistical uncertainties, which is desirable
 518 for systematic uncertainties estimation. Here we used jargons increased and decreased width
 519 which refers to $a = 1.1$ and 0.9 , respectively.

520 The full results of the various fits extracted with the different fit functions in PbPb are pre-
 521 sented in Appendix C. For pdf variation in p_T 50-60GeV centrality 0-90%, we don't quote any
 522 systematics from background component. This is because the background in that highest p_T
 523 bin is essentially zero and we can only fit and vary signal components. We pick the maximum

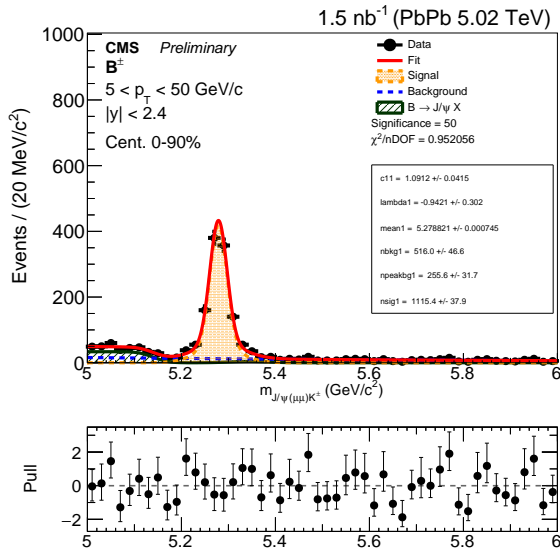


Figure 56: Invariant mass fit of B^+ candidates for $5 < p_T < 50 \text{ GeV}/c$ in 5.02 TeV , with an extra free parameter in the signal model a , as described by Eq. 2

$p_T(\text{GeV}/c)$	Scaling factor a
5–7	1.45 ± 0.25
7–10	1.33 ± 0.16
10–15	1.07 ± 0.07
15–20	0.98 ± 0.08
20–30	1.02 ± 0.08
30–40	1.12 ± 0.13
40–50	0.89 ± 0.18
50–60	0.95 ± 0.18
5–50	1.09 ± 0.04

Table 21: Summary table of the value obtained for the parameter a , when using the signal model described by Eq. 2, in different p_T bins.

524 value among the various background variations and the maximum value among the various
 525 signal variations. Then sum them up in quadrature to get the total pdf variation uncertainties.
 526

PDF/ p_T (GeV)	7-10	10-15	15-20	20-30
30-40	40-50	20-50		
Triple Gaussian	0.004	0.235	0.500	0.750
Fixed Mean	1.13	0.046	0.030	0.010
Increased Width	3.84	2.27	2.32	1.79
Decreased Width	4.46	2.67	2.36	

Table 22: Systematic uncertainties associated with signal PDF variation for p_T bins. All values are in units of %.

PDF/ p_T (GeV)	7-10	10-15	15-20	20-50
Linear Poly	0.021	0.312	0.386	0.196
2nd Poly	0.117	0.380	0.432	0.238
3rd Poly	0.093	0.546	0.576	1.03

Table 23: Systematic uncertainties associated with background PDF variation for p_T bins. All values are in units of %.

PDF/ p_T (GeV)	7-10	10-15	15-20	20-50
Signal	4.46	2.67	2.74	2.36
Background	0.117	0.546	0.576	1.03
Total	4.46	2.73	2.80	2.57

Table 24: Total systematic uncertainties associated PDF variation for p_T bins. All values are in units of %.

PDF/Centrality	0-30%	30-90%	0-90%
Triple Gaussian.	0.415	0.370	0.494
Fixed Mean	0.155	0.064	0.060
Increased Width	2.12	2.10	2.19
Decreased Width	2.50	2.57	2.60

Table 25: Systematic uncertainties associated with signal PDF variation for inclusive p_T with centrality bins. All values are in units of %.

PDF/Centrality	0-30%	30-90%	0-90%
Linear polynomial	0.157	1.13	0.384
2nd order polynomial	0.245	0.065	0.427
3rd order polynomial	0.412	0.102	0.422

Table 26: Systematic uncertainties associated with background PDF variation for inclusive p_T with centrality bins. All values are in units of %.

PDF/Centrality	0-30%	30-90%	0-90%
Signal	2.50	2.57	2.60
Background	0.412	1.13	0.427
Total	2.53	2.81	2.64

Table 27: Total systematic uncertainties associated PDF variation for inclusive p_T with centrality bins. All values are in units of %.

527 A Training Results

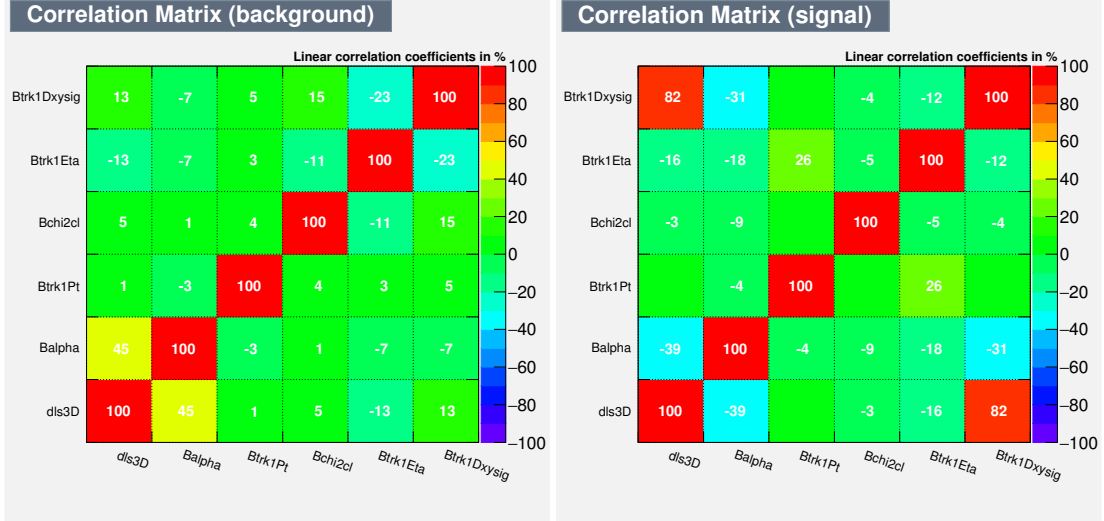


Figure 57: TMVA training correlation matrices of PbPb in p_T 7-10GeV/c.

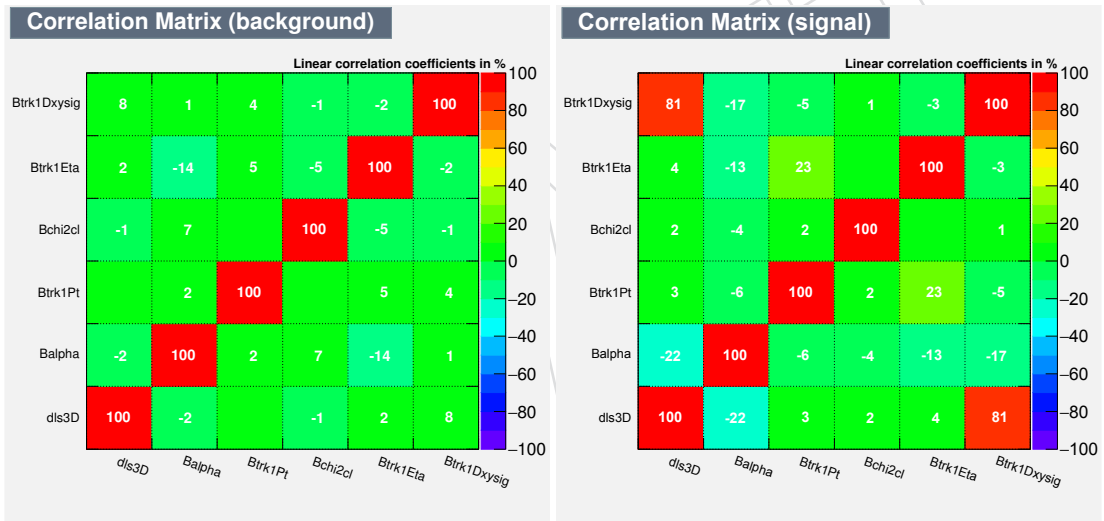
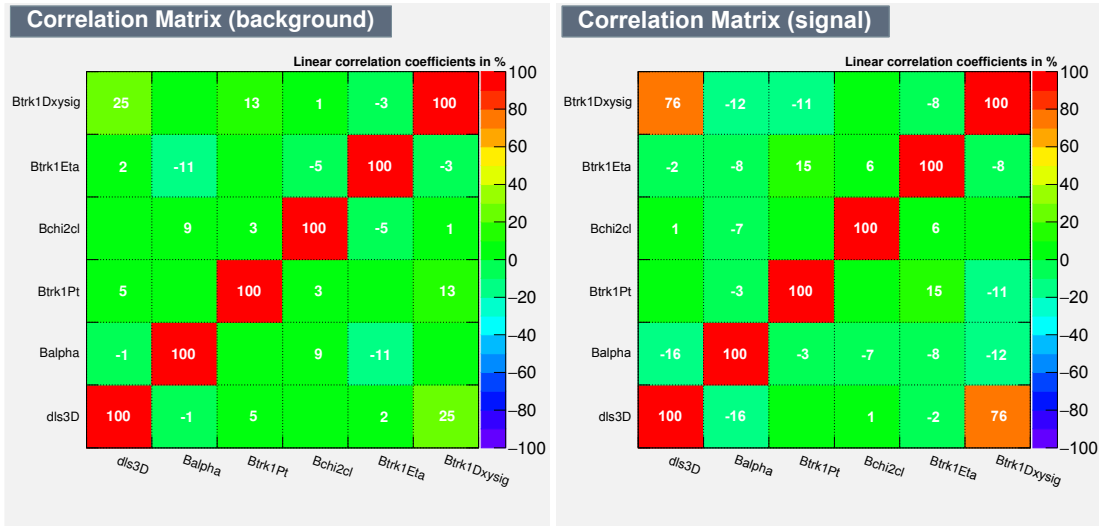
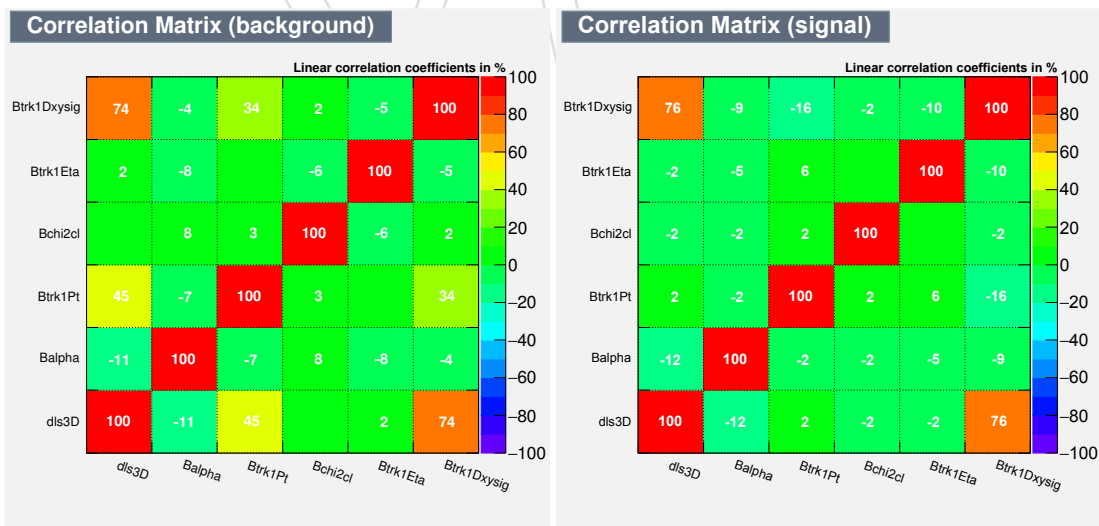


Figure 58: TMVA training correlation matrices of PbPb in p_T 10-15GeV/c.

Figure 59: TMVA training correlation matrices of PbPb in p_T 15-20GeV/c.Figure 60: TMVA training correlation matrices of PbPb in p_T 20-30GeV/c.

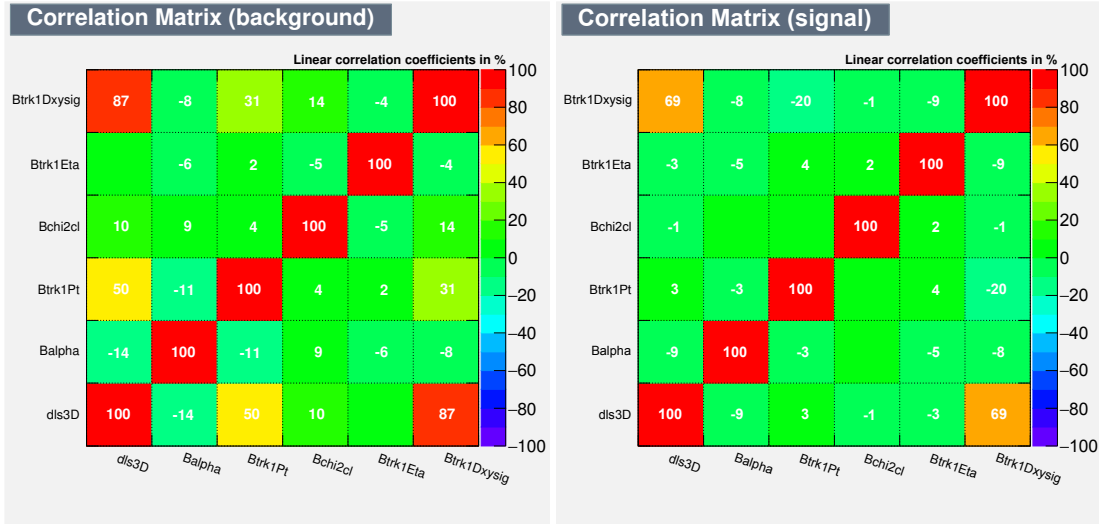


Figure 61: TMVA training correlation matrices of PbPb in p_T 30-40GeV/c.

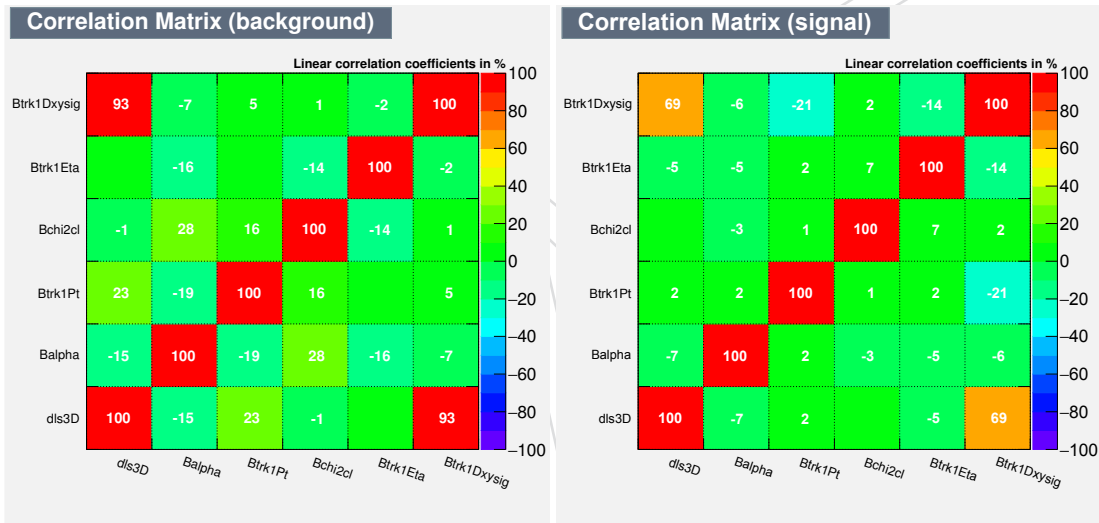


Figure 62: TMVA training correlation matrices of PbPb in p_T 40-50GeV/c.

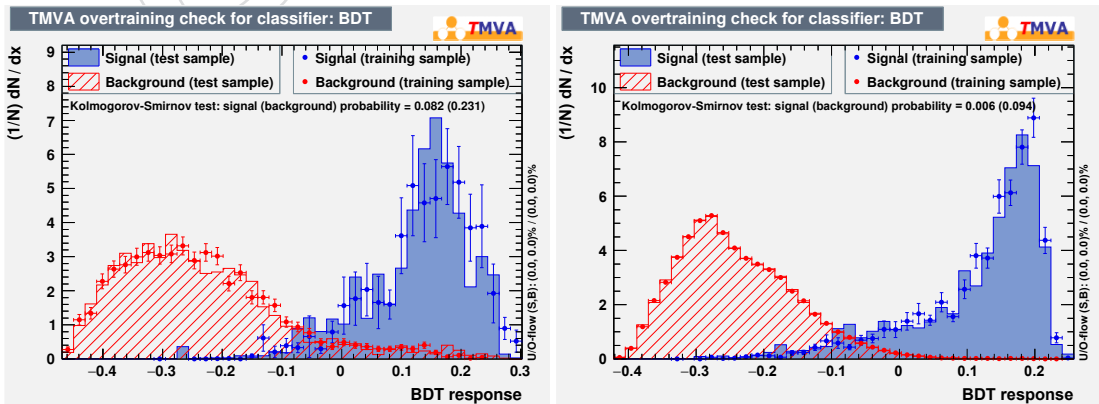


Figure 63: TMVA overtraining check of PbPb in p_T 7-10 and 10-15GeV/c, respectively

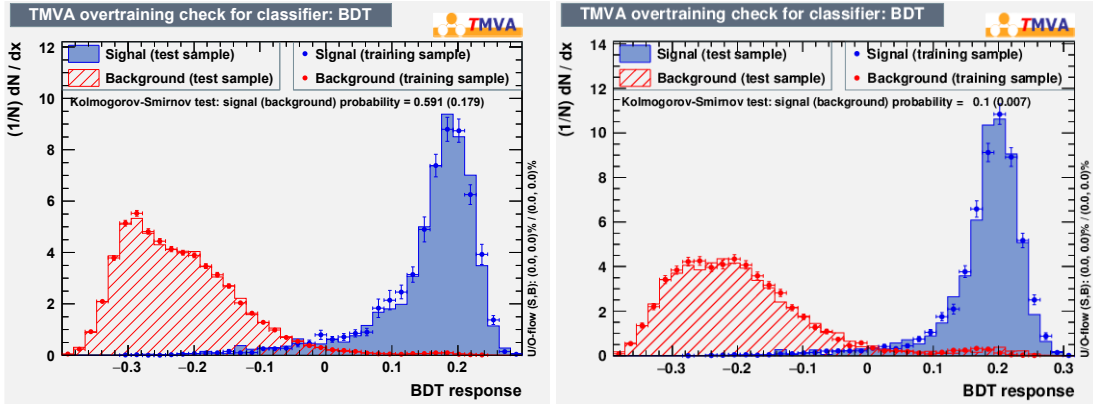


Figure 64: TMVA overtraining check of PbPb in p_T 15-20 and 20-30GeV/c, respectively

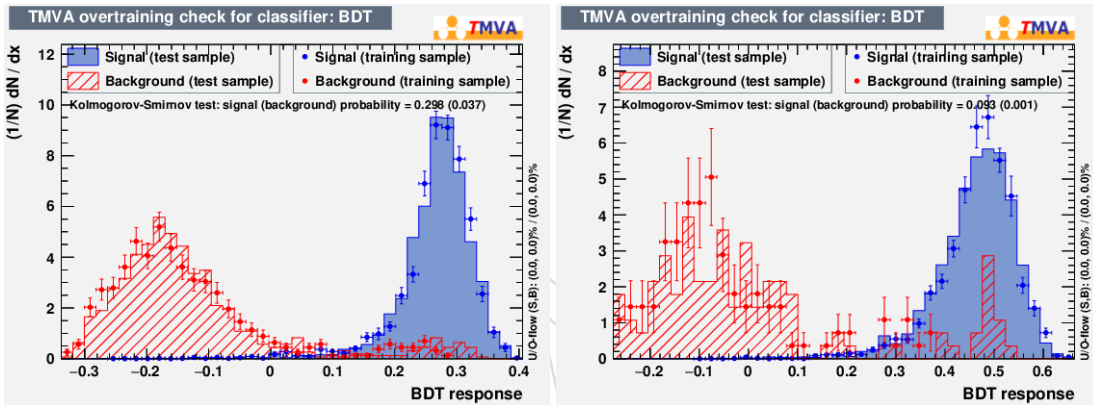


Figure 65: TMVA overtraining check of PbPb in p_T 30-40 and 40-50GeV/c, respectively

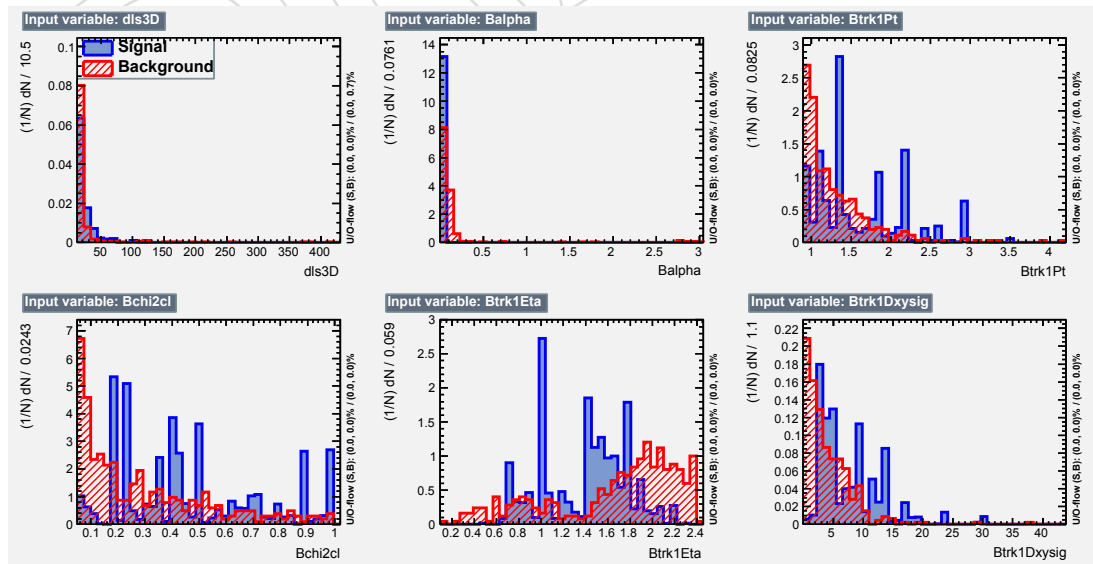


Figure 66: TMVA training variable distribution of PbPb in p_T 5-7GeV/c.

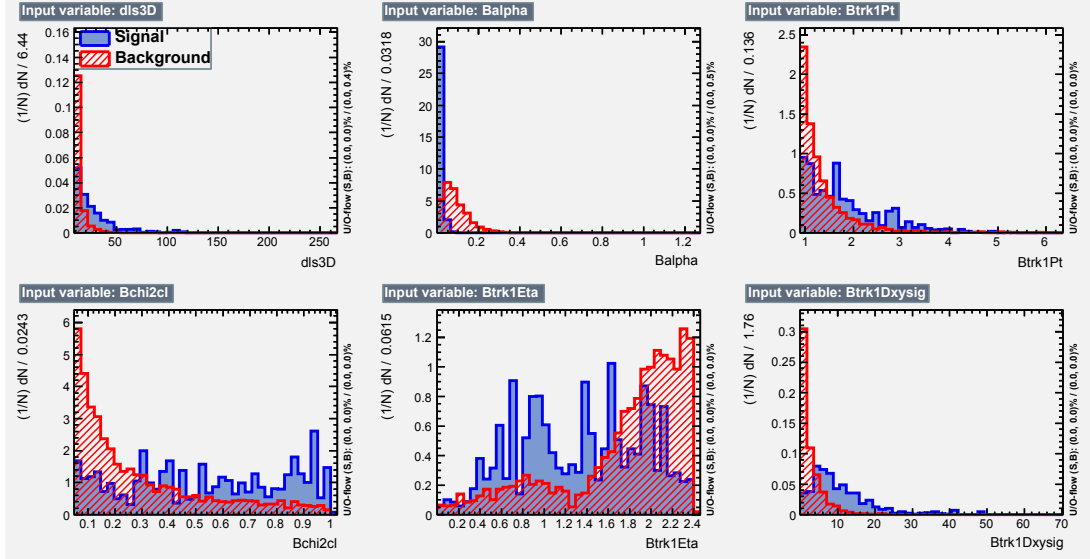


Figure 67: TMVA training variable distribution of PbPb in p_T 7-10 GeV/c.

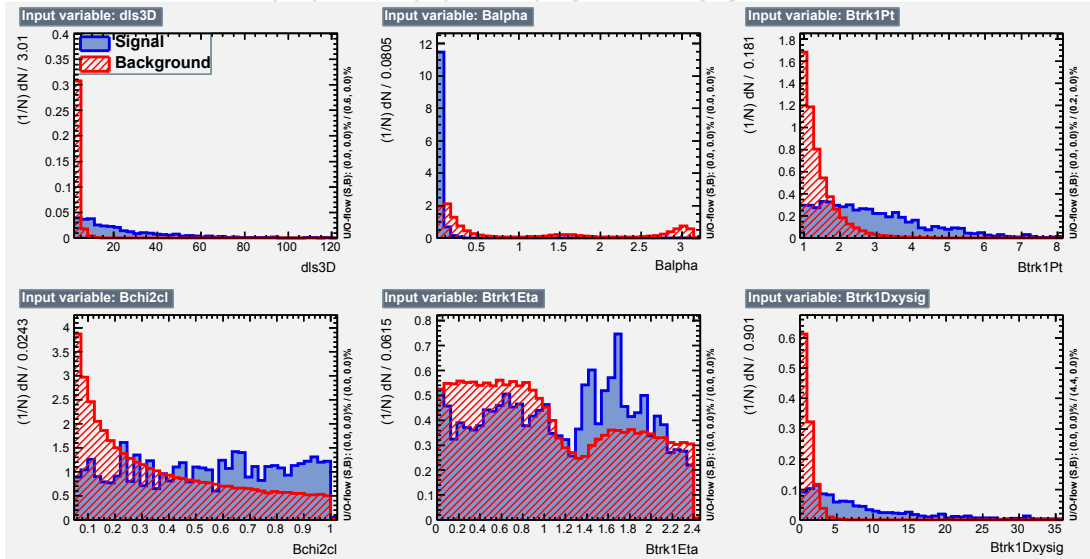


Figure 68: TMVA training variable distribution of PbPb in p_T 10-15 GeV/c.

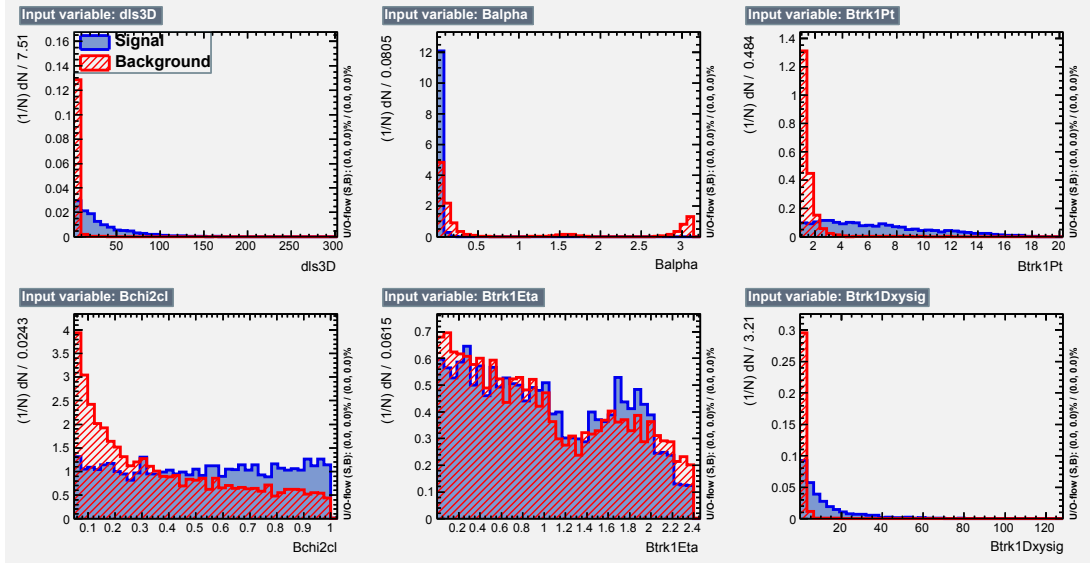


Figure 69: TMVA training variable distribution of PbPb in p_T 20-30GeV/c.

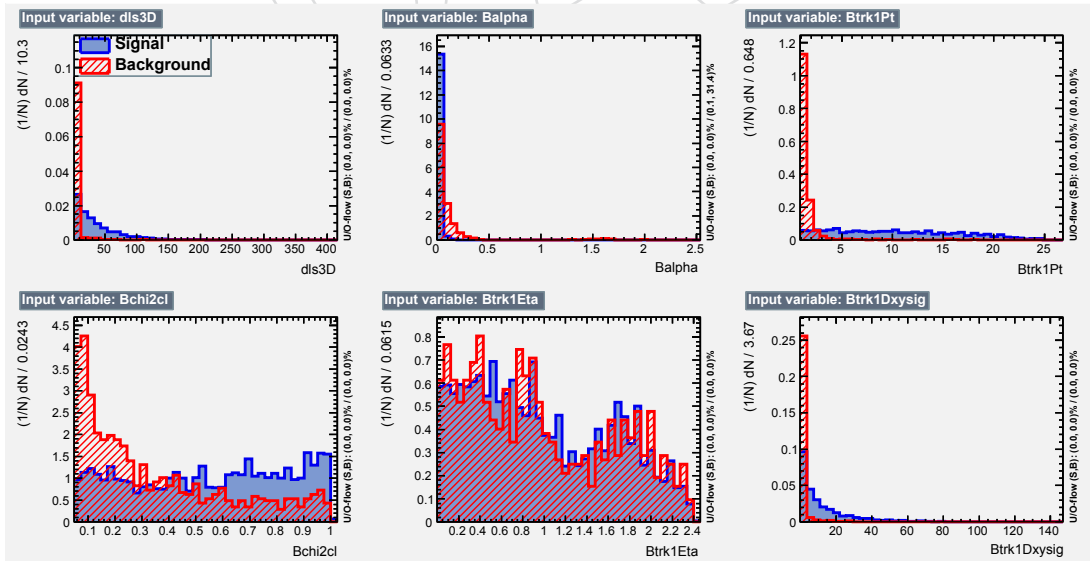


Figure 70: TMVA training variable distribution of PbPb in p_T 30-40GeV/c.

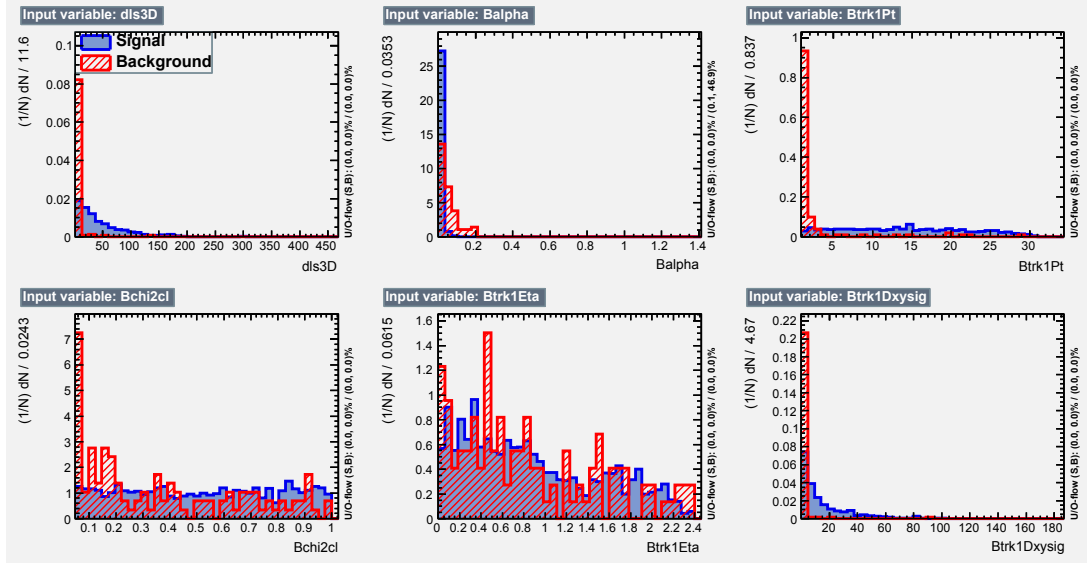


Figure 71: TMVA training variable distribution of PbPb in p_T 40-50GeV/c.

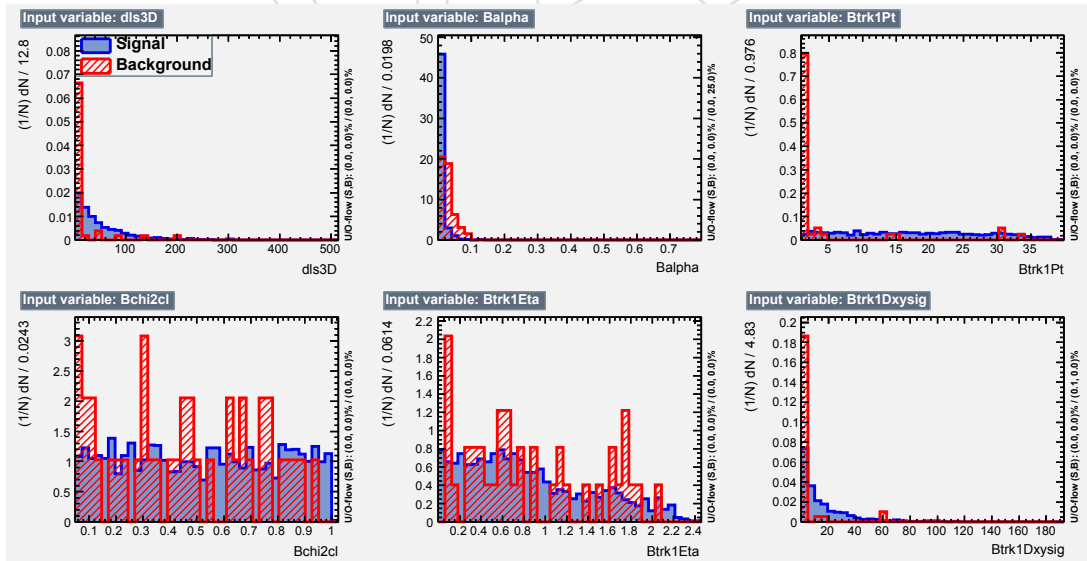


Figure 72: TMVA training variable distribution of PbPb in p_T 50-60GeV/c.

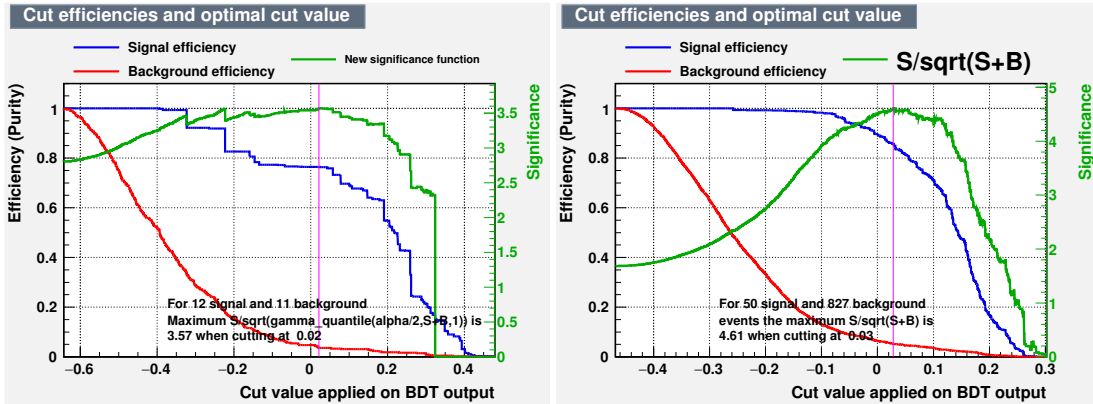


Figure 73: TMVA significance curve of PbPb in p_T 5-7 and 7-10GeV/c, respectively

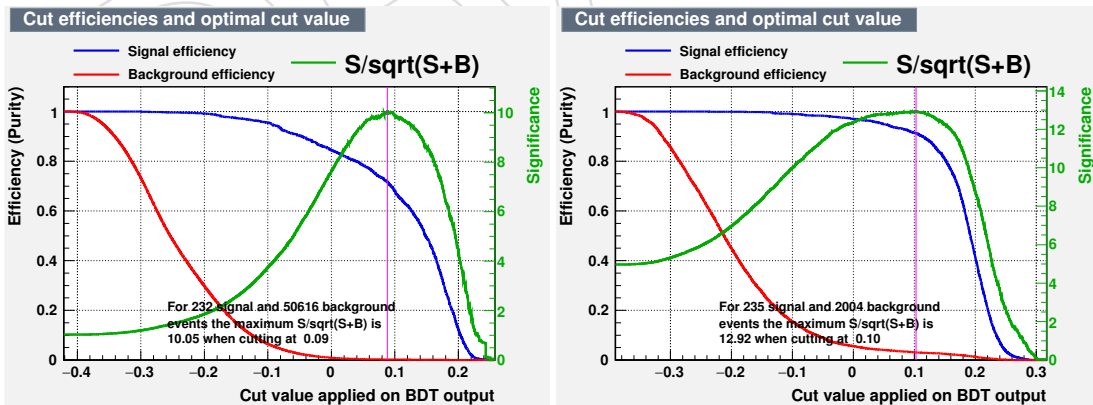


Figure 74: TMVA significance curve of PbPb in p_T 10-15 and 20-30GeV/c, respectively

528 B Non-prompt J/ψ background

529 In the B^+ invariant mass spectrum, there are potential background feed-down sources coming
 530 from other B meson decays that can form peaking structures in the region of interest, and need
 531 to be properly subtracted in order not to bias the yield extraction procedure. In order to esti-
 532 mate these components, we processed the inclusive B meson MC sample with the nominal B^+
 533 channel workflow, and vetoed the candidates that are matched to a genuine B^+ signal. The re-
 534 sulting B candidate mass spectrum in the inclusive p_T range (5-100 GeV/c) is shown in Fig. 77
 535 for PbPb MC samples.

536 It is clear that these sources create a peaking structure in the region of $M_{inv} < 5.20 \text{ GeV}/c^2$.
 537 This structure can be nicely fit with an error function as done previously in B proton-proton
 538 analyses [10]. In addition, there is a minor peak on the right shoulder ($\approx 5.34 \text{ GeV}/c^2$) of the
 539 nominal signal ($\approx 5.28 \text{ GeV}/c^2$), and this can be fit with an Gaussian function. There is ad-
 540 dditional combinatorial background which is fitted with a linear function. This contribution is
 541 absorbed in the total combinatorial background of our nominal channel of the main analysis.
 542 As described in details in Sec. 6, the shape of the Non-prompt function is used as template in
 543 the fit extraction procedure.

544 Further MC studies were done in order to identify the different channels that give rise to the
 545 non-prompt peaking structure in the B^+ invariant mass spectrum. Few main processes were
 546 identified:

- 547 • 4-body B^+ decays which occur via resonant decay channels e.g. $B^+ \rightarrow J/\psi K^*(892)^+$.
 548 In these cases, we distinguish the kaons coming from the $K^*(892)^+$ decays as coming
 549 from a signal $B^+ \rightarrow J/\psi K^+$ decay.
- 550 • 4-body B^0 decays channels e.g. $B^0 \rightarrow J/\psi K^*(892)^0$.
- 551 • $B^+ \rightarrow J/\psi \pi^+$ decays in which we misidentified the π^+ as a K^+ .

552 The different contributions in PbPb are presented in Fig. 78. The contribution from $B^+ \rightarrow J/\psi \pi$
 553 clearly form a peaking structure on the right shoulder of the nominal decay channel $B^+ \rightarrow$
 554 $J/\psi K^+$. However, the overall magnitude of this component is tiny compared to the other two
 555 sources, and negligible compared to the nominal signal. As a consequence, we can barely see
 556 the contribution of this peaking structure in the invariant mass plot of B^+ nominal channel.

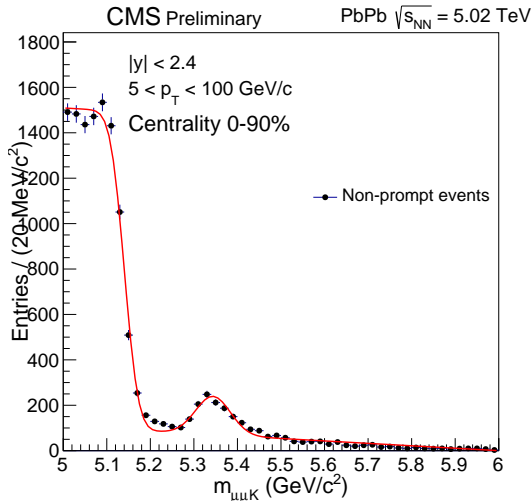


Figure 77: B^+ candidate mass spectrum obtained in inclusive B meson MC production after vetoing the contribution of genuine B^+ signal candidates in PbPb.

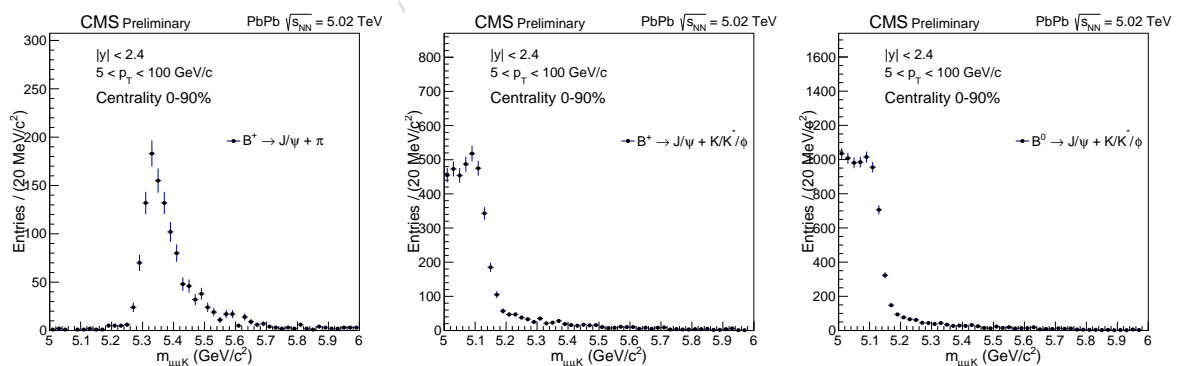


Figure 78: Peaking background contribution from $B^+ \rightarrow J/\psi \pi$ and from K resonant decay channels of B^0 and B^+ in PbPb MC.

557 C PDF variation studies

558 Here we show the pdf variation plots. In each figure, from left to right, top to bottom, triple
 559 Gaussian, fixed mean double Gaussian, width-increased double Gaussian, width-decreased
 560 double Gaussian, linear background, quadratic background, and cubic background are shown
 561 respectively. Note that background fit variation fails in 50-60GeV within centrality 0-90% in
 562 Fig. 87 due to zero background, thus we do not consider background variation in this kinematic
 563 range.

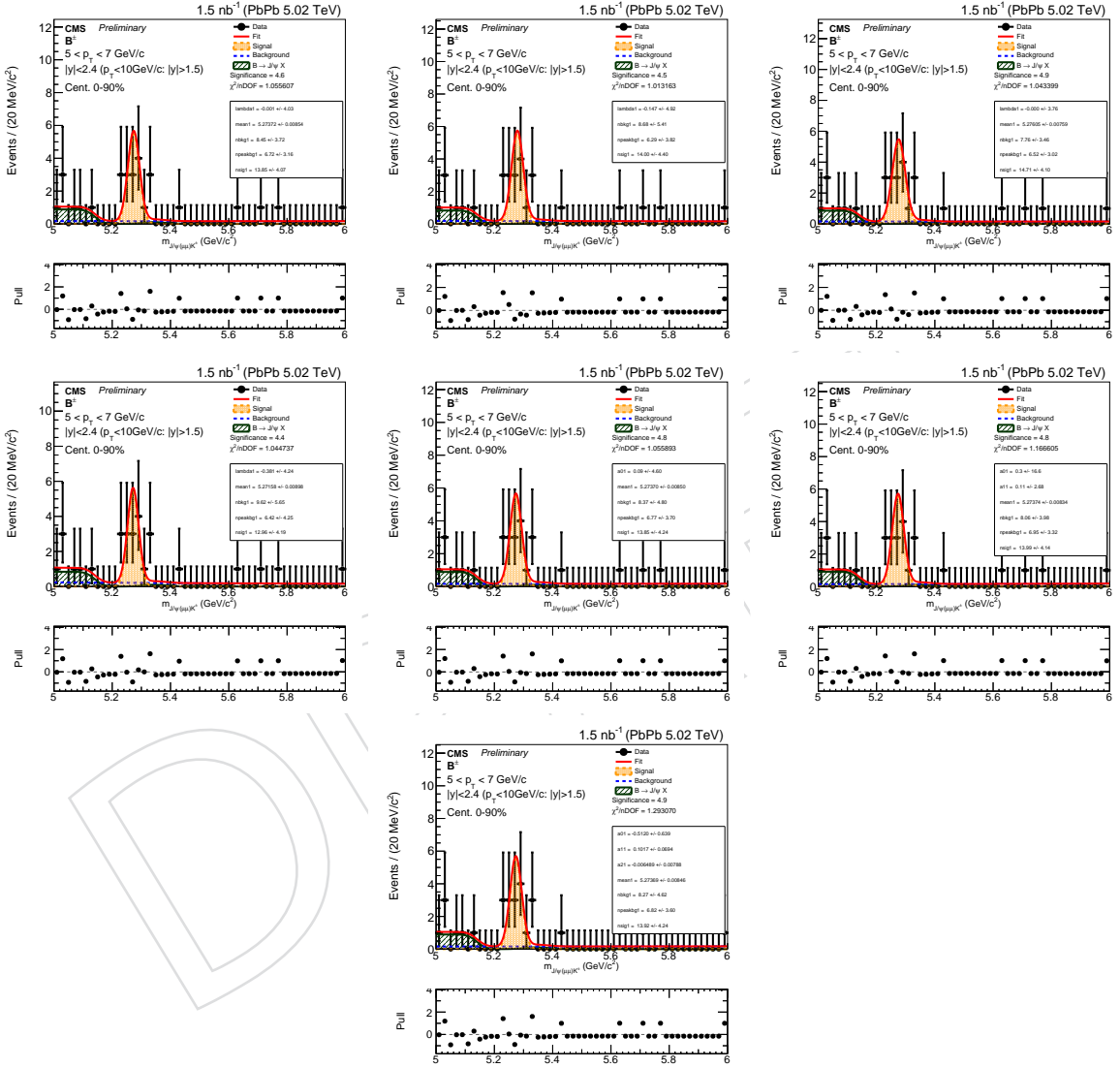


Figure 79: Signal and background modeling variation for PbPb analysis in p_T 5-7 GeV/c within 0-90% centrality.

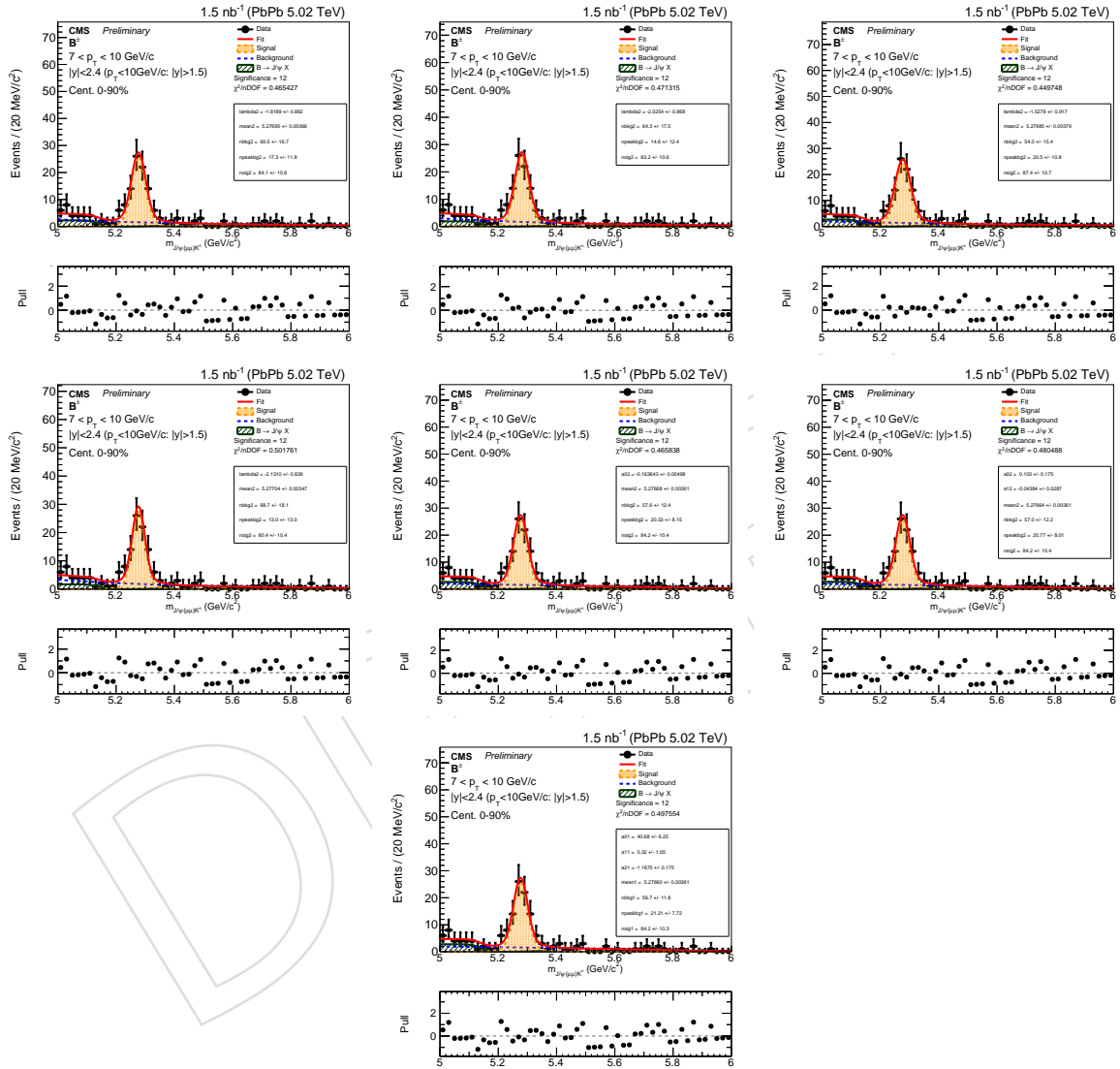


Figure 80: Signal and background modeling variation for PbPb analysis in p_T 7-10 GeV/c within 0-90% centrality.

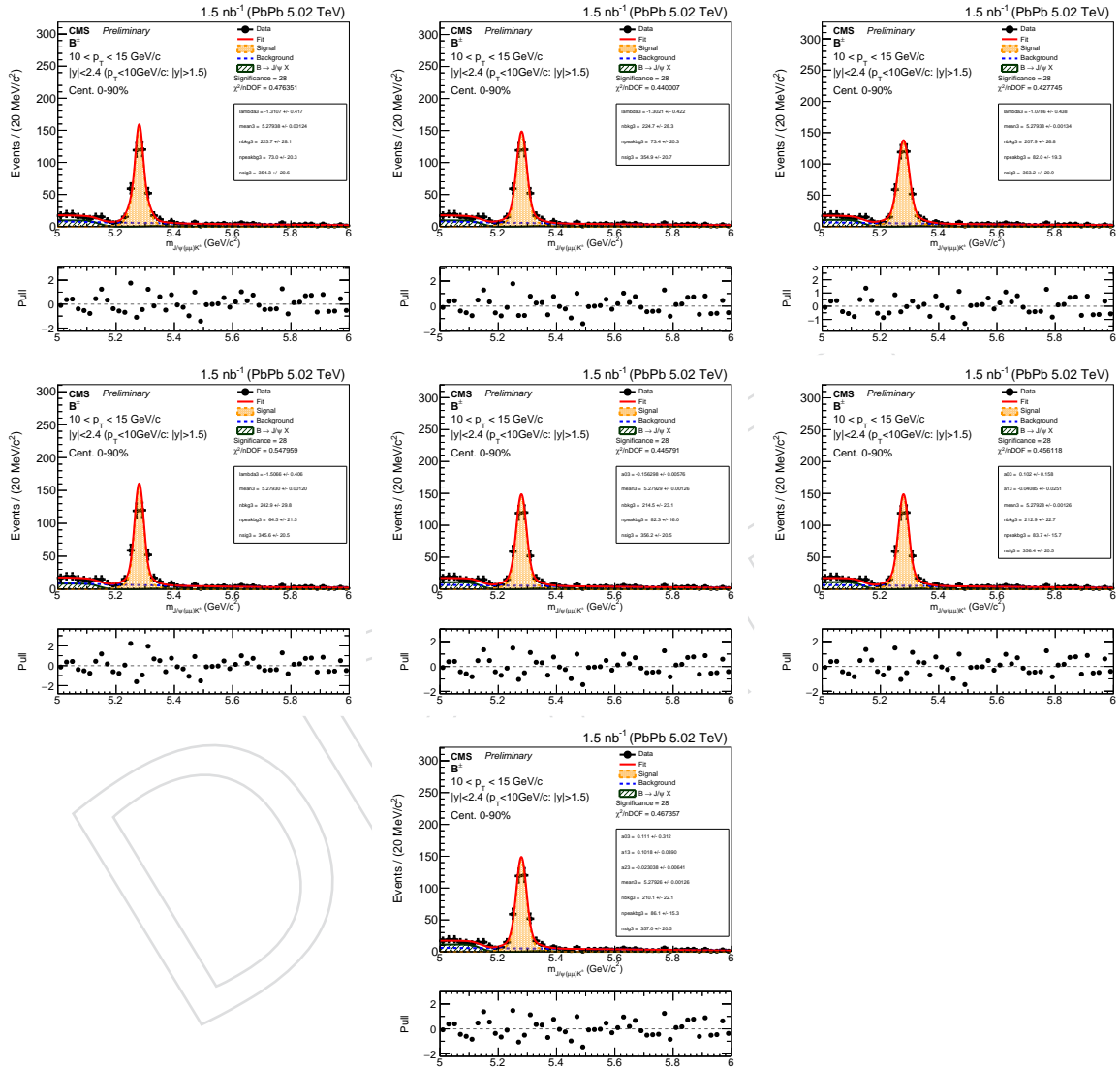


Figure 81: Signal and background modeling variation for PbPb analysis in p_T 10-15 GeV/c within 0-90% centrality.

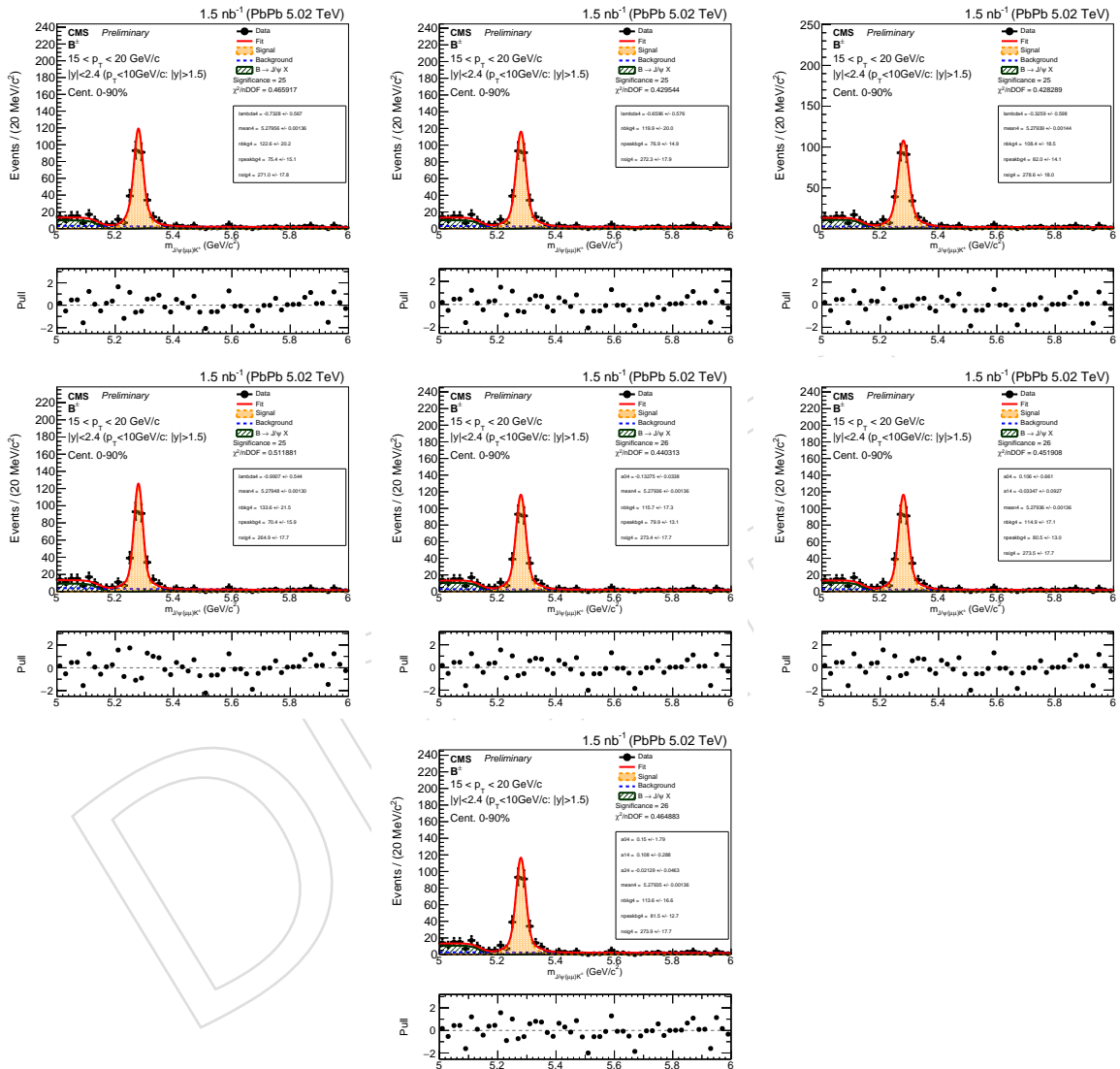


Figure 82: Signal and background modeling variation for PbPb analysis in p_T 15-20 GeV/c within 0-90% centrality.

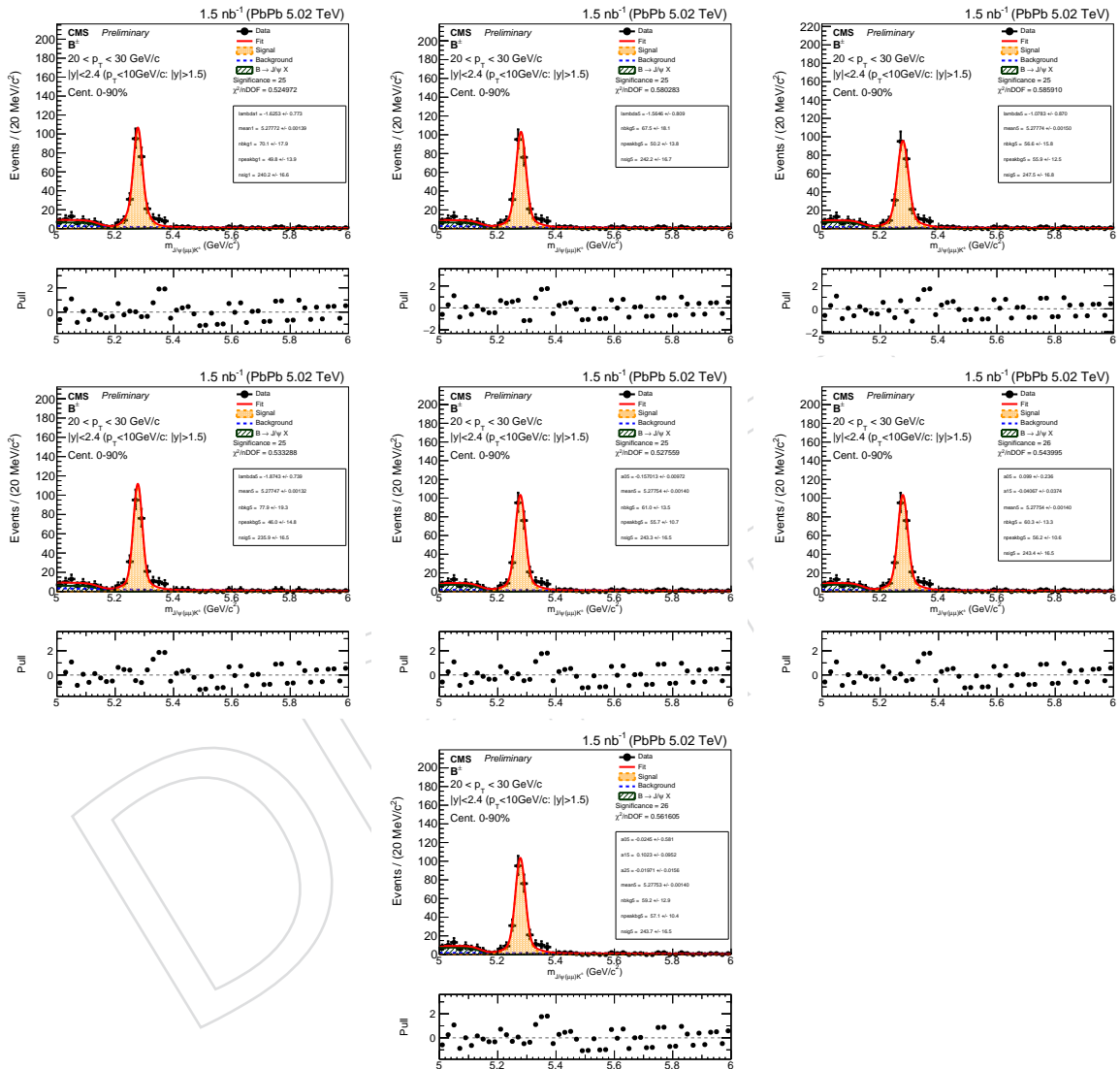


Figure 83: Signal and background modeling variation for PbPb analysis in p_T 20-30 GeV/c within 0-90% centrality.

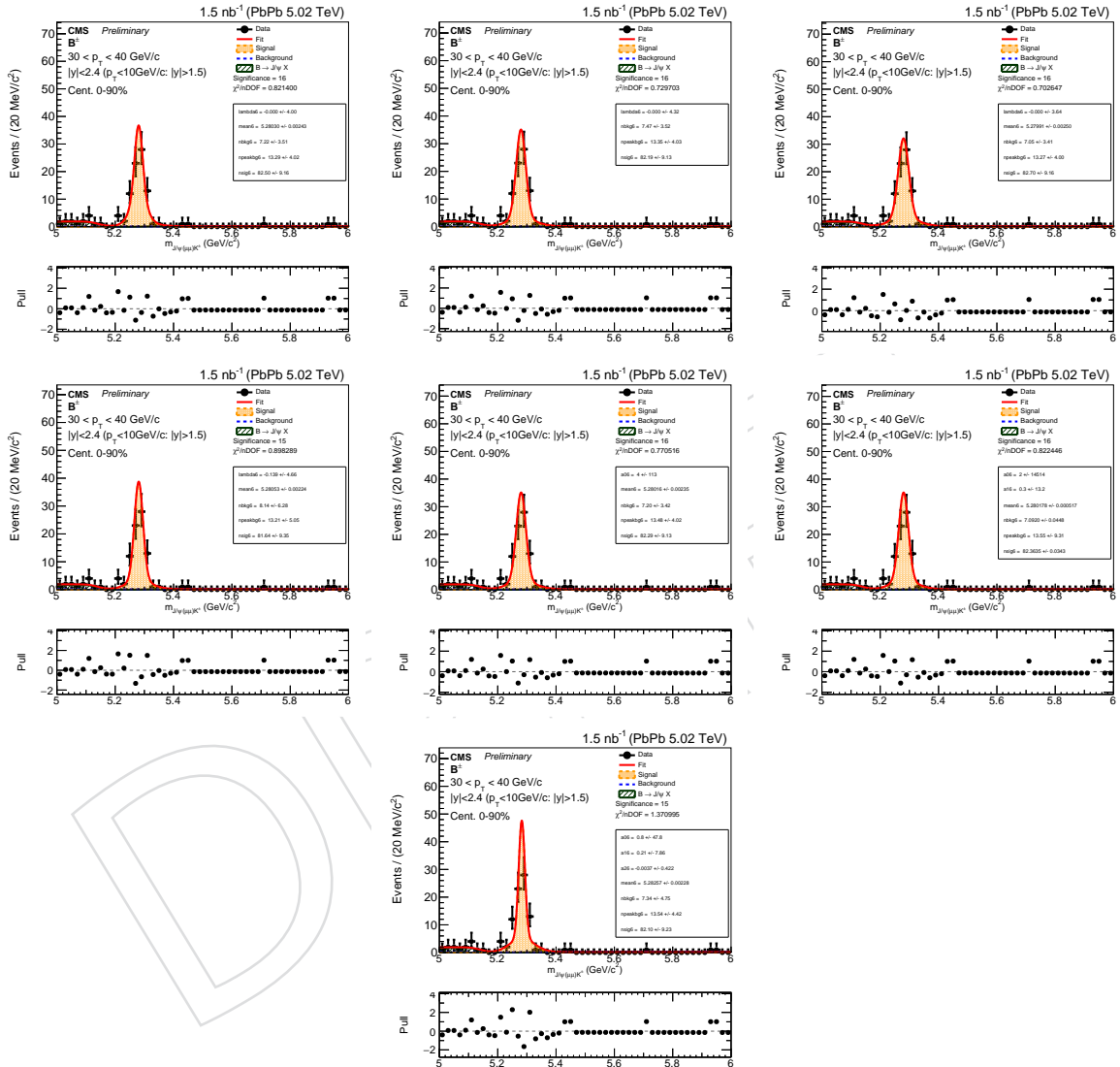


Figure 84: Signal and background modeling variation for PbPb analysis in p_T 30-40 GeV/c within 0-90% centrality.

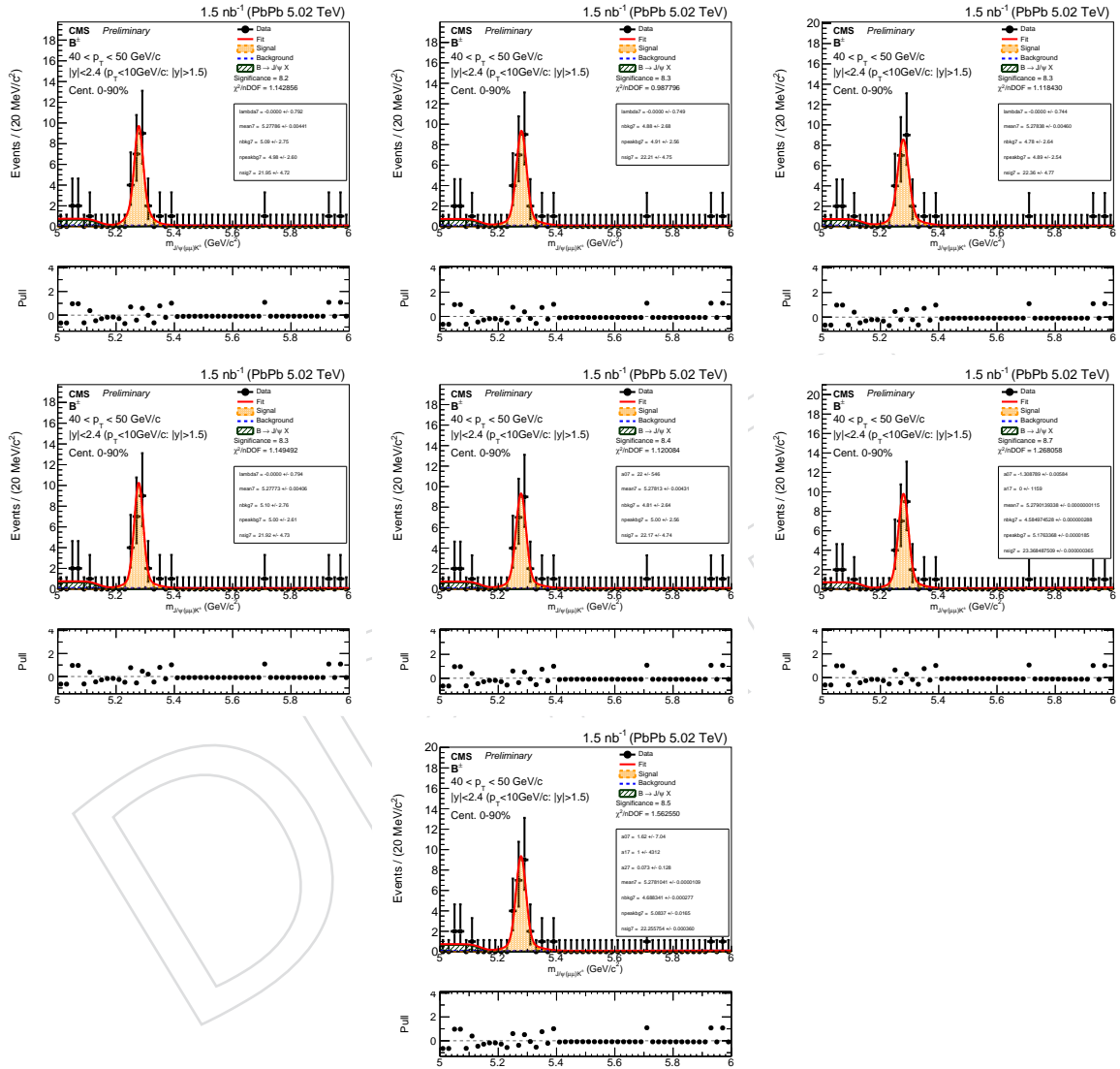


Figure 85: Signal and background modeling variation for PbPb analysis in p_T 40-50 GeV/c within 0-90% centrality.

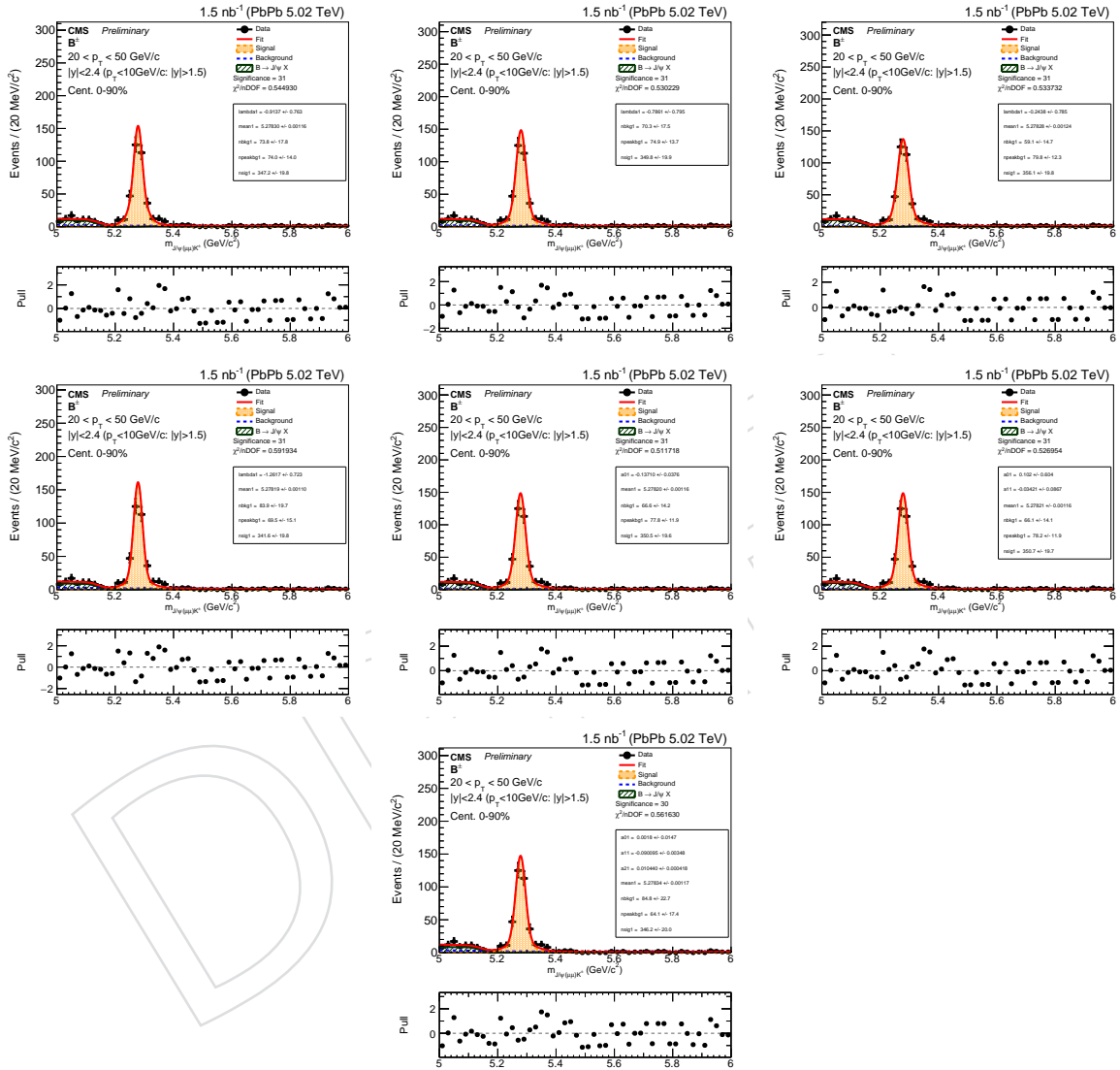


Figure 86: Signal and background modeling variation for PbPb analysis in p_T 20-50 GeV/c within 0-90% centrality.

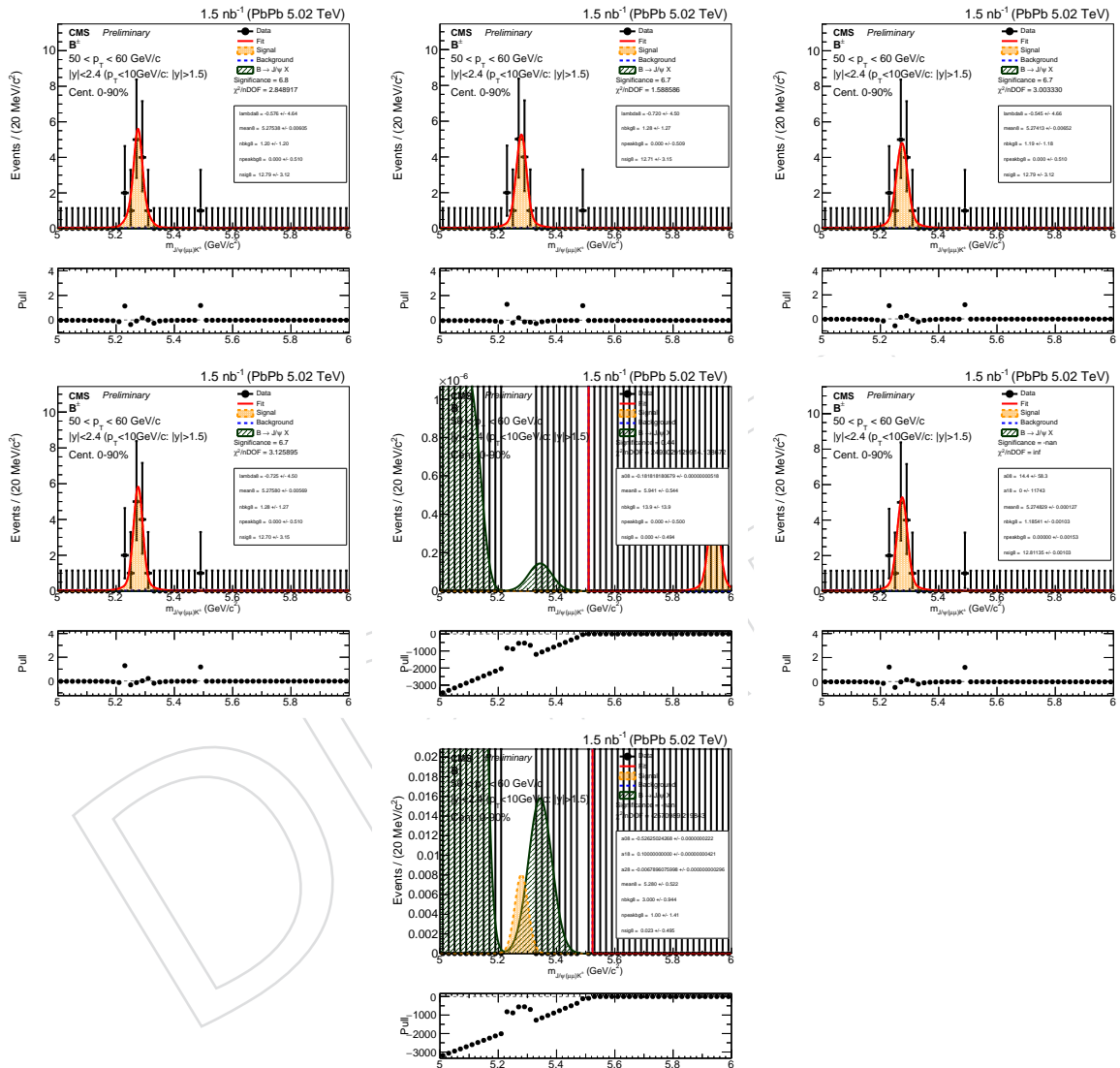


Figure 87: Signal and background modeling variation for PbPb analysis in p_T 50-60 GeV/c within 0-90% centrality.

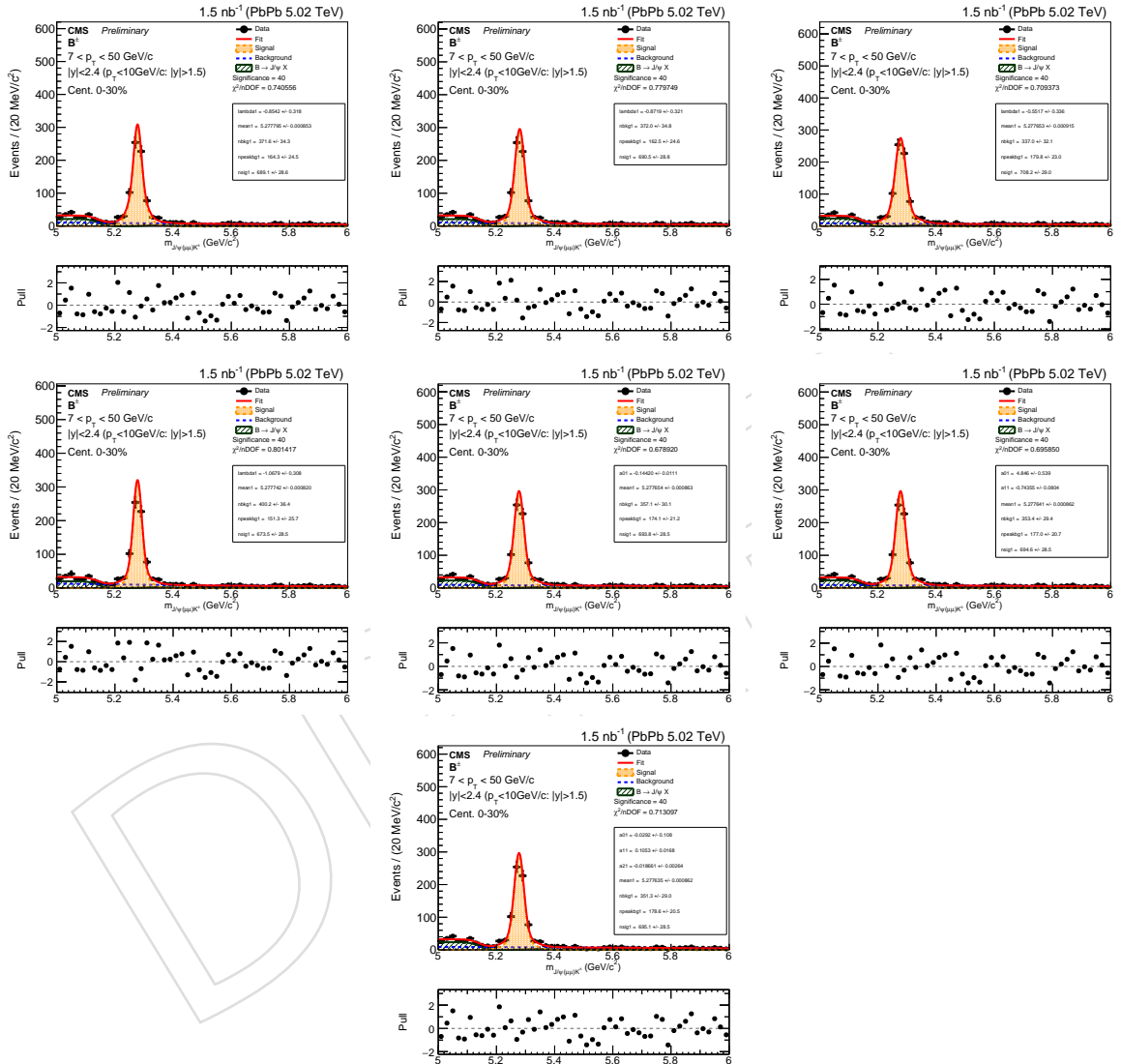


Figure 88: Signal and background modeling variation for PbPb analysis in p_T 7-50 GeV/c within 0-30% centrality.

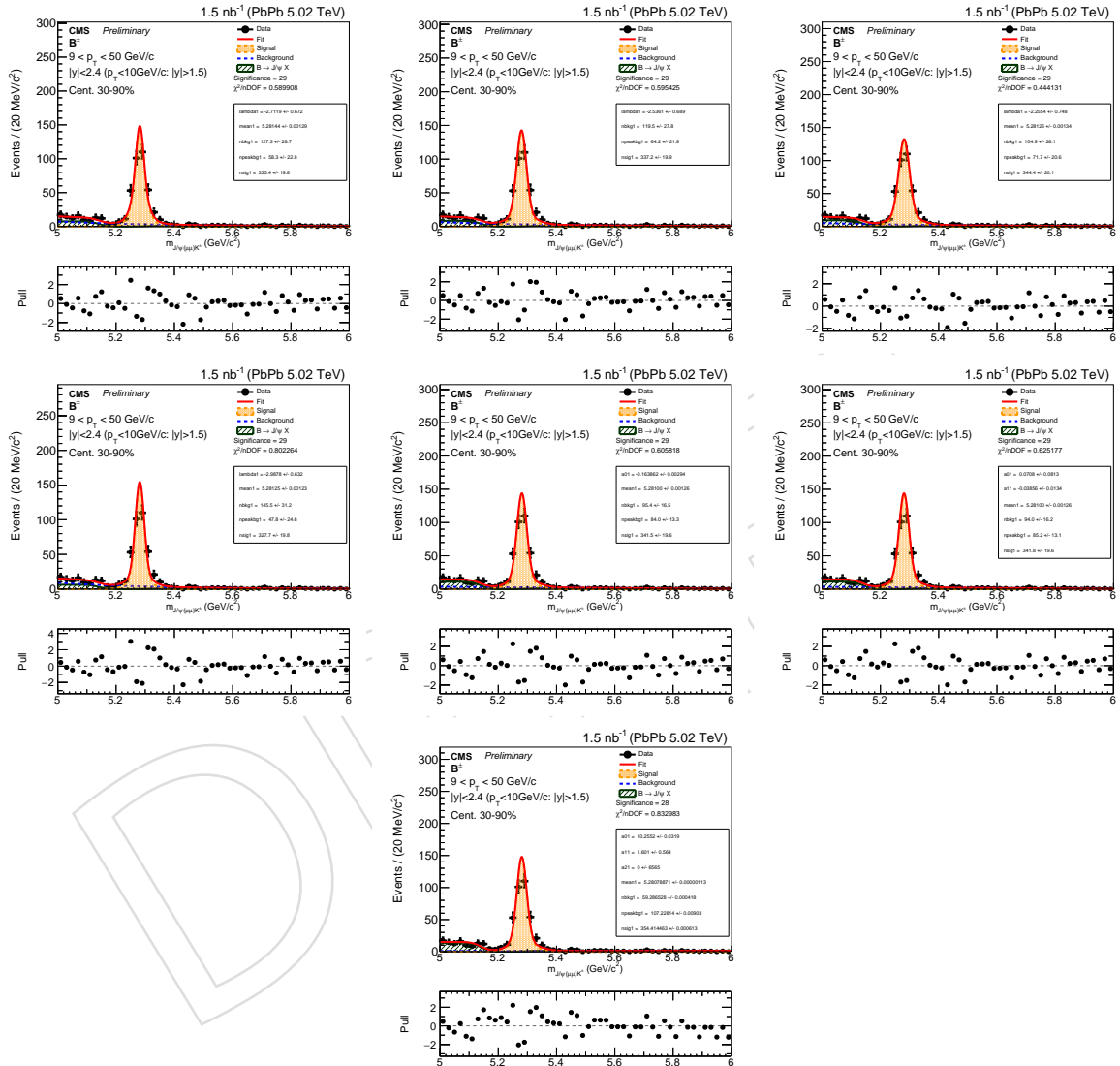


Figure 89: Signal and background modeling variation for PbPb analysis in p_T 9-50 GeV/c within 30-90% centrality.

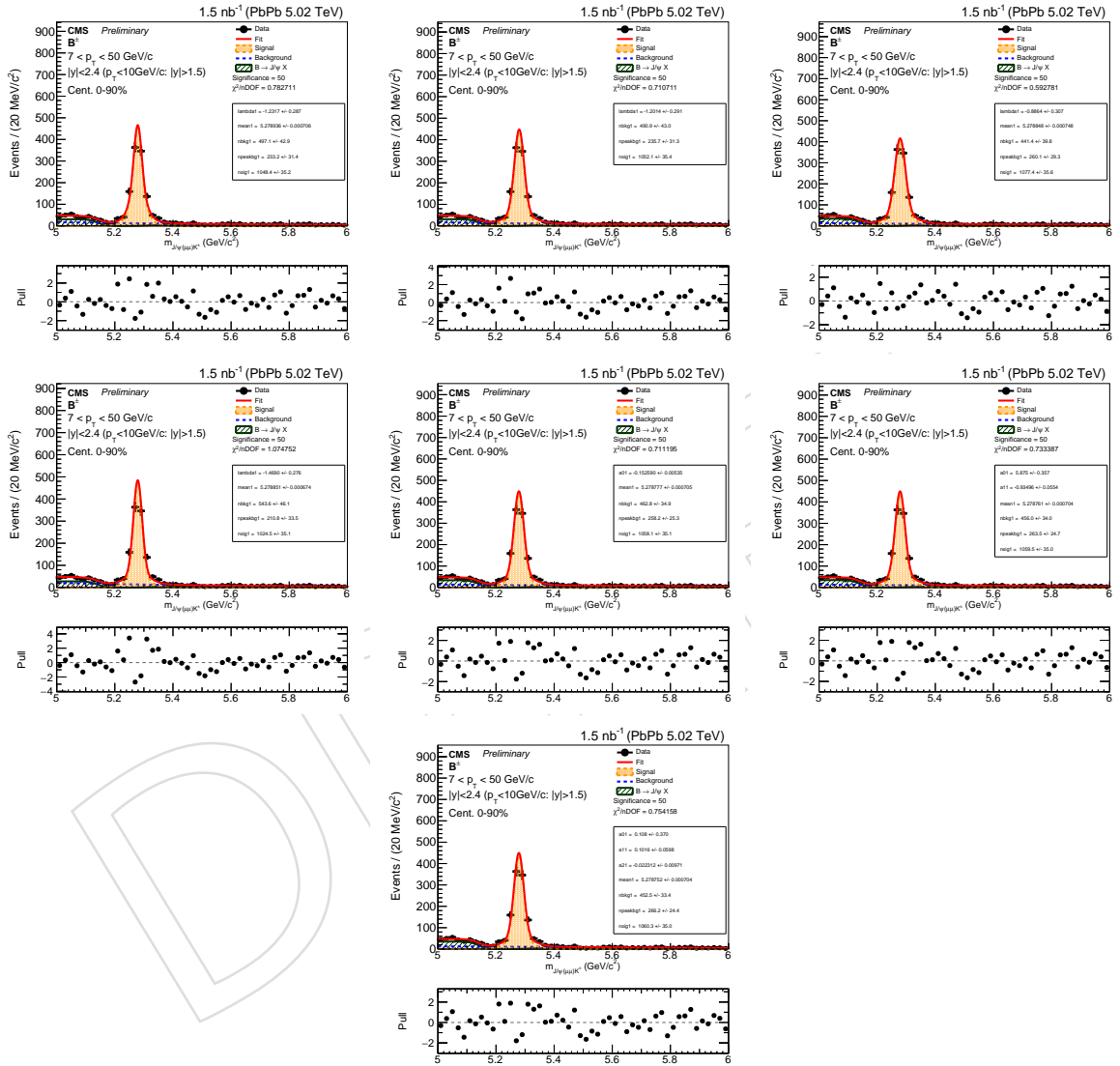


Figure 90: Signal and background modeling variation for PbPb analysis in p_T 7-50 GeV/c within 0-90% centrality.

564 References

- 565 [1] CMS Heavy Ion Group, "Measurement of B_s^0 meson production in pbpb collisions at
566 $\sqrt{s_{NN}} = 5.02$ tev", CMS Analysis Note 2019/055, CERN, 2019.
- 567 [2] Y. L. Dokshitzer and D. E. Kharzeev, "Heavy quark colorimetry of QCD matter", *Phys.*
568 *Lett.* **B519** (2001) 199–206, doi:10.1016/S0370-2693(01)01130-3,
569 arXiv:hep-ph/0106202.
- 570 [3] CMS Collaboration, " Measurement of the charged particle nuclear modification factor in
571 PbPb collisions at $\sqrt{s_{NN}} = 5.02$ TeV", Technical Report CMS-PAS-HIN-15-015, CERN,
572 Geneva, 2016.
- 573 [4] CMS Collaboration, "D⁰ meson nuclear modification factor in PbPb collisions at
574 $\sqrt{s_{NN}} = 5.02$ TeV", Technical Report CMS-PAS-HIN-16-001, CERN, Geneva, 2016.
- 575 [5] CMS Collaboration, " Measurement of $B^{+/-}$ mesons differential production cross
576 sections in pp and PbPb collisions at $\sqrt{s_{NN}} = 5.02$ TeV", Technical Report
577 CMS-PAS-HIN-16-011, CERN, Geneva, 2016.
- 578 [6] CMS Collaboration, " Measurement of the B_s^0 meson nuclear modification factor in pp
579 and PbPb collisions at $\sqrt{s_{NN}} = 5.02$ TeV", Technical Report CMS-PAS-HIN-17-008,
580 CERN, Geneva, 2016.
- 581 [7] Particle Data Group, "Review of particle physics", *Phys. Rev. D* **98** (2018) 030001,
582 doi:10.1103/PhysRevD.98.030001.
- 583 [8] A. Hoecker et al., "TMVA: Toolkit for Multivariate Data Analysis", *PoS ACAT* (2007)
584 040, arXiv:physics/0703039.
- 585 [9] CMS Heavy Ion Group, "B meson production in pbpb data: signal extraction and mc
586 validation", CMS Analysis Note 2019/219, CERN, 2019.
- 587 [10] CMS Collaboration, "Measurement of the B^+ hadron production cross section in pp
588 collisions at 13 TeV", Technical Report CMS-PAS-BPH-15-004, CERN, Geneva, 2015.